Master Thesis in Geosciences

The relation between Syn-sedimentary deformation, Contractional Structures and Fracture Systems in the North-eastern Ainsa Basin, Pyrenees, Spain

by

Erlend Morisbak Jarsve

UNIVERSITY OF OSLO

FACULTY OF MATHEMATICS AND NATURAL SCIENCES

The relation between Syn-sedimentary deformation, Contractional Structures and Fracture Systems in the north-eastern, Pyrenees, Spain

by

Erlend Morisbak Jarsve

Master Thesis in Geosciences

Discipline: Petroleum geology and geophysics

Department of Geosciences

Faculty of Mathematics and Natural Sciences

UNIVERSITY OF OSLO

[June 2008]

Tutor(s): Prof. Roy H. Gabrielsen and Prof. Johan Petter Nystuen

This work is published digitally through DUO – Digitale Utgivelser ved UiO

http://www.duo.uio.no

It is also catalogued in BIBSYS (http://www.bibsys.no/english)

Acknowledgements

First of all I would like to thank my beloved Marianne Vatsøy Jarsve for all support and encouragement during this work.

I owe a special thank to my primary supervisor Prof. Roy H. Gabrielsen for his excellent guiding and support in the field and providing constructive and interesting discussions during this work. I also owe special thanks to my supervisor Prof. Johan Petter Nystuen for the help and support in the field.

I would also like to thank Prof. Cai Puigdefabregas for interesting lectures in the field.

I thank my fellow students Roger Flåt, Ojong Gilbert Ako and Asfaw Tenna for valuable remarks and discussions during this work.

Oslo, June 2008
Erlend Morisbak Jarsve

Contents

Chapter 1 - Introduction

1.1 – Subject

This master thesis include mapping, classification, correlation and interpretation of the major fault and fold systems and the fracture populations of the north-eastern part of the Ainsa Basin with emphasis on determining the development of palaeo-stress fields under which the structures were generated. The work was concentrated in Ainsa Basin, Las Uslas and Lascorz in Ainsa Basin, Spain (Figure 1.1). The structural development is seen in the context of syn-sedimentary deformation associated with intra-basinal slopes and the general structure development of the frontal Pyrenees. The study included field mapping of folds and fault systems, statistical analysis of fractures, microscope analysis and analysis of fracture fill.

The final objective is to determine the relation between the structures and their genesis, i.e. syn-sedimentary structures, which develop during sedimentation, compaction related structures and structures related primarily to tectonics.

1.2 – Field work information

The field work was performed over a period of four weeks and consisted of structural geological data collection for use in the investigation of the subject. This field study was performed in parallel with officiated field study by three other fellow students in the north-eastern part of the Ainsa Basin, Spain (Figure 1.1). The data used in this thesis are collected and analyzed by the writer alone for the Las Uslas and Lascorz areas, whereas in Ainsa Quarry, data was collected together with Ojong Gilbert Ako (In prep.), although analyzed individually.

The field work includes a summer job for Norsk Hydro (StatoilHydro) in the period 9th July to 5th August. The field work was performed in the Ainsa Basin with three fellow students,

i.e. Roger Flåt, Asfaw Tenna Woyessa and Ojong Gilbert Ako, although in different parts of the basin. For ten days, in the period 9th of July to 19th of July, professor Roy H. Gabrielsen and professor Johan Petter Nystuen guided and supported the students in the field. And in July 10th and July 11th, professor Cai Puigdefabregas gave a two days excursion and field introduction (figure 1.2). All students and professors were staying at Appolo Hostel, Ainsa, were Norsk Hydro (StatoilHydro) has a work room with three computers together with internet access. These were used daily after field work, for preparation of data collected in the field.

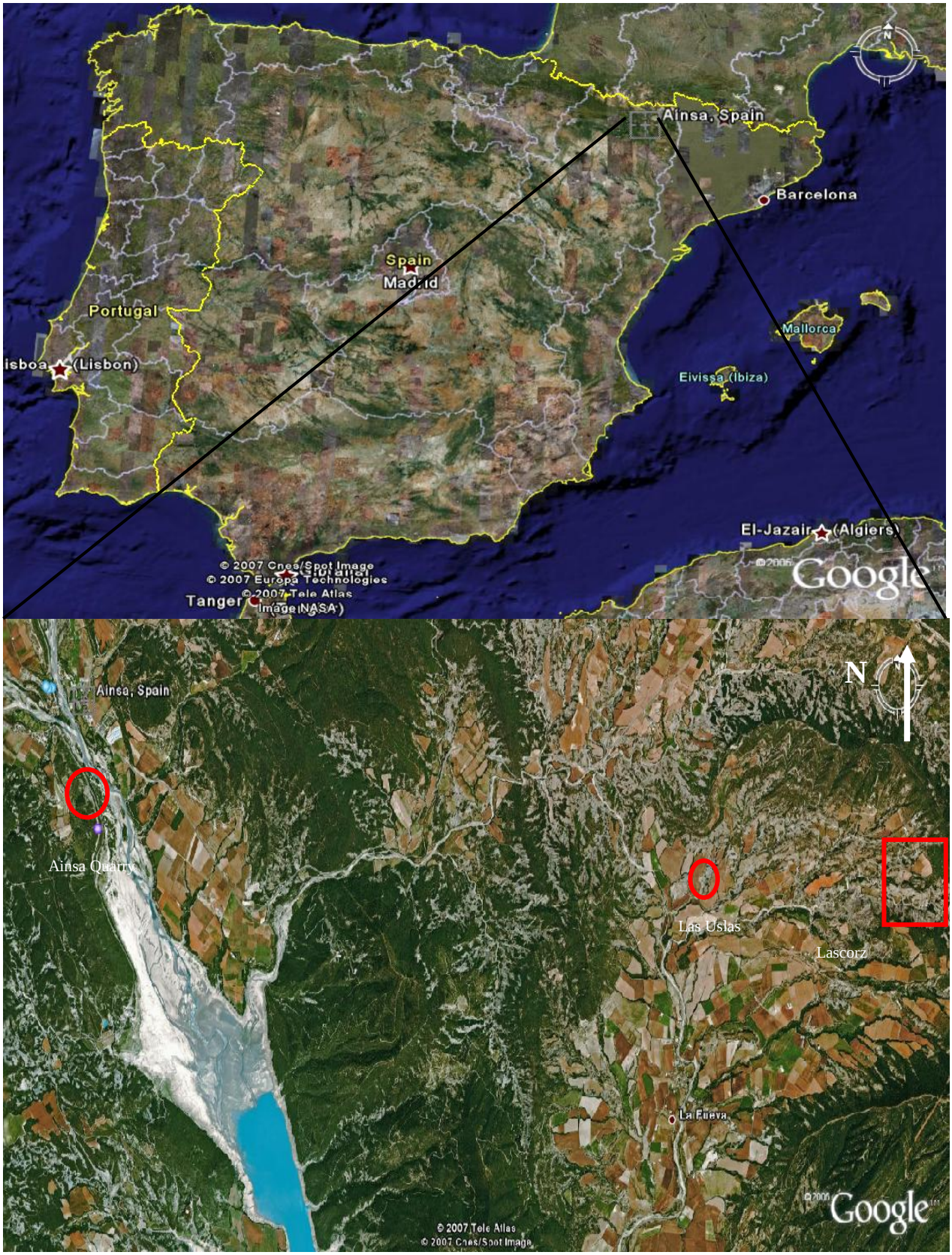

Figure 1.1: Area of focus in this paper. The different localities were the field work was done, are marked on the figure. Maps from GoogleEarth™ (2008).

During field work, some of the structures were located at inaccessible heights. To get access to structures located in altitudes up to three meters above the ground, a ladder was used.

Thin sections were prepared from two rock samples with the purpose of investigating host rock properties and nature of fracture fill.

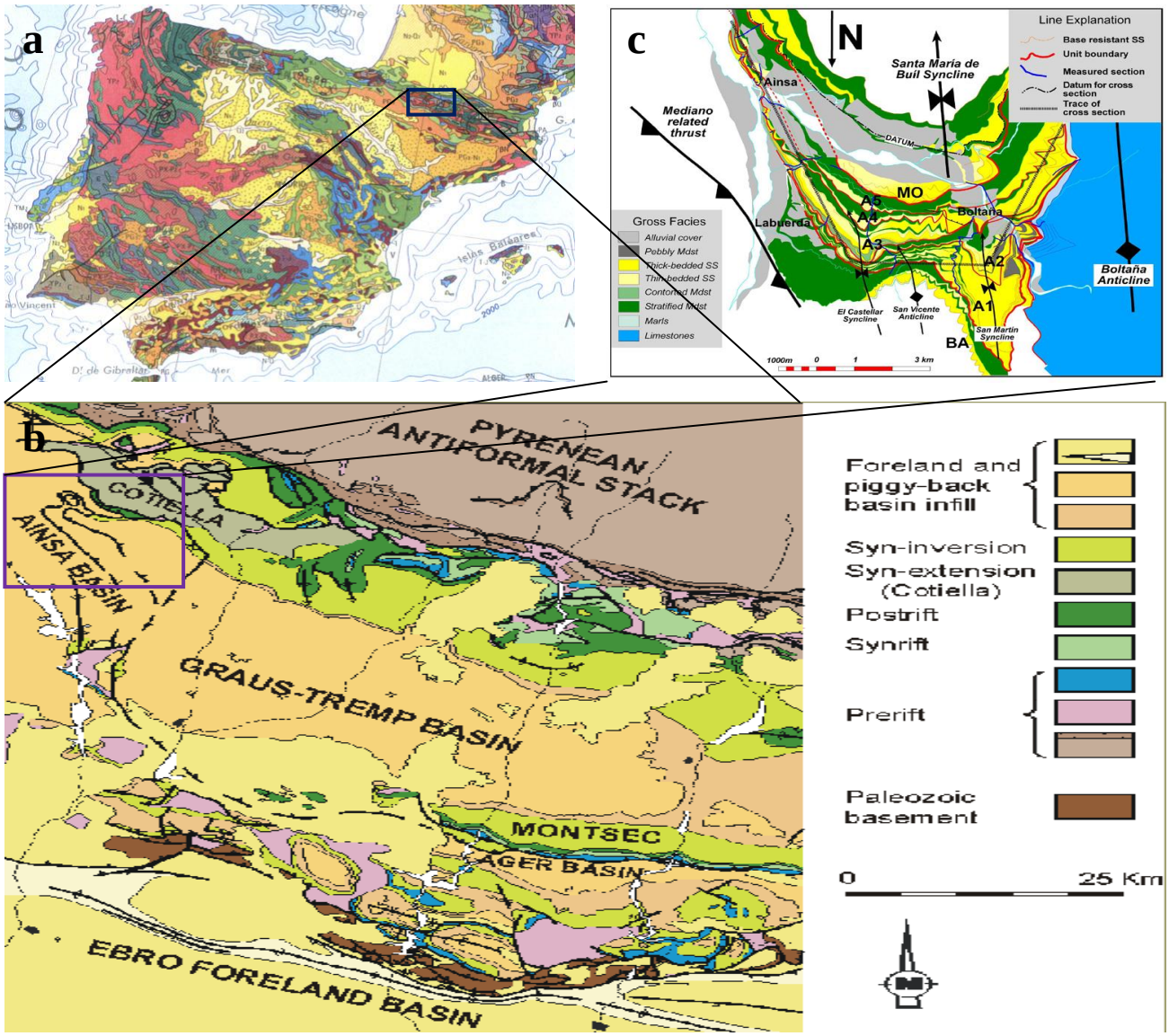

Figure 1.2: a) Geological map of the Pyrenees (DiMaggio, 2005). b) Geological map of the south-central Pyrenees From Melick et. al. (2004). Structural map of south-central Pyrenees. From Melick et. al. (2004).

1.3 – Field maps, equipment and software

Structures illustrated in structural maps are represented by following structures:

- Strike and Dip:
- Fold axis:
- Lineation:
- Thrust:
- River:
- Anticline:
- Syncline:

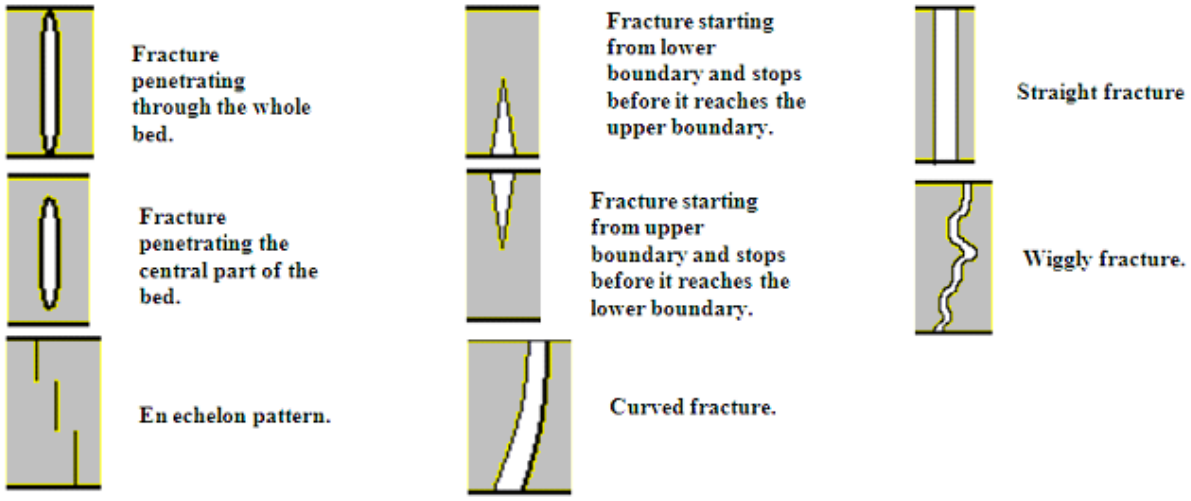

Figure 1.3: Fracture patterns of fractures measured in the study area.

The different fracture patterns are either straight, wiggly or curved, together with either penetrating the whole bed, penetrate central parts of the beds or penetrating from central parts of the bed towards upper or lower layer boundary (figure 1.3). Fractures may also have an en echelon architecture.

Equipment

The equipment used during the field work were Magelan GPS, to get the correct position on the map, and Silva compasses, to measure strike and dip of bedding and fractures together with strike and plunge of fold axes and lineations.

Software

GoogleEarth™ (2008) and GoogleMaps™ (2007), together with aerial photos gathered from http://sitar.aragon.es/en/Vuelos_3D_en.html (Aragon 3D, 2007), were used as a regional mapping reference.
Geological map and cross-sections of the study area are managed out in Adobe Illustrator.

To illustrate measurements taken during field work, Stereowin, developed by Rick Allmendinger, are used. This is a software developed for plotting measurements of strike and dip of bedding and fractures, strike and plunge of lineation and to find a direct value of fold-axes. The program, and more detail about it, can be downloaded from the developer's homepage: http://www.geo.cornell.edu/geology/faculty/RWA/, for free.

1.4 - Terminology

In this section, definitions of the terms used later in this paper are described.

When measuring strike and dip of bedding and fractures, together with strike and plunge of lineation's and fold axes, the right hand rule is used. According to the right-hand rule, the strike of the structure is measured so that the down-dip direction is on the right side of the compass (Davis & Reynolds, 1996).

In sedimentary rocks, bedding planes represent time planes in the rock (Whitten, 1969). These beds are primary structures and are deposited horizontally. Sets of parallel beds are referred to as S-surfaces (Sander, 1948). S-surfaces are designated S_0, S_1, S_2...S_n. Here, S_0 is referred to as primary bedding plane, S_1 is fracture sets and S_2 is schistosity. S-surfaces, such as bedding, foliation and schistosity, are distinguished from S-planes. S-planes are not

visible in a hand-specimen, but they represent a statistically preferred orientation of minerals present in the rock.

Lineation is defined as a linear fabric element, which means that one dimension is much longer then the two others (Van der Pluijm & Marshak, 2004). The most common type of lineations is the *intersection of S-surfaces*, which occur in folded rocks where axial-plane foliations have developed. *Growth of minerals* is a second type of lineations, which often occur in the foliation plane, on shear surfaces and in the plane of mylonitic foliation. This is growth of minerals that reflect the geometry of the plane of growth. A third type of lineation is the *surface lineation*. This includes both the intersection of S-surfaces, described above, and *slip lineation* which develop on surfaces were the rock on each side move in opposite directions (figure 1.4).

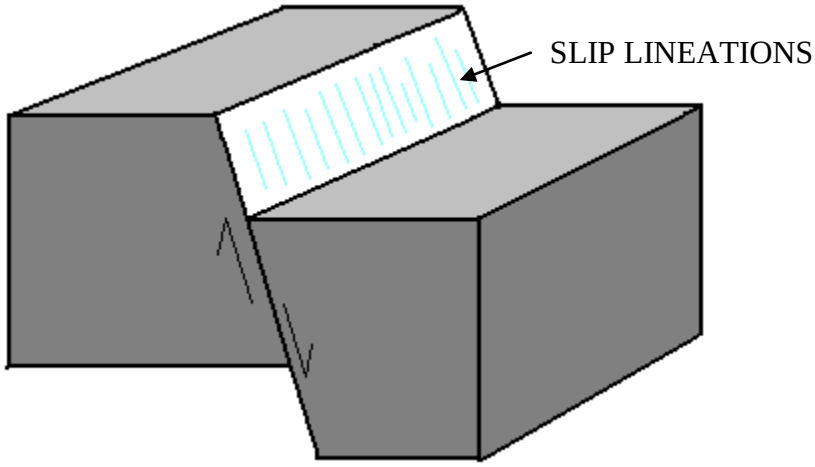

Figure 1.4: Illustration of slip lineation on an extensional fault plane. This kind of lineation can occur on every surfaces where two bodies of rock move in opposite direction relative to each other. Developed from Marshak and Van der Pluijm (2004).

Fold nomenclature

A fold is a distortion of a volume of material that manifests itself as a bend or nest of bends in linear or planar elements within the material (Hansen, 1971). The fold axis is a geometric, but only imaginary, linear structural element that does not possess a fixed location (Ramsay, 1967). The fold limbs represent the two sides of the hinge line (figure 1.5). Fold axes were measured directly in the field wherever possible, and in addition constructed as a function of the S_0 measurements in stereonet, which is termed the β-axes.

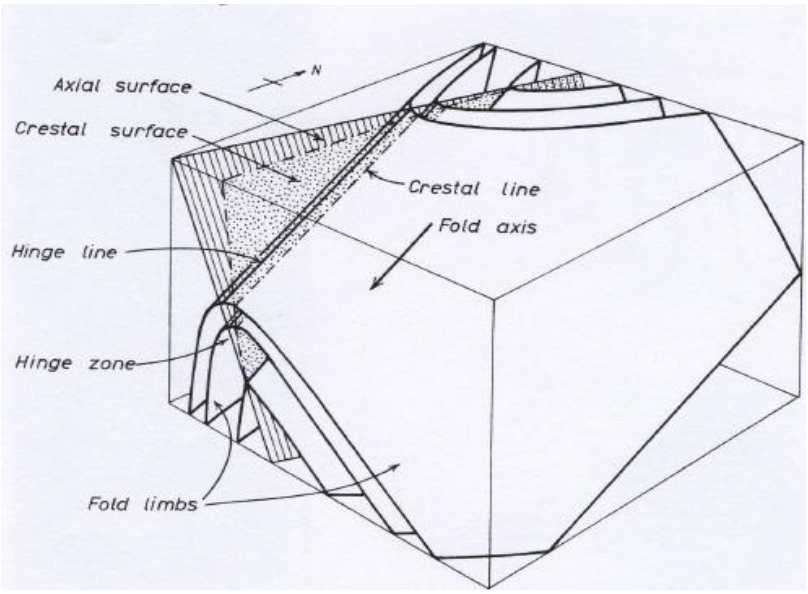

Figure 1.5: Illustration of a fold with its main components. From Ramsay, 1967.

Folds are often associated with different types of foliation (Scrope, 1825), which may, or may not; coincide with another S- surface, such as bedding (Fairbairn, 1954). Foliations are often developed in the same process as folds, and show a consistent geometrical relationship with their axial planes (Darwin, 1846; Stearns, 1964; Price, 1966; Whitten, 1969). Foliation parallel to bedding is very common in areas subjected to flexural-slip and slip folding. Lithological layers may then show foliation parallel to the axial plane and to the layering (S_0) (Whitten, 1969). Cleavage is a type of foliation, whereby the rock tends to split parallel to the cleavage surfaces. Axial planar cleavage forms parallel to the axial plane of folds (fractures related to folding is described in more detail in appendix I).

Folds may be classified by their isogons. Isogons are lines between areas of equal dip or apparent dip on the profile plane between two surfaces represented in the fold. This represents the relationship between the two surfaces. The inner surface is taken as the reference point regarding the direction of isogon convergence. Five patterns are recognized. These are:

1a Folds with strongly convergence isogons.

1b Folds with parallel isogons.

1c Folds with weakly convergence isogons.

2 Folds where both inner and outer curves are identical and the isogons are parallel.

3 Folds where the inner bed has a less curvature than the outer bed.

This is the Ramsey's fold classification and is illustrated in figure 1.6 (Ramsay, 1967).

The shape and opening of folds are recorded to say something about the magnitude of compression during folding. An open fold appears during less shortening of the layers than what is expected for a tight fold (figure 1.7) (Ramsay, 1967).

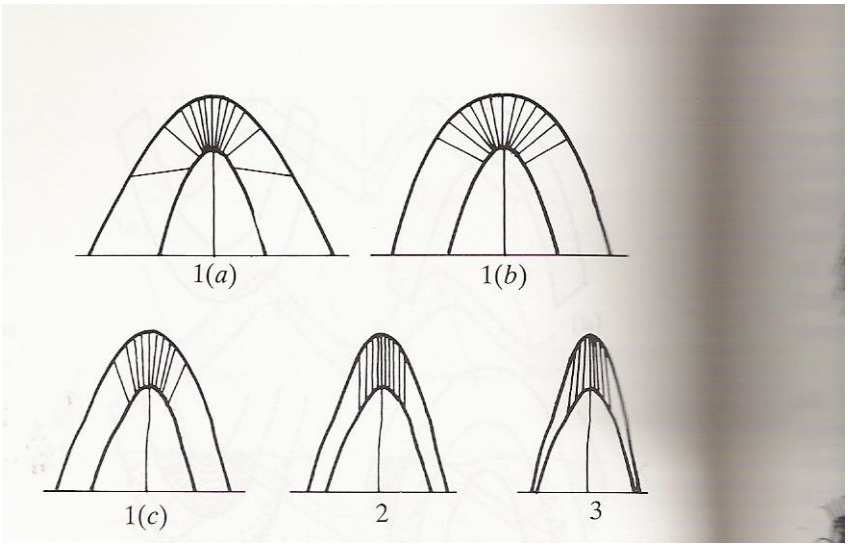

Figure 1.6: Ramsay Classification of folds. From Ramsay (1967).

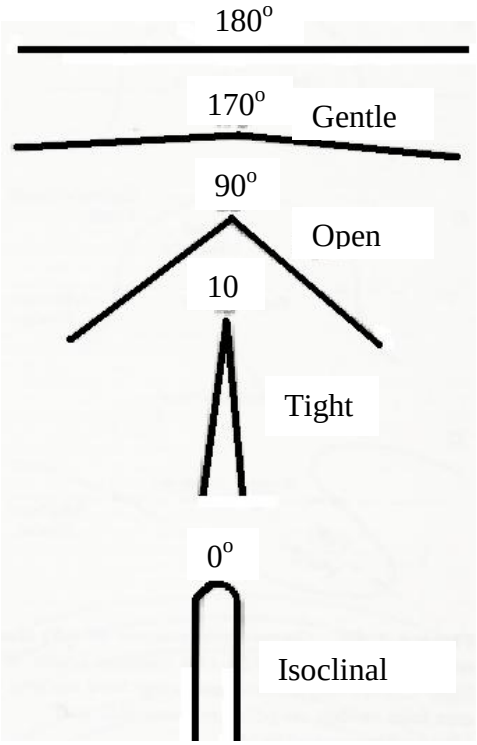

Figure 1.7: Fold classification according to tightness. The classification is based on the angle between the two limbs. From Davis & Reynolds, 1996.

The fabric of a deformed rock defines the orthogonal a- b- and c- axes defined by Sander (1948) (figure 1.8). Fabric is defined as the relationships of planar and listric structures, like bedding, cleavage etc, to texture in rocks.

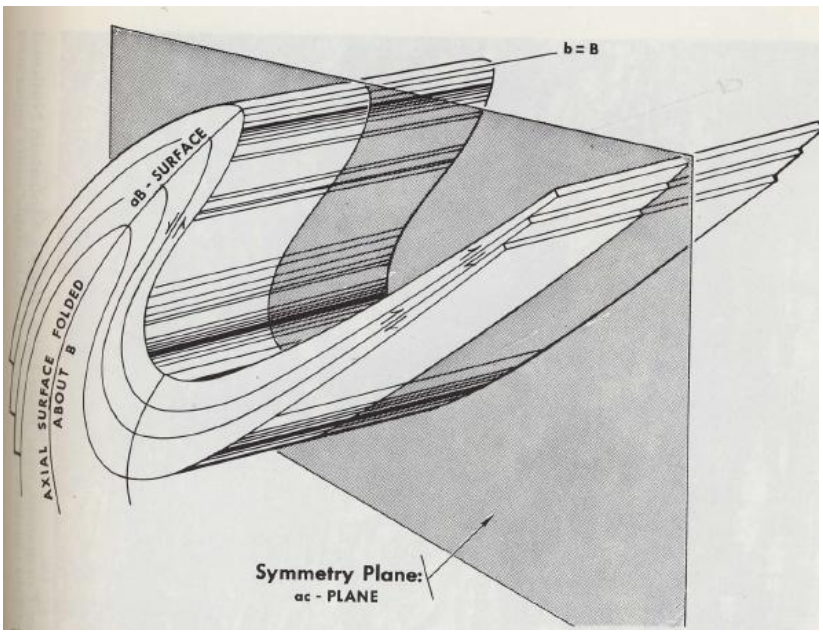

Figure 1.8: Relationship between the different planes represented within folds. From Whitten, (1969).

The b-axis is the plane parallel to the fold axis (i.e. the β).Normally, the most prominent direction of foliation is parallel to the ab-plane. The ac-plane is perpendicular to the fold axis, then also the b-plane, whereas the c-axis is parallel to the direction perpendicular to the ab-plane, but can vary throughout the fold since the a-axis can vary from point to point within the fabric (Sander, 1948; Whitten 1969). The direction of slip is along the a-axes, which by definition is oriented differently in each point of flexure. The b-axis is homogeneous throughout the fold, and is therefore, by definition, parallel to the fold axis, i.e. the β-axis. As the figure illustrates, the aβ-plane is the plane of slip, while the deformation plane is perpendicular to the β (i.e. the ac-plane).

Often, minor folds are observed on one or both limbs of a larger fold, with similar orientations. These minor folds are then referred to as parasite folds, developed in the same stress field as the main fold (Van Der Pluijm & Marshak, 2004).

Folds may also buckle as a result from the application of compressive stresses parallel to the layers (Twiss & Moores, 1992). These folds are then referred to as buckle folds (figure 1.9). This type of folds is often recognized by lineations oriented perpendicular relative to the fold axis on upper surface of bedding. Axial surface foliation related to buckle folds, are dipping perpendicular relative to bedding (S_0).

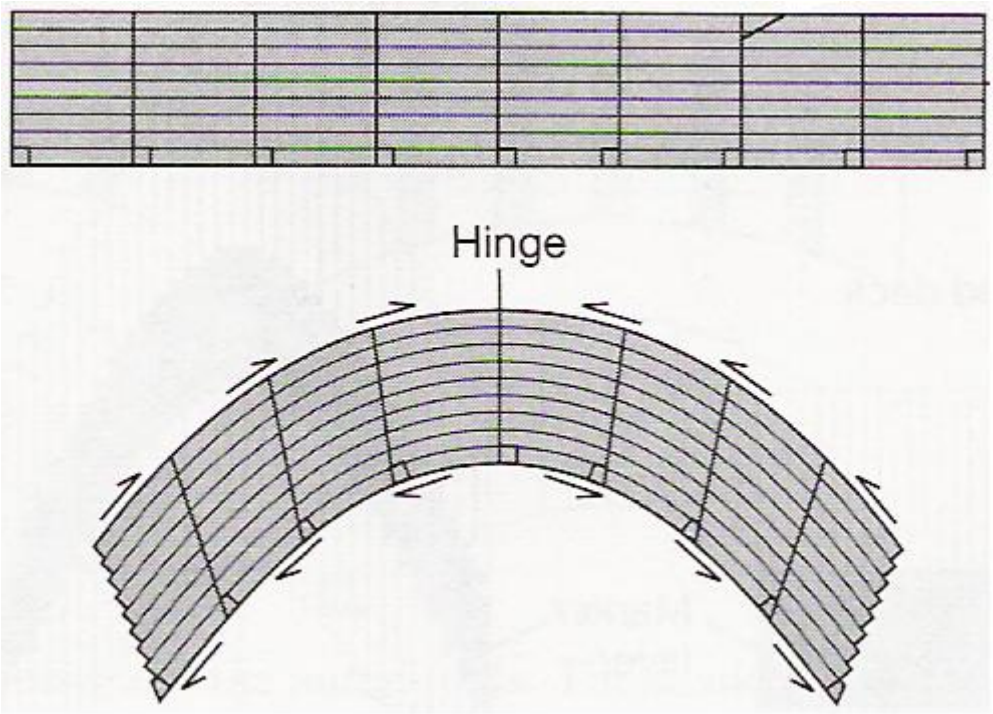

Figure 1.9: Geometry of a buckle fold after flexural-shear folding. From Twiss & Moores, 1992.

Fracture terminology

A population of fractures is a certain number of fractures that have the same properties, and presumably are genetically related. Such properties may be orientation, opening and displacement, geometry and nature of fracture infill. Fractures can be classified into three groups:

1. Dilation fracture/joints.
2. Shear fractures.
3. The hybrid, shear-dilation fractures.

Dilation fractures, i.e. joints, are referred to as Mode 1 fractures. Mode 2 and Mode 3 fractures are considered as shear fractures (figure 1.10; Hatcher, 1990).

Stress (σ) is defined as force (F) divided by area (A) (Davis, 1984).

$$\sigma = \frac{F}{A}$$

The relationship between the different stress directions are, per definition:

$$\sigma_1 > \sigma_2 > \sigma_3$$

These are further referred to as maximum (σ_1), intermediate (σ_2) and minimum (σ_3) principle stresses

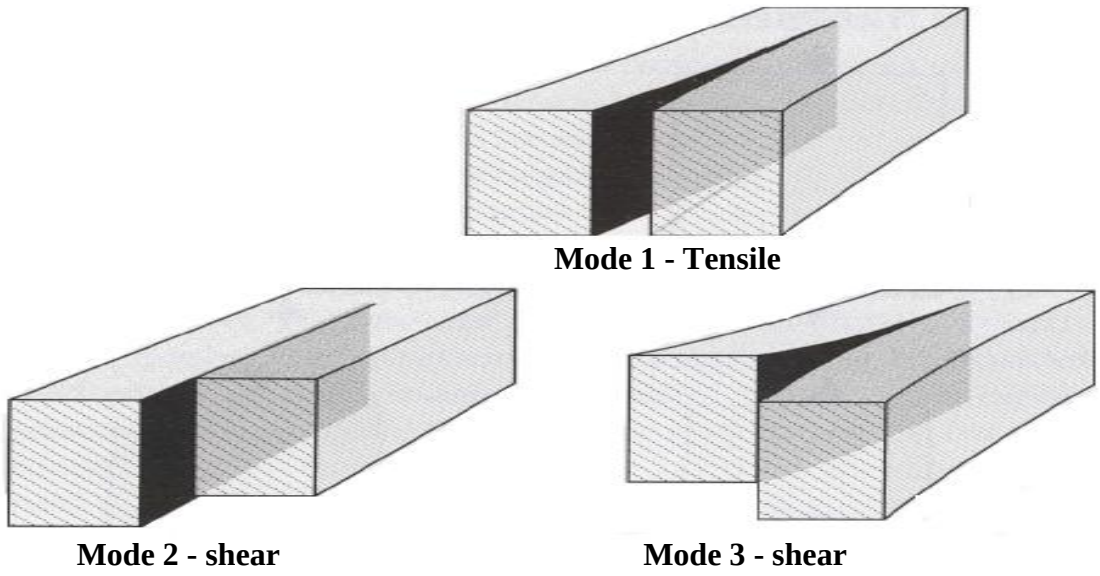

Figure 1.10: The three different modes of fractures. Developed from Fossen & Gabrielsen, 2005.

The orientation of the fractures, their mode (mode 1, mode 2 and mode 3 fractures) and the type of fracture fill are analyzed to deduce the principle stress at the time of formation. Mode 1 fractures, i.e. tensile fractures, develop parallel to the maximum stress axis (σ_1) (figure 1.11; Van Der Pluijm & Marshak, 2004). They are typical for cases were the magnitude of the maximum and minimum stress axes are of similar order of magnitude (Fossen & Gabrielsen, 2005). This is commonly the case near the surface and in cases with abnormally high fluid pressure. Mode 2 fractures, i.e. shear fractures, develop at an angle of 20-30^o to the maximum stress axis. This is referred to as the "sliding mode", since rock on one side of the crack surface has moved parallel to the strike of the fracture. Mode 3 fractures are the second type of shear fractures. These are referred to as "tearing mode", since rock on one side of the fracture has moved perpendicular to the strike of the fracture.

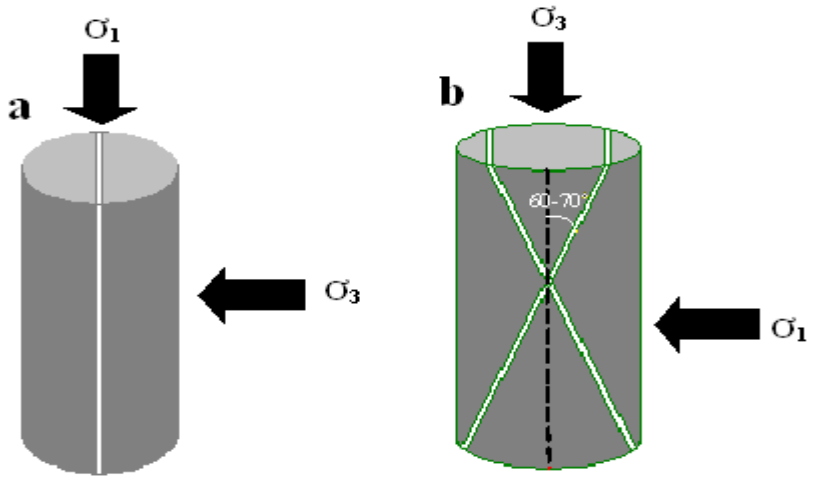

Figure 1.11: Fracture development within a cylinder possessed for different differentiated stress. a) Maximum stress axis is vertical, and the fracture is then also striking perpendicular to σ_1. b) Minimum principle stress axis is vertical, and maximum stress axis is horizontal. The fractures are then developing at an angle of 20-30^o to the maximum stress axis (σ_1).

The different stress axes are also referred to as σ_v, σ_H and σ_h, which are vertical stress and the maximum and minimum horizontal stress axes, respectively (Anderson, 1951). These three stress axes represent the three main stress directions σ_1, σ_2, and σ_3. Anderson formulated the theory of three tectonic regimes (Fossen & Gabrielsen, 2005) (figure 1.12):

- $\sigma_v > \sigma_H > \sigma_h$ - Extensional regime
- $\sigma_H > \sigma_v > \sigma_h$ - Strike slip regime
- $\sigma_H > \sigma_h > \sigma_v$ - Contractional regime

The vertical stress is defined as:

$$\sigma_v = \rho g h,$$

were ρ represents the density of the rock, g is the gravity and h is the thickness of the overburden (Anderson, 1951). The maximum horizontal stress is defined by the vertical stress together with a tectonic contractional stress regime:

$$\sigma_H = \rho g h + \sigma_t,$$

where σ_t is the contractional tectonic stress.

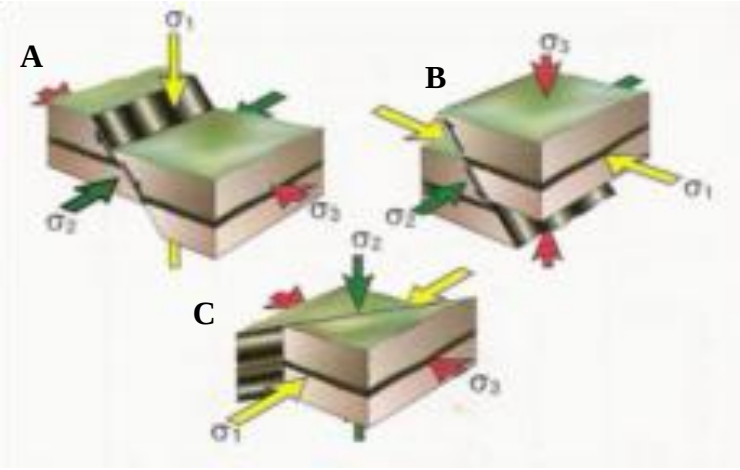

Figure 1.12: Illustration of the three different cases of stress distribution. A: Extensional faulting, were maximum stress axis is vertical and minimum stress axis is perpendicular to the strike of the fault. B: contractional fault (thrust), were maximum stress axis is perpendicular to the strike of the fault and minimum stress axis is vertically. C: Both maximum and minimum stress axes are horizontal, while intermediate stress axis is vertically. From Fossen & Gabrielsen (2005).

Orthogonal fracture pattern can develop during compression when maximum horizontal stress axis rotates by 90^o (e.g. Ghosh, 1988; Dunne, & North, 1990; Dunne and Hancock, 1994; Aydin et.al., 2002), a rotation which also can occur during regional uplift and erosion because of release of locked in stress (Friedman, 1972). Orthogonal cross-joints may also form in rocks subjected to biaxial extension. Then, the stress axis parallel to the systematic joints already present in the rock becomes the axis of maximum tensile stress, resulting in jointing perpendicular to the already existing fracture set.

Scattering of measurements within a stereonet are expected to be found in areas representing a fault zone. These are interpreted as Conjugate shear fractures, which are often found in relation to folds and faults (figure 1.13). There are two sets of fractures oriented approximately 60^o to each other and with opposite sense of shear (Twiss & Moores, 1992; Alhgren et. al., 1999). In a stereonet, this may result in poles plotted in all four quadrants. The intermediate stress axis (σ_2) is always parallel with the line of intersection of the shear fractures, whereas maximum stress axis (σ_1) is oriented 30^o from the individual fractures. Fault planes are often associated with closely spaced faults, numerous joints and shear fractures, and brecciation (Davis & Reynolds, 1996).

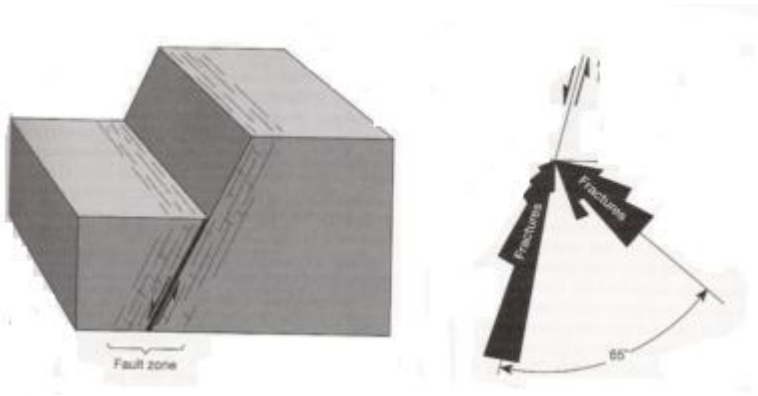

Figure 1.13: Drawing of fracture development within a thrust zone. Figure from Moore & Twiss (1992).

Sometimes, thrusts do not penetrate up to the surface, but stops in the subsurface. This can then result in a fold above the thrust, a fault-propagation fold (figure 1.14a; Van der Pluijm & Marshak, 2004). Fault-propagation folds contain a fault ramp with associated fold above. The folding of strata above the fault develops simultaneously with the faulting. In cases were displacements along the fault diminish before it penetrates the surface, it is referred to as a blind fault. These may later be revealed after erosion of overburden (Twiss & Moores, 1992). Together with fault-propagation fold, detachment folding are distinct scenarios related to fold-thrust interaction in overthrust terrains (figure 1.14b) (Jamison, 1987). Detachment folds develop at the termination of a thrust where displacement is transferred into folding above the thrust sheet, or within the interior of a thrust sheet where fault displacement gradient changes abruptly (Dunne, 1986; Clevis et. al., 2004; Hayes & Hanks, 2008). Both fault-propagation fold and detachment fold may often evolve into splay faults. These are minor faults which branches out from the larger fault, often at their termination point (Jackson et. al., 2005; Fossen & Gabrielsen, 2005). The third fault-related fold mechanism is the fault-bend fold. Fault-bend folds are formed when beds are displaced along a thrust with ramp-flat geometries (Davis & Reynolds, 1996). A fold form above the thrust when the thrust cuts up through the stratigraphic section from lithologically controlled flat to another (figure 1.14c).

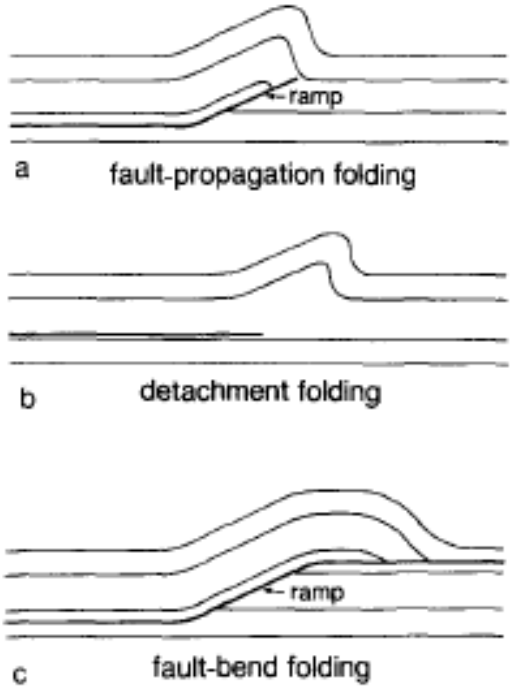

Figure 1.14: a) Illustration of fault-propagation fold. b) Illustration of detachment folding. c) Illustration of fault-bend fold. Figure from Jamison (1987).

Tear faults are defined as small scale, local faults that are associated with other structures such as folds, thrust faults and normal faults (Mueller & Talling, 1996). In a thrust belt, tear faults strike perpendicular to the thrust front and fold axis. Tear faults may form along propagating thrust sheets as they start to segment the thrust sheet and act as lateral boundaries that separate the thrust units. They may be a result of drastic lateral changes during propagation of the thrust front by differential shortening of the thrustal sheet.

Often, structures can be related to sedimentation, and develop as syn-sedimentary structures. These structures are presumably generated in response to intra-basinal stresses associated with surface gradients in the basin. They are distinguished from mechanically and tectonically developed structures by the thickening of the beds towards the fault, which makes them look wedge shaped, the faults are not penetrating all beds in a section, meaning that sediment accumulated after displacement along the faults, and roundness of beds at the boundary between two lithologies at the fault (figure 1.15) (e.g. Collinson, 1994; Bhattacharya & Davies, 2001; Bouroullec et.al., 2002).

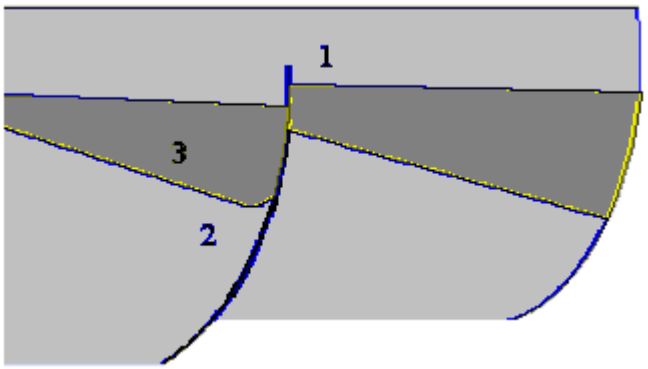

Figure 1.15: Illustration of the three characteristics regarding growth faults. 1: Fault is not penetrating bed above. 2: Roundness of corner close to the fault. 3: Wedge shaped beds, thickening towards the fault.

In areas with several different fracture populations, mode, orientation and fracture fill are used to distinguish between the different populations. The age of the populations relative to each other is also investigated, and is seen by offset of any fractures belonging to one population by a fracture belonging to another population (Price, 1966). The population represented by the fracture that has been offset, is then youngest.

Chapter 2 – Plate tectonic setting

To understand the development of the Pyrenees is of principle significance due to its close link between structural geology and sedimentology. This is particularly evident in its southern zone (described in section 3.2) (Mey et. al., 1968; Choukroune & Seguret, 1973; Puigdefàbregas & Souquet, 1986; Bentham et. al., 1992). The counter-clockwise rotation of the Iberia Peninsuela during collision with south-western Eurasia was suggested by Warren (1955) to explain mechanism of formation of the Bay of Biscay. This concept was further developed by Choucroune & Seguret. in 1973, Nijman in 1989 and Sibuet et.al. in 2004 (figure 2.1). The rotational compression of the Pyrenees resulted in an intense compressional folding and thrusting in the eastern Pyrenees, which diminished in both width and intensity westwards, towards the Bay of Biscay.

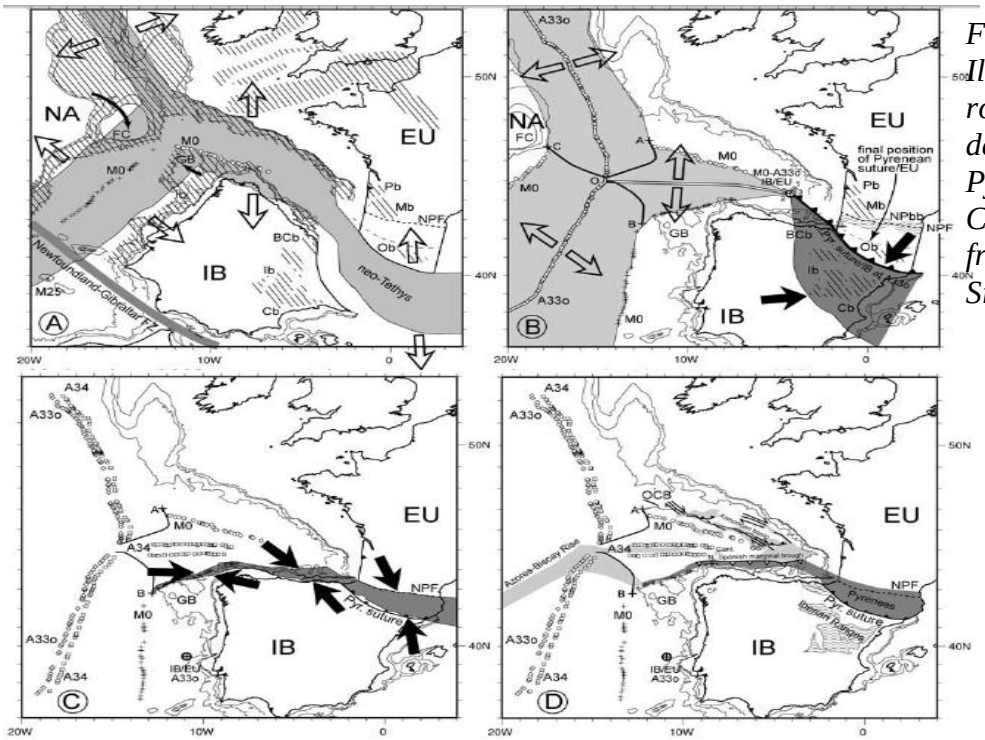

Figure 2.1: Illustration of the rotational development of the Pyrenees. Chronologic time from A – D. From Sibuet et. al. (2004).

There is now consensus that the tectonic processes were the principal driving mechanism for the accumulation of sediments in the Ainsa Basin (Fontana et. al., 1989; Bentham et. al., 1992; Dreyer et. al., 1999; Pickering & Corregidor, 2000; Arbues et. al., 2004). These

writers also discuss how syn-sedimentary tectonics has influenced variations in accommodation space and therefore also sequence stratigraphy. The eastern and western boundaries of Ainsa Basin, Mediano and Boltana anticlines respectively, have been interpreted as transport-oblique lateral thrust ramps (Atkinson et.al, 1987), but more recent investigations suggest that at least the Boltana anticline is a fault-propagation fold (Arbues et.al, 1998; Fernandez et.al, 1998).

The investigation on how the Ainsa Basin was formed has been increased during the last two decades. That the Ainsa Basin developed as a piggy-back basin on the propagating frontal thrust belt of the evolving Pyrenees during early to mid Eocene, was first suggested by Fontana et. al. (1989), and later supported by Bentham et. al. (1992), Arbues et. al. (1999) and Pickering & Corregidor (2000).

In Ainsa Basin, lenticular sandstone bodies are encased in a mudstone-dominated succession (figure 2.2). These sandstones were first mentioned by Mutti & Lucchi (1972), and interpreted as slope features thought to represent the main feeder channels of the thick and laterally extensive basinal turbidite succession, which developed west of the Boltaña anticline. This concept has been further investigated by Fonnesu et. al. (1981); Mutti & Normark (1987, 1991); Fontana et.al. (1989); Schuppers (1995); Clark (1995); Clark and Pickering (1996); Cronin et. al. (1998) and Pickering and Corregidor (2000), who also developed a model for the sedimentation and depositional setting of the Ainsa sandstones.

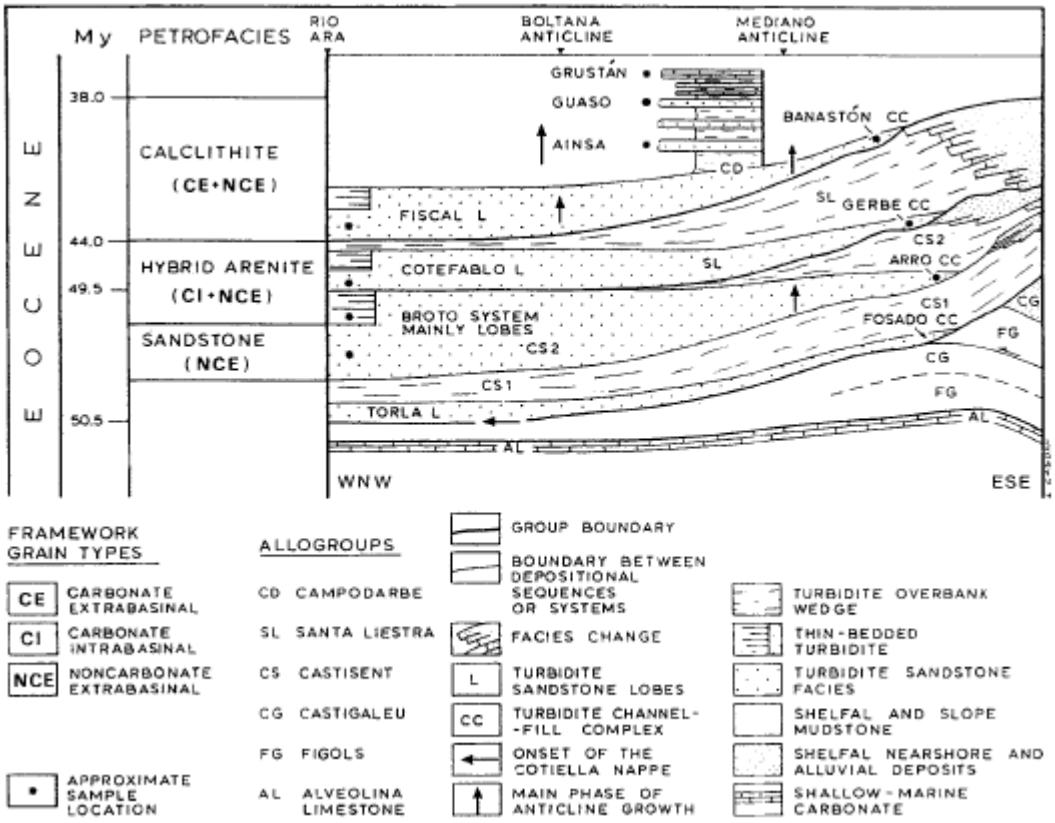

Figure 2.2: Turbidite sandstone bodies located in the south-central Pyrenees. This also comprises the area between Boltaña anticline and Mediano anticline, were Ainsa Basin is located. Figure from Fontana et. al. 1989.

Chapter 3 – Development of the Pyrenees

3.1 – General basin description of the Pyrenees

During development of the Pyrenees, several foreland basins were formed in the southern part of the orogen (see chapter 2). A foreland basin is defined as the sedimentary basins between the front of a mountain chain and the adjacent orogen (Allen et. al., 1986). There are two genetic classes of these, mainly the retro-arc and the peripheral foreland basins (figure 3.1). The retro-arc type involves subduction of oceanic crust during collision (Dickinson, 1974), whereas the peripheral type is linked to continent – continent collision, and is the class represented in the southern Pyrenees.

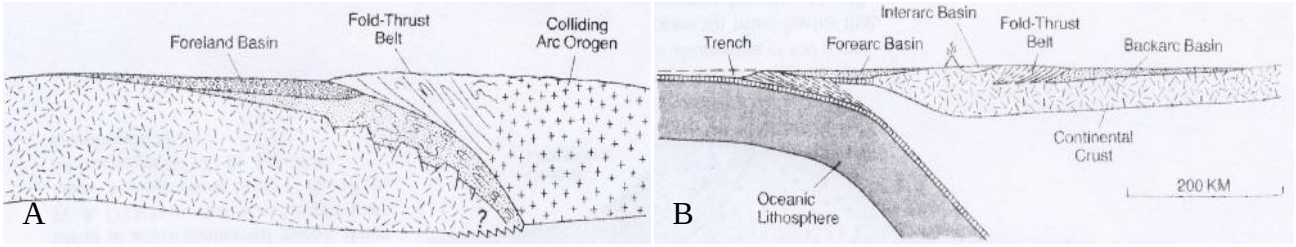

Figure 3.1: Illustration of formation of foreland basins (Davis, 1984). The Pyrenees foreland basins are formed in a continent – continent collision, i.e. A. B illustrates continent – oceanic collision.

The term "piggy-back basin" is used for a thrust based basin marginal to a foredeep (Friend & Ori, 1984). These basins develop were the deformation of the foreland basins has progressed under the basin, so that it rests on moving thrust sheets. Figure 3.2 illustrate the evolution of piggy-back basins from within a foreland basin.

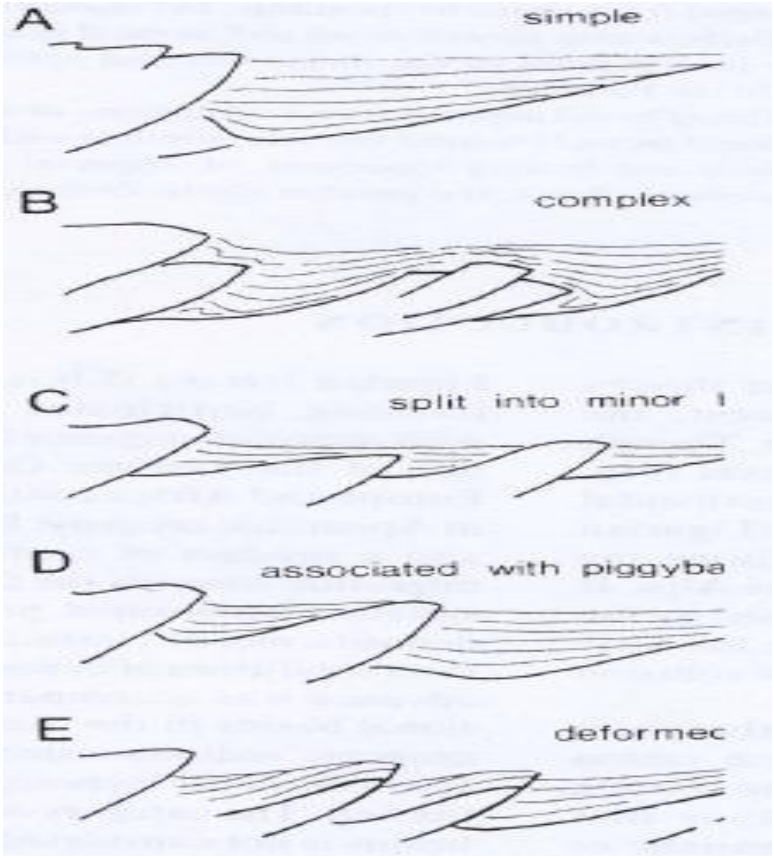

Figure 3.2: Evolution of a foreland basin into piggy-back basin. A simple foreland basin in A, and the thrust sheet prograde and split below the basin in B and C, before the piggy-back basin is established in D. In E, the piggy-back basin becomes deformed (Lucchi, 1984).

3.2 – General tectonics of the Pyrenees and main structural units

The Pyrenean orogen is located at the border to France in the north-eastern Spain (3.3). It is an E – W trending orogen that developed in the northeastern corner of the Iberian Peninsuela, formed during Late Cretaceous – Miocene convergence and limited northward underthrusting of the Iberian plate beneath the Eurasian plate (Bentham, 1992). The onset of contraction associated with the collision between the Iberian plate and the Eurasian plate was strongly diachronous from east to west. Figure 3.4 illustrate a cross-section of the Pyrenees from south to north at present day.

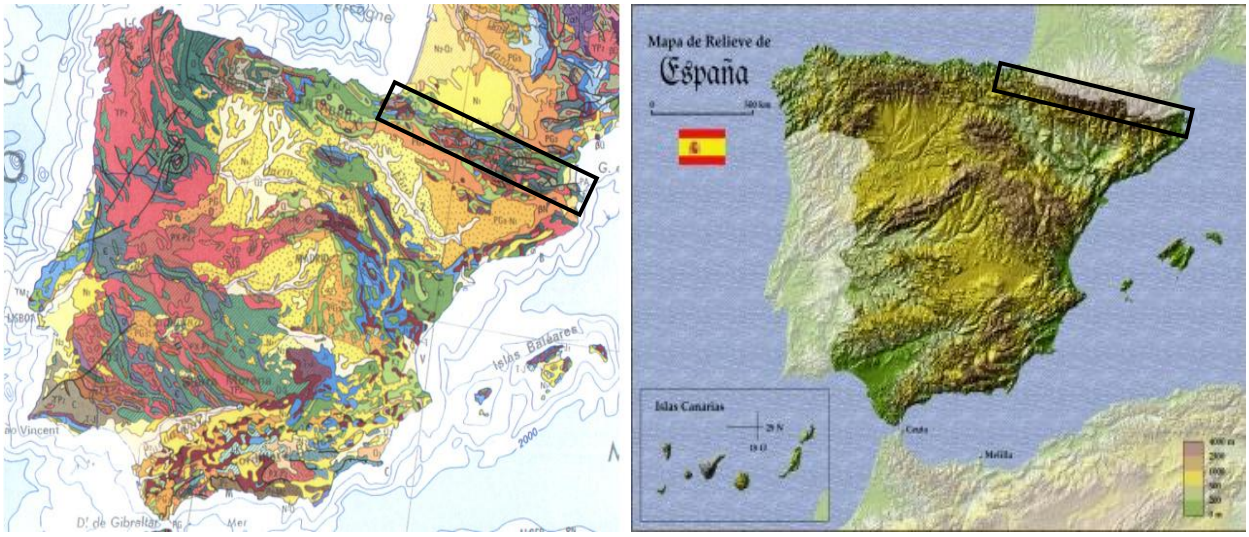

Figure 3.3: Geological and topographic map of the Iberian Peninsuela. The Pyrenean orogeny is located within the dark rectangle northeast of the two maps. Maps from DiMaggio, 2005.

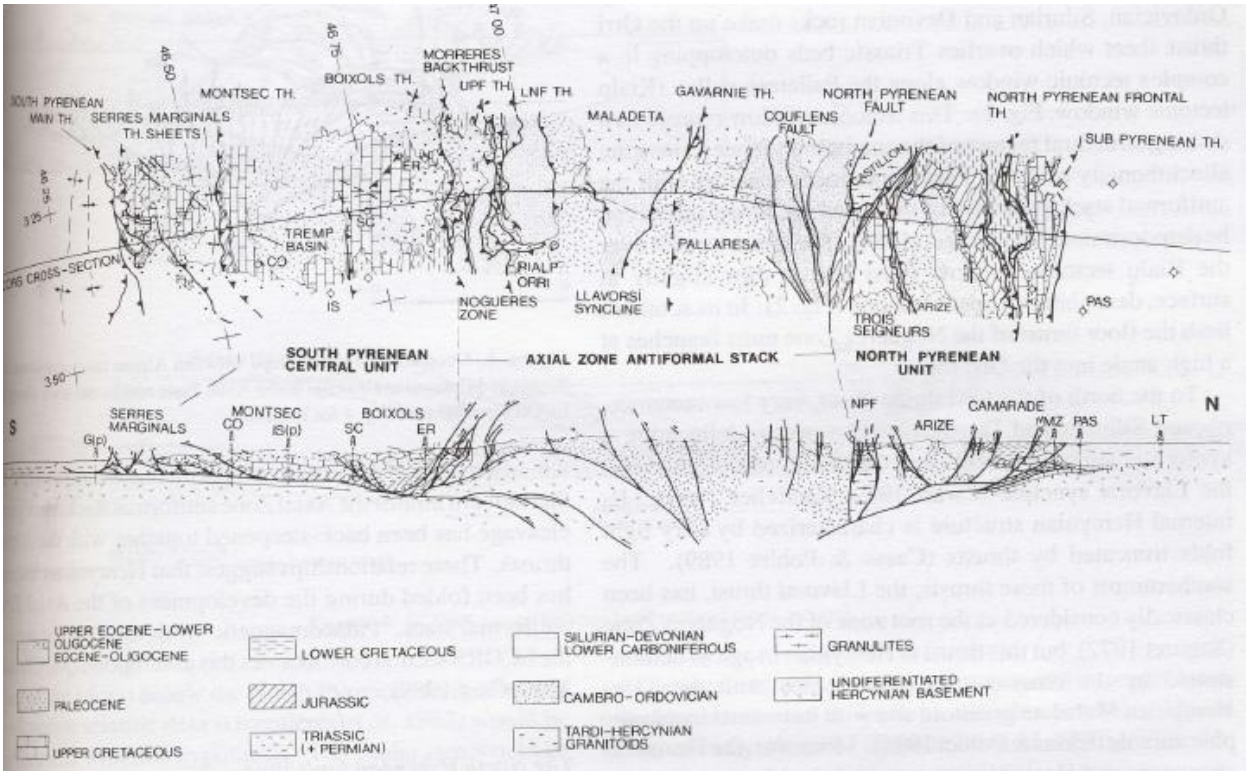

Figure 3.4: Cross-section of the Pyrenees from south to north, along the ECOR's line. From Muñoz et.al. 1992.

Three main zones are recognized representing the Pyrenees. These are the Northern Pyrenees zone, the axial zone and the Southern Pyrenees zone.

The main structures in the Northern zone are steeply dipping faults and folds with steep axial planes. The North Pyrenean fault, which is the most important fracture in the North Pyrenean zone, corresponds to late Hercynian faults in the basement, were the rocks consists of basement blocks with a Mesozoic cover (Puigdefàbregas & Souquet, 1986).

The axial zone of Paleozoic rocks affected by the Hercynian orogeny is flanked by the North Pyrenean and South Pyrenean zones of deformed Mesozoic, represented largely by Cretaceous, strata (Choukroune & Seguret. 1973). Here are also granite intrusions altering the sedimentary rocks close to the contact zones (Adams, 1901).

The evolution and infilling of the Southern Pyrenees zone can be divided into four stages.

The first stage represents the extensional rift basin development in early Cretaceous (Puigdefabregas & Souquet 1986). The first Pyrenean thrusts represent reactivation, in upper Santonian times, of these extensional faults. In front of thrusts, deep E–W elongated sedimentary basins were formed and filled in with Upper Santonian to Campanian age turbiditic deposits. The first fractures found in the Pyrenees were developed as stylolites and possible hydraulic fractures during this rift event (Whaley, 2008).

The second stage, between latest Maastrichtian to Palaeocene, is represented by formation and infill of foreland basins in the southern Pyrenees (Mey et. al, 1968). According to Muñoz (1992), the early Cretaceous extensional faults were completely inverted in Palaeocene times. After inversion of the extensional faults, the upper crust recovered its pre-Cretaceous initial length. The sediments accumulated in the southern Pyrenean foreland basins, after inversion of the extensional faults, and are characterized by uniform shallow-water deposits (Muñoz et. al. 1992; Vincent, 1999). One example of such inverted extensional faults is the Boixols thrust (figure 3.5). This is one of the dominating structural features in the southern Pyrenees, with several kilometric E-W trending folds (Bond & McClay, 1995).

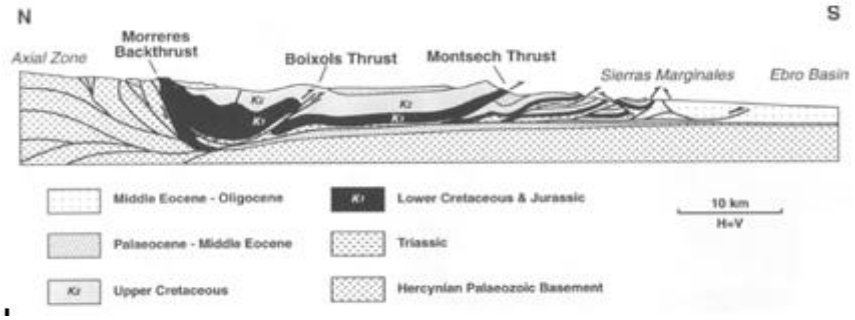

Figure 3.5: Cross-section of the Southern Pyrenees from north to south (Bond & McClay, 1995).

The third stage was between Lower and Middle Eocene. At this time, a transgression of the southern Pyrenean foreland basins resulted in infilling of turbiditic sediments. Thrust sheet geometries controlled the arrangement of the turbidites and coeval shallow marine to continental deposits (Muñoz et. al., 1992; Verges et. al, 2002). At this stage, the foreland basins started to evolve further into piggy-back basins, (figure 3.6).

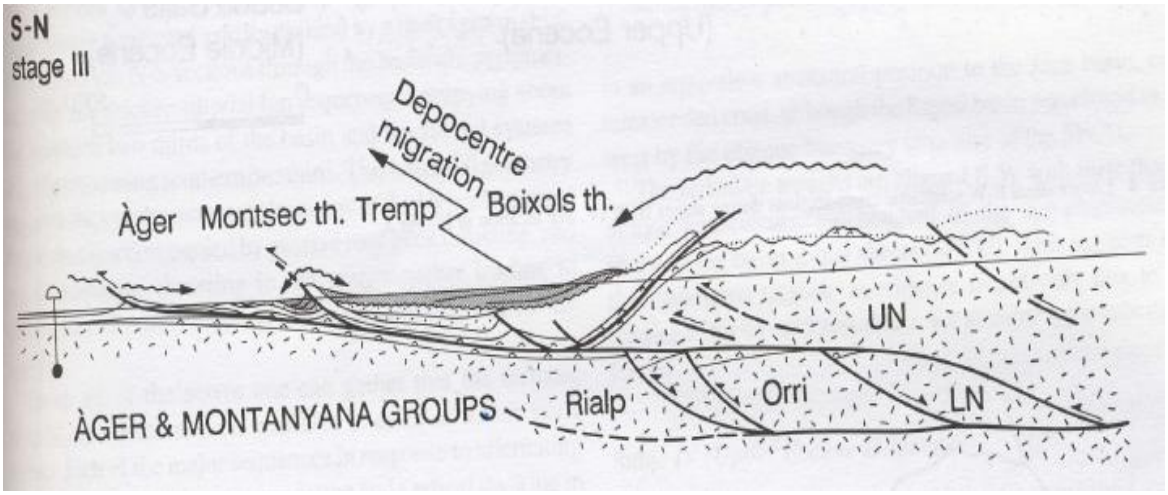

Figure 3.6: Cross-section of the southern Pyrenees during development of the foreland basins (Muñoz et.al, 1986).

The fourth stage, (late Eocene to Oligocene) is characterized by final infilling of the earlier turbidite basins by deltaic deposits. The facies distributions were controlled by the geometry of the thrusts. The structural evolution in this period was controlled by the growth and development of the antiformal stack in the inner part of the mountain chain (i.e. the axial zone antiformal stack). The piggy-back migration continued further southwards in this period, illustrated in figure 3.7 (Puigdefabregas & Souquet, 1986; Muñoz et. al. 1992).

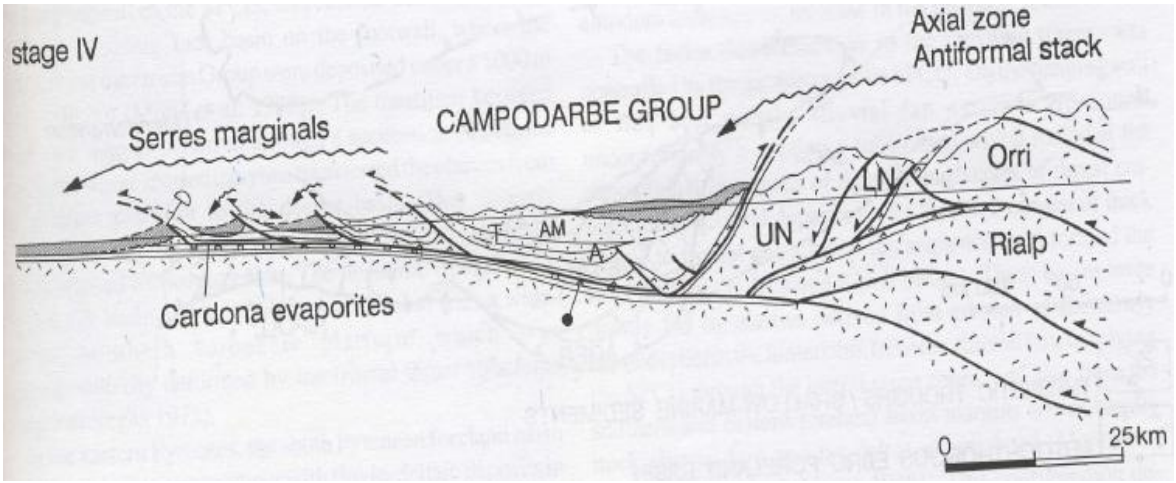

Figure 3.7: Cross-section of the southern Pyrenees from north to south during development of the piggy-back basins (Muñoz et.al, 1992).

3.3 - Further development of the Ainsa Basin

Three main thrust sheets are present in the south central Pyrenees (Bentham et. al., 1992). These are, from north to south, the Bòixols, the Montsec, and the Sierras Marginales (figure 8), which developed during Late Cretaceous, Palaeocene-Early Eocene and middle Eocene-Oligicene times, respectively, and they link together along their eastern boundary into Segre fault zone oblique ramp. Their western boundary is defined as a diffuse oblique ramp system, where numerous transport – oblique anticlines have developed. Boltaña anticline is an example of such transport – oblique anticlines.

The Ainsa Basin is situated in the south-Central unit of the southern Pyrenees (figure 3.9). This unit is characterized by thrust sheets and is associated with piggy-back basins. The Ainsa piggy - back Basin is located between Boltaña anticline and Mediaño anticline, as its eastern and western boundaries respectively, and has its southern margin defined at the E-W trending Sierra Marginales thrust (figure 3.9 and 3.10) (Bentham et.al., 1992; Mùnoz, 1992).

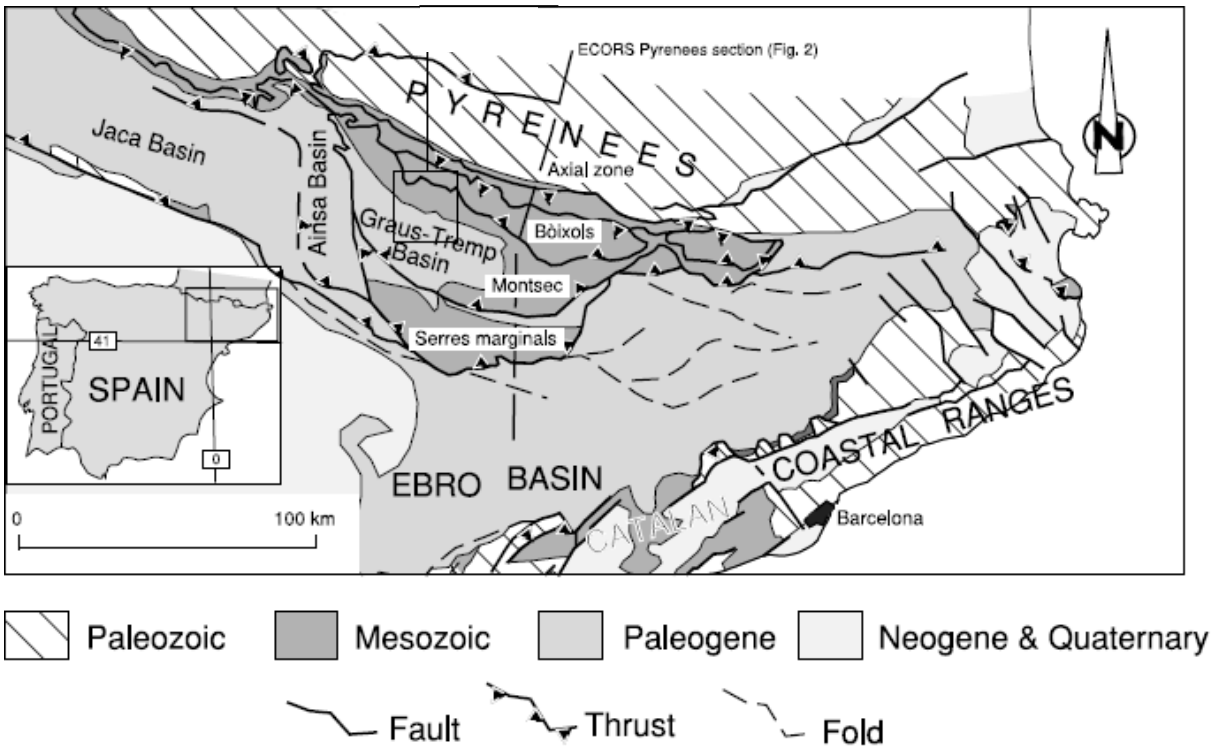

Figure 3.8: Structural geological map of the south-central Pyrenees, with its focus on Tremp-Graus Basin. Figure from Lopez-Blanco et. al., 2003.

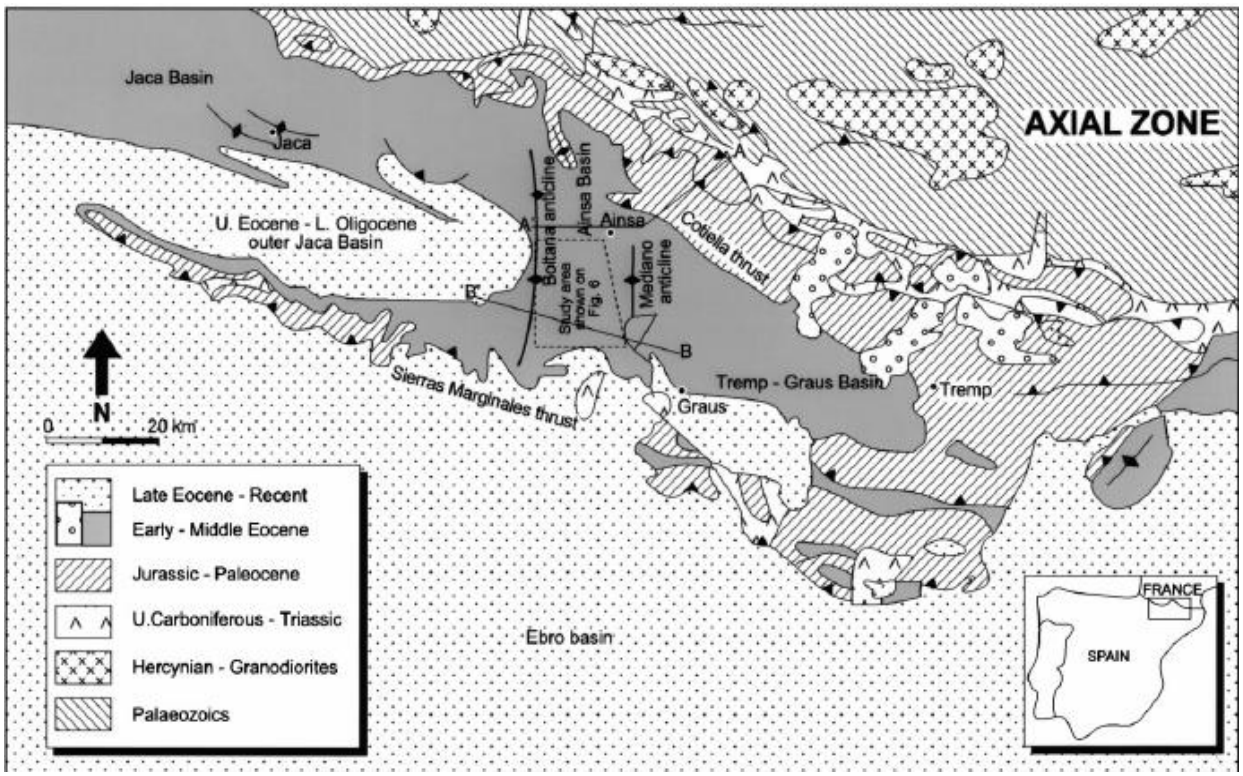

Figure 3.9: Position of the Ainsa Basin located between the Mediano anticline in the east and the Boltaña anticline in the west (Dreier et. al., 1999).

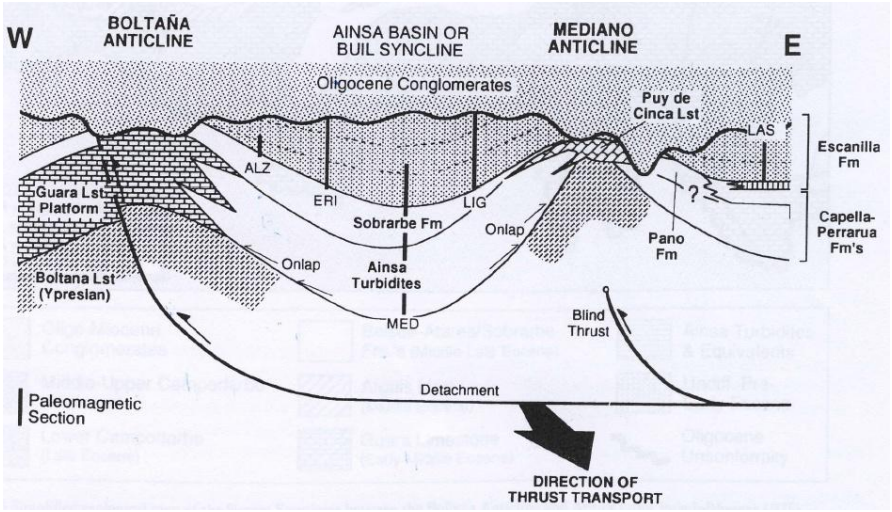

Figure 3.10: Cross-section of Ainsa Basin between Boltana Anticline and Mediano Anticline. The figure is from Bentham (1992).

The Ainsa Basin started developing in the transition between Ypresian and Lutetian due to flexural subsidence of the area laterally adjacent to the active south Pyrenean central thrust sheet. It was on top of this thrust sheet continental and deltaic deposits accumulated (Friend and Ori 1984). The boundary between the Ainsa Basin and the Tremp-Grauss Basin is defined by the change from an eastward compartment where the sole thrust displaces the south-Central Pyrenean to the south, to a western compartment, represented by the Ainsa Basin, where deformation is taken up by a set of imbricated thrusts with top-to southwest (Teixell, 1996; Travè et. al., 1998; Nijman, 1998). Mediano anticline, which is the most prominent structure in this transition zone, is a detachment fold which developed in the transitional foredeep phase of the Ainsa Basin (Bentham et.al., 1992; Poblèt et. al., 1998; Arbues et.al, 1999). When the detachment fault beneath Ainsa Basin propagated further westward in middle Lutetian and Bartonian times, it broke towards the surface in several places, with the result of development of several fault-propagation folds, of which the Boltana anticline is the most prominent (Atkinson et. al. 1987). Together with Boltaña anticline, Mediano anticline and Buil syncline are the most prominent structures in the Ainsa Basin (figure 3.12).

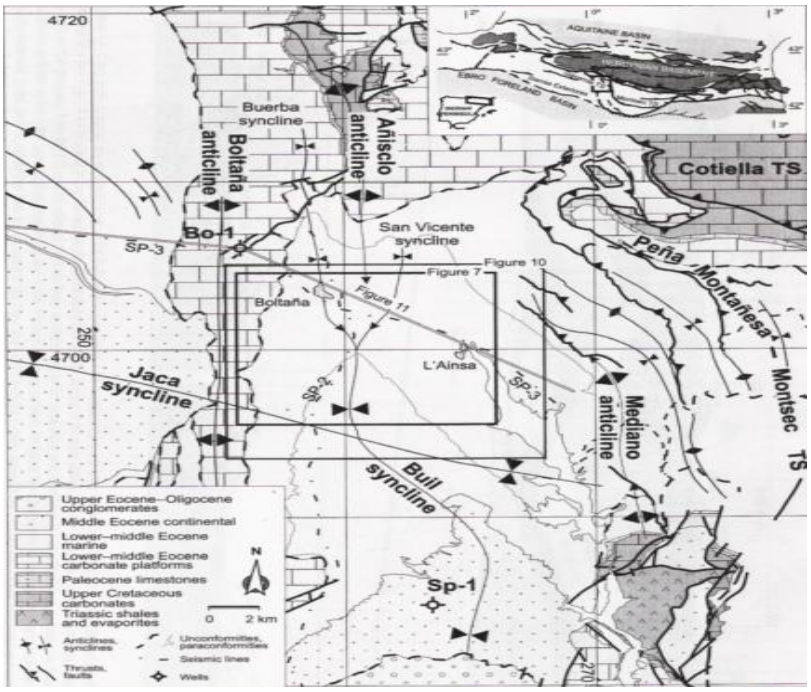

Figure 3.12: Map sheet of the structural features in Ainsa Basin. Boltana anticline and Mediano Anticline represent the western and eastern boundary of the Ainsa Basin respectively. From Fernandez et. al., 2004.

The northeastern part of the basin is influenced by the Cotiella Nappe system, represented by Cotiella, Atiart and Los Molinos thrusts, with top to southwest (Atkinson et. al., 1987; de Boer & Peper, 1995; Poblèt et. al., 1998; Travè et.al., 1998). These represent a southwestward prograding thrust imbricate fan system of early Eocene age, with several back-thrusts with top-to northeast. In the same period, a left-stepping thrust system developed, related to the La Foradada fault, which is interpreted as a tear fault related to the Cotiella Nappe thrust system (Nijman, 1989).

3.4- Stratigraphy of the southern Pyrenees

The post-Hercynian Carboniferous rocks are strictly non-marine and largely fluvial (Puigdefabregas & Souquet, 1986). Volcanic rocks were deposited in Early Permian, before grey and red calcareous sandstones, siltstones and mudstones were deposited in Late Permian. The Middle and Upper Triassic consists of micritic limestone, dolomite, marl, cargneule and ophite. The uppermost part of the Triassic rocks are non-systematically oriented blocks of ophite set in a matrix of brecciated evaporate mylonite. This zone is the floor thrust of the Montsec thrust sheet (Williams, 1985). The post-Triassic rocks in the Montsec thrust sheet consists of calcareous sandstones, siltstones and mudstones (figure 3.13).

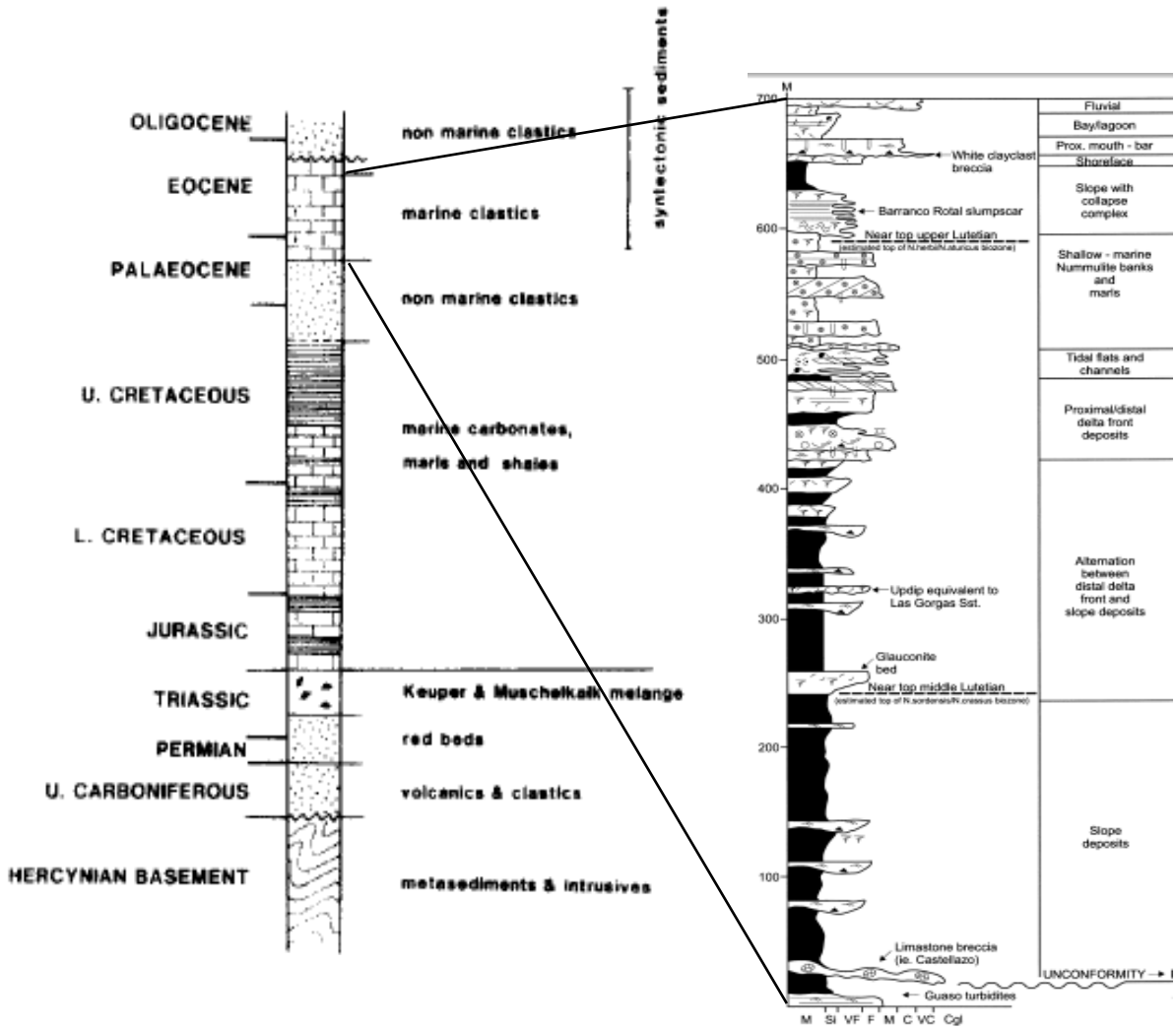

Figure 3.13: Sedimentological log from the south central Pyrenees to the left (from Williams, 1985). The log to the right illustrate the Sorbrarbe delta in Ainsa Basin, accumulated in Lutetian time (from Arbues et.al., 1999).

In the transition between Mesozoic to Tertiary in the Pyrenees, a widespread global transgression, together with the establishment of plate convergence conditions, led to the change from a deep basin to development of foreland basins (Puigdefabregas & Souquet, 1986). These foreland basins developed due to responses by thrust wedge loading and the subduction-related flexure of the down-going Iberian plate. The development of this thrust system took place synchronously with the accumulation of sediments into the related foreland basins, which implies that basin geometry and sedimentation patterns are controlled by the development of the thrust system (Muñoz, 1992).

The Early Eocene is characterized by fluvial and shallow marine deposits, which has been deposited in a northwest draining axial trunk system that again was fed by alluvial fans along the northern margin (de Boer & Peper, 1995). These deposits are mainly from the Montanana delta, which developed in Early Eocene time (figure 3.14). The continental deposits from Late Eocene – Oligocene time is mainly from the Cornudella formation, which is derived from uplift of the axial zone resulting in infill of the paleovalleys (Vincent, 2001).

From Early – Middle Eocene, clastic supply has been sufficient reduced to allow large-scale colonization of Nummolites in the shallow marine part of the Ainsa Basin (Selzer, 1933; Williams, 1985; Puigdefabregas & Souquet, 1986). The Nummolite packstone is interpreted as shoals and banks formed by a combination of in-situ growth of Nummolites-colonies and episodes of transport and re-deposition. The mudstone are thought to have been formed in protected areas between higher-relief features, with the Nummolites living scattered upon a mud substrate in fairly quite-water conditions (Arbues, 1999).

The deep-water systems in the Ainsa Basin accumulated between two structural highs in Early-Middle Eocene, today seen as Mediano and Boltaña anticlines (Corregidor & Pickering, 2005; Flåt, In Prep.). The deep-water system is mud-dominated, but it also includes several clastic turbidite systems (figure 3.14 & 3.15) (Bakke, 2007).

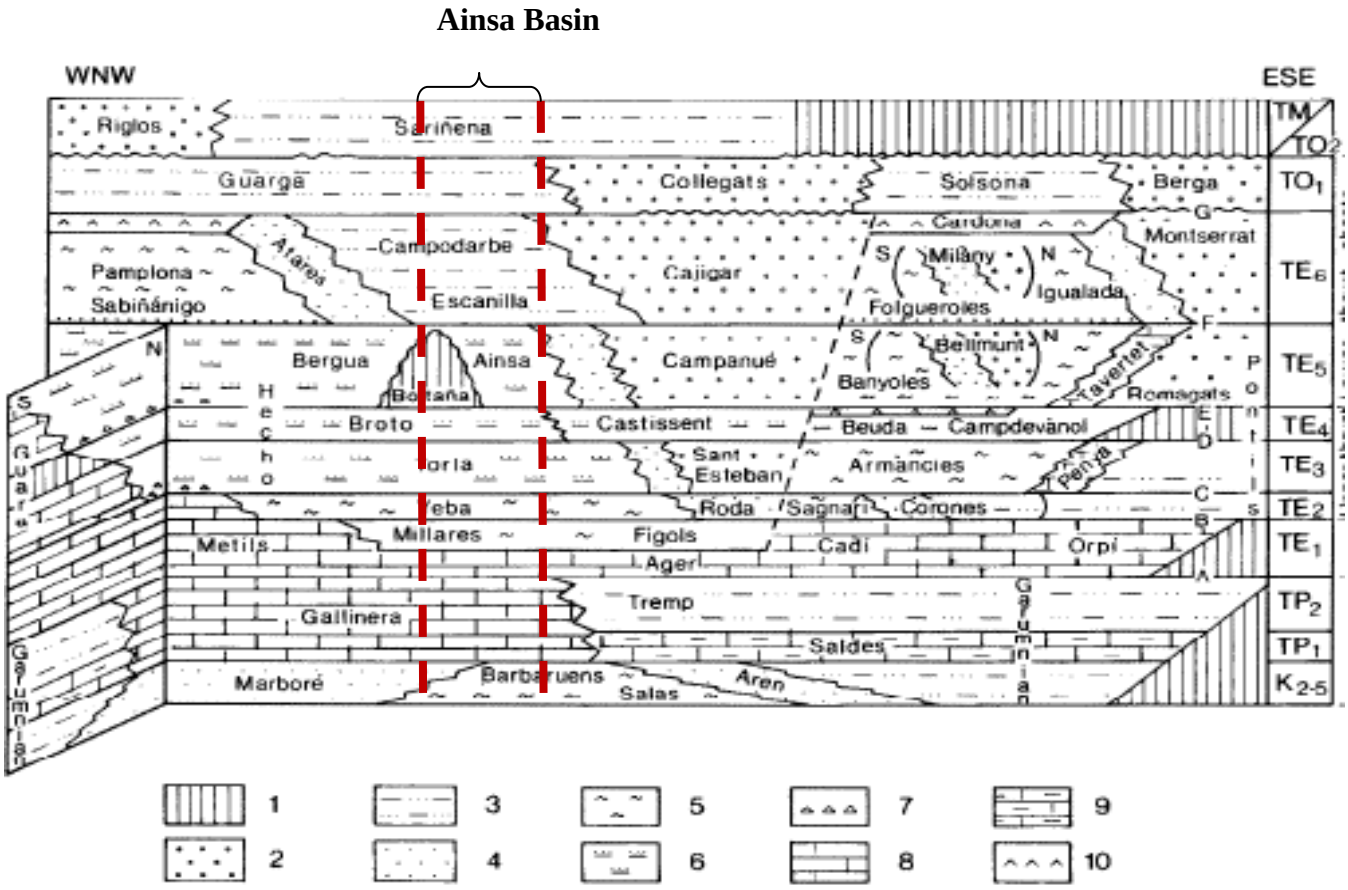

Figure 3.14: An illustration of Tertiary lithostratigraphic units, thrusting events and depositional sequences in the southern Pyrenees. 1=Hiatus, 2=conglomerates, 3=Fluvial deposits, 4=nearshore sandstone, 5=blue marls, 6=turbidites, 7=slope breccias and megaturbidites, 8=shallow marine carbonates, 9=non-marine carbonates, 10=evaporates.TE_1 – TE_4 are of Early Eocene age. TE_5 and TE_6 are Middle and Late Eocene, respectively. Figure from Puigdefàbregas & Souquet, 1986.

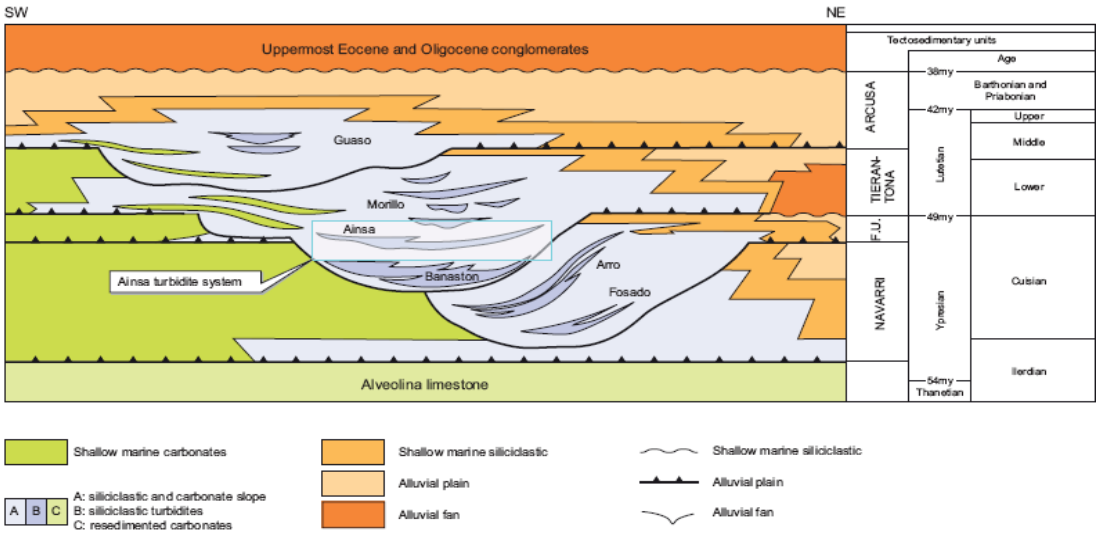

Figure 3.15: Stratigraphic cross-section of the Ainsa Basin deposits. From Bakke, 2007.

Chapter 4 – Locality descriptions and interpretations

Ainsa Basin (figure 4.1) offers good conditions for the study of the interaction between syn sedimentary structuring and the regional development of the frontal mountain chain. The main focus has been on the north – eastern part of the Ainsa basin. No publicized studies on the structural geology of the area are available. The main structures delineating the northeastern Ainsa Basin are the Mediano anticline and Buil syncline (see figure 3.12), together with several minor folds and faults represented by the Cotiella Nappe system (figure 4.1). Three of these folds were investigated in more detail during field work, and described in chapter 5. Syn-sedimentary faults are present in several areas, of which two locations were investigated in detail (section 5.2).

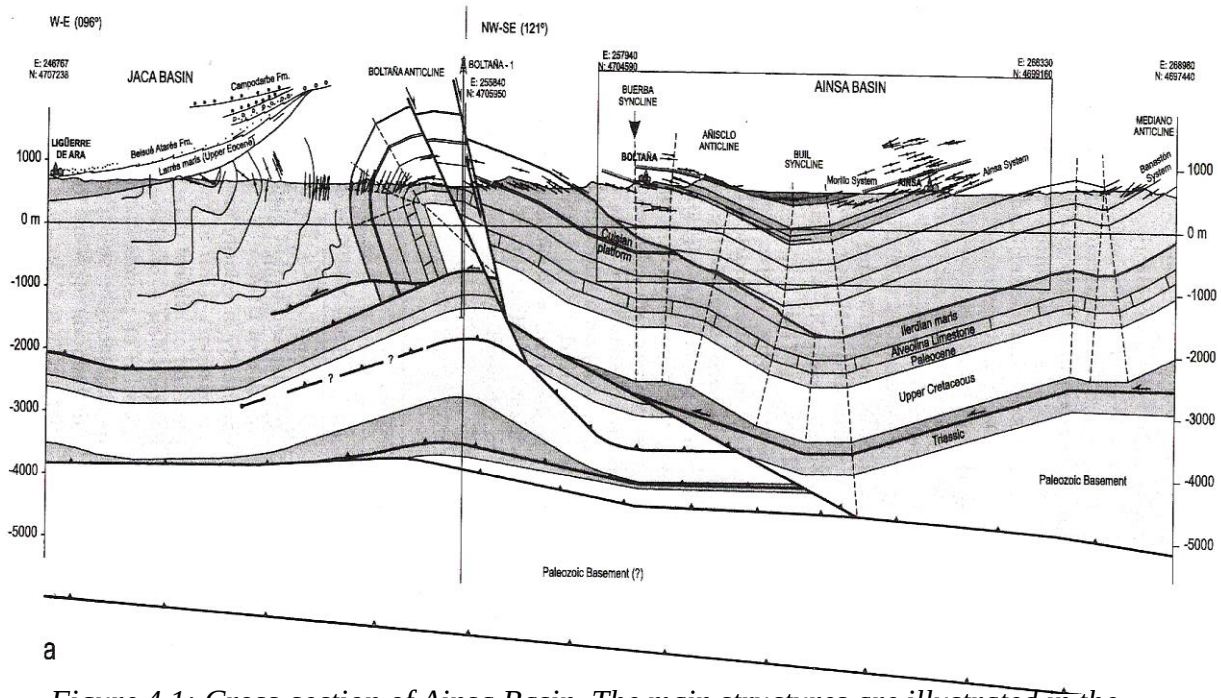

Figure 4.1: Cross-section of Ainsa Basin. The main structures are illustrated in the cross-section, i.e. Boltaña Anticline and Mediano Anticline representing eastern and western boundary respectively, and Buil Syncline were Ainsa Basin is located. From Arbuès, 2004.

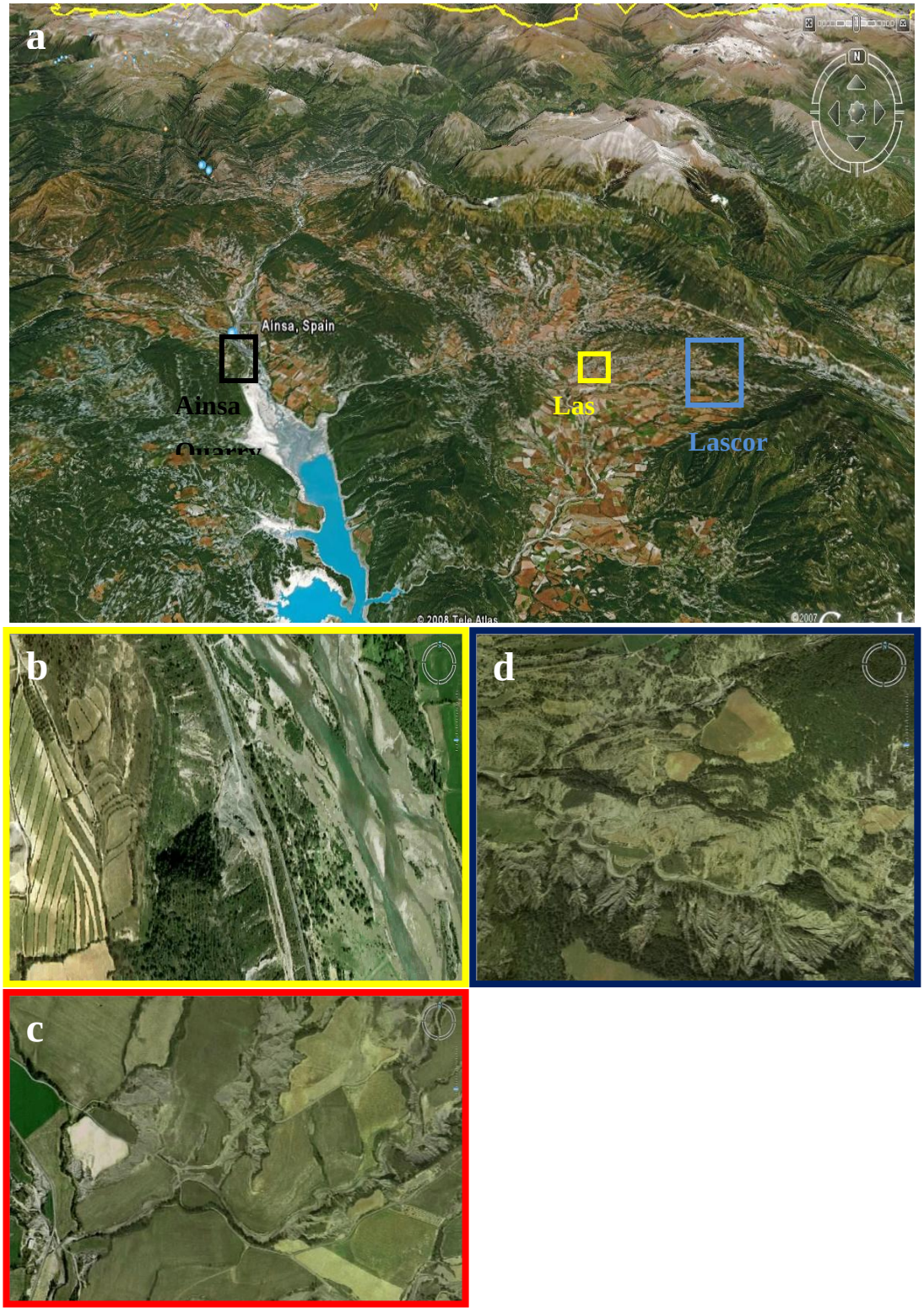

Figure 4.2: a) Overview of northeastern Ainsa Basin and northwestern Tremp-Graus Basin (from googleEarth, 2008). b) Detail photo of Ainsa Quarry (from Aragon 3D, 2007). c) Detailed photo of Las Uslas (from Aragon 3D, 2007). d) Detailed photo of Lascorz (from Aragon 3D, 2007).

The study area comprises three main localities (figure 4.2). This chapter follows a scheme where the localities are presented in a sequence so that those characterized by the less deformed are presented first. This is done with the intention to identify structural elements that are not related to the regional folding, so that the relation between such syn-sedimentary or buried-related structures can be identified in the folded area. At the different localities, fracture populations are identified and described using the criterion of Stearns (1968). Populations of fractures are defined in a sequence from Q1–Q5 in Ainsa Quarry, and L1-L9 in Lascorz.

Fractures which have developed prior to folding where re-oriented according to the regional tectonic gradient. This was done, particularly in the Lascorz area, to find the orientations of the fractures at the time of development. The method described by Ramsay (1961) was used to find this gradient.

4.1 – Ainsa Quarry

The Ainsa Quarry is the locality in the present study which is the least influenced by folding – only a slight tectonic tilt of approximately 20^{o} to the east is recorded. The locality is represented by a 15 meter high and 600 meter long exposure, one kilometer south of Ainsa town (figure 4.3). The UTM-coordinates are 31265340E, 4698819N.

The section contains structures developed in the recent years due to exploding through human activity in the quarry. Due to this activity, sliding on millimeter scale of rock occur after heavy rainfall, which makes safety equipment (e.g. helm) necessary during field work due to rock fall.

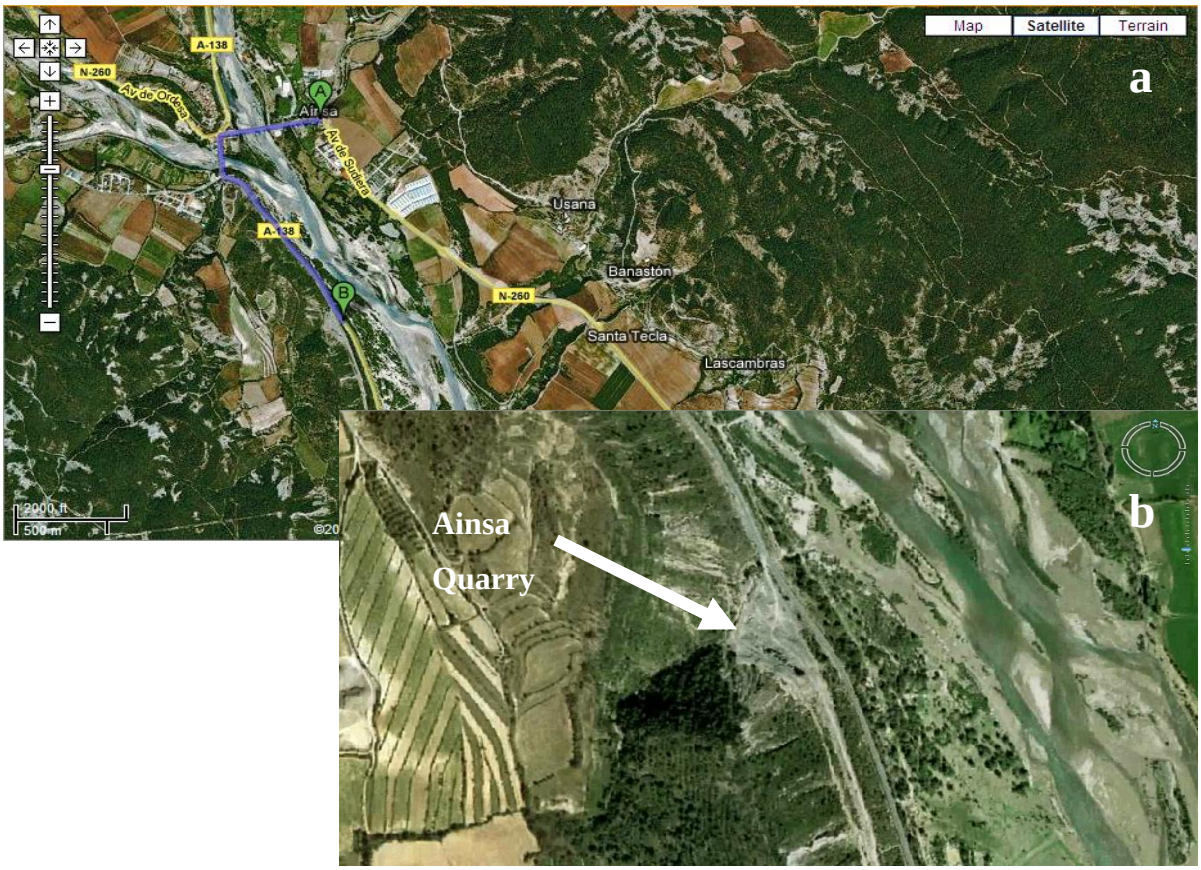

Figure 4.3: Road map from Ainsa town (A) to Ainsa Quarry (B) (From GoogleMaps™ , 2007). b) Detailed photo of Ainsa Quarry (from Aragon 3D, 2007).

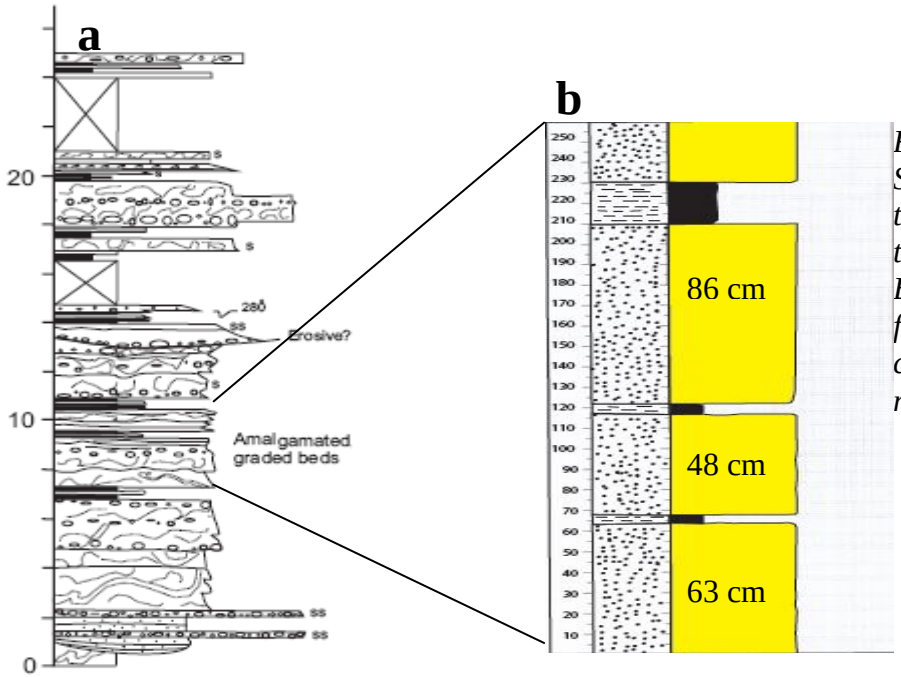

Figure 4.4: a) Sedimentary log of the Ainsa II turbidites (from Bakke, 2007). b) Log from Ainsa quarry containing the beds measured.

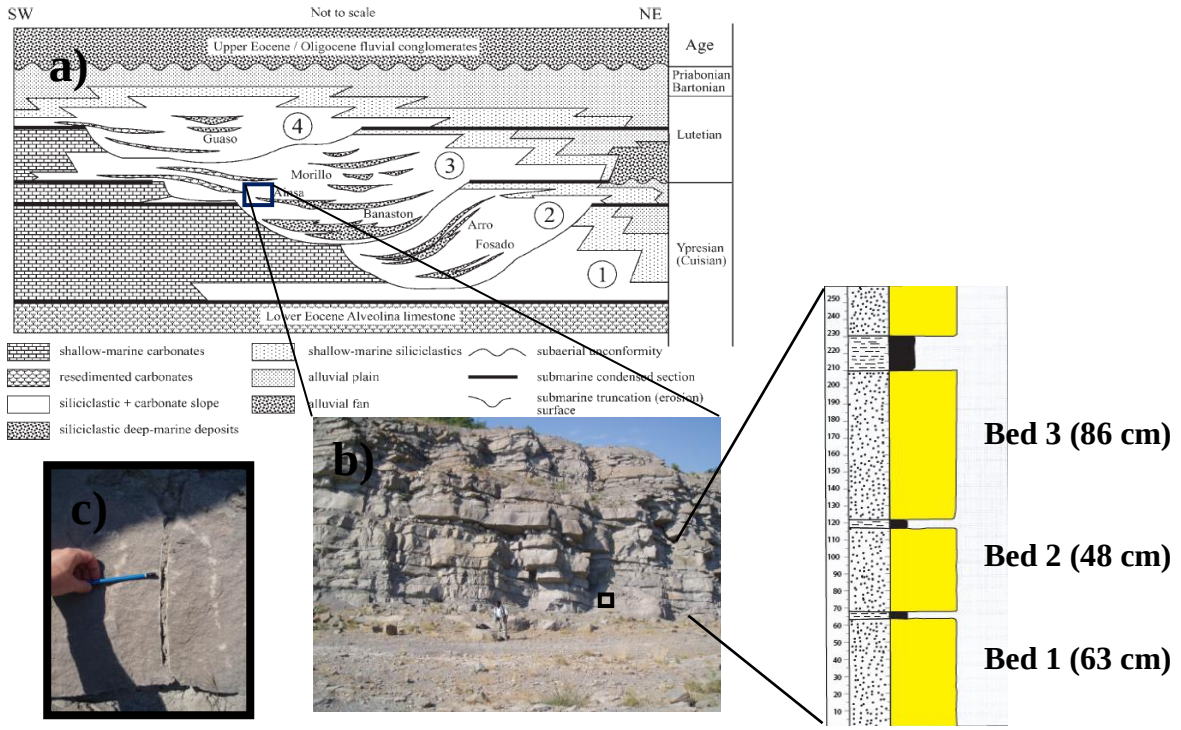

Figure 4.5: a) Stratigraphic overview of the Ainsa Basin, were the Ainsa Quarry is marked with the square. From Bakke et. al., 2007. b) Section making up the locality with corresponding log. c) Picture of a typical fracture represented in the Quarry, also marked in b.

The rock types in Ainsa Quarry are silisiclastic sandstone and shale, together with minor beds made up by conglomerates (figure 4.4). The sediments were deposited in deep marine turbidite complex distributaries' channels, and represents turbidites deposited in Middle Lutetian time (Puigdefàbregas & Souquet, 1986; Bakke et. al., 2007). The turbidite sand bodies contain sediments that originate from fluvial and shallow marine systems, which migrated into the basin from the southeast, and are a part of the Ainsa II turbidites (figure 4.5).

At the time of deposition, the southern Pyrenean foreland basins developed further into piggy-back basins, were Ainsa Basin is one of them (see chapter 2). Structurally, Ainsa Quarry is located in an area with minor macro scale deformation, on the western limb of Buil syncline, approximately seven kilometers west and 10 kilometers east of Mediano and Boltana anticlines, respectively. The depositional environment was probably in the central parts of the Ainsa piggy-back basin, and the average orientation of the strata is N179E and dipping 22^{o} westwards.

Strike and dip, maximum width, depth, geometry, architecture, mode and presence of calcite cement where measured of 71 fractures altogether, whereas length, parallel with bedding (S_0) were not possible not measure due to limited exposure. Based on these observations, five populations are recognized (i.e. Q1-Q5), mainly based on mode, orientation, geometry and fracture fill (figure 4.6). The fracture frequencies in the three beds reflects the thickness of the beds, where the thinnest bed (i.e. bed number two) has highest fracture frequency, whereas the thickest (i.e. bed number three) has lowest fracture frequency (figure 4.7).

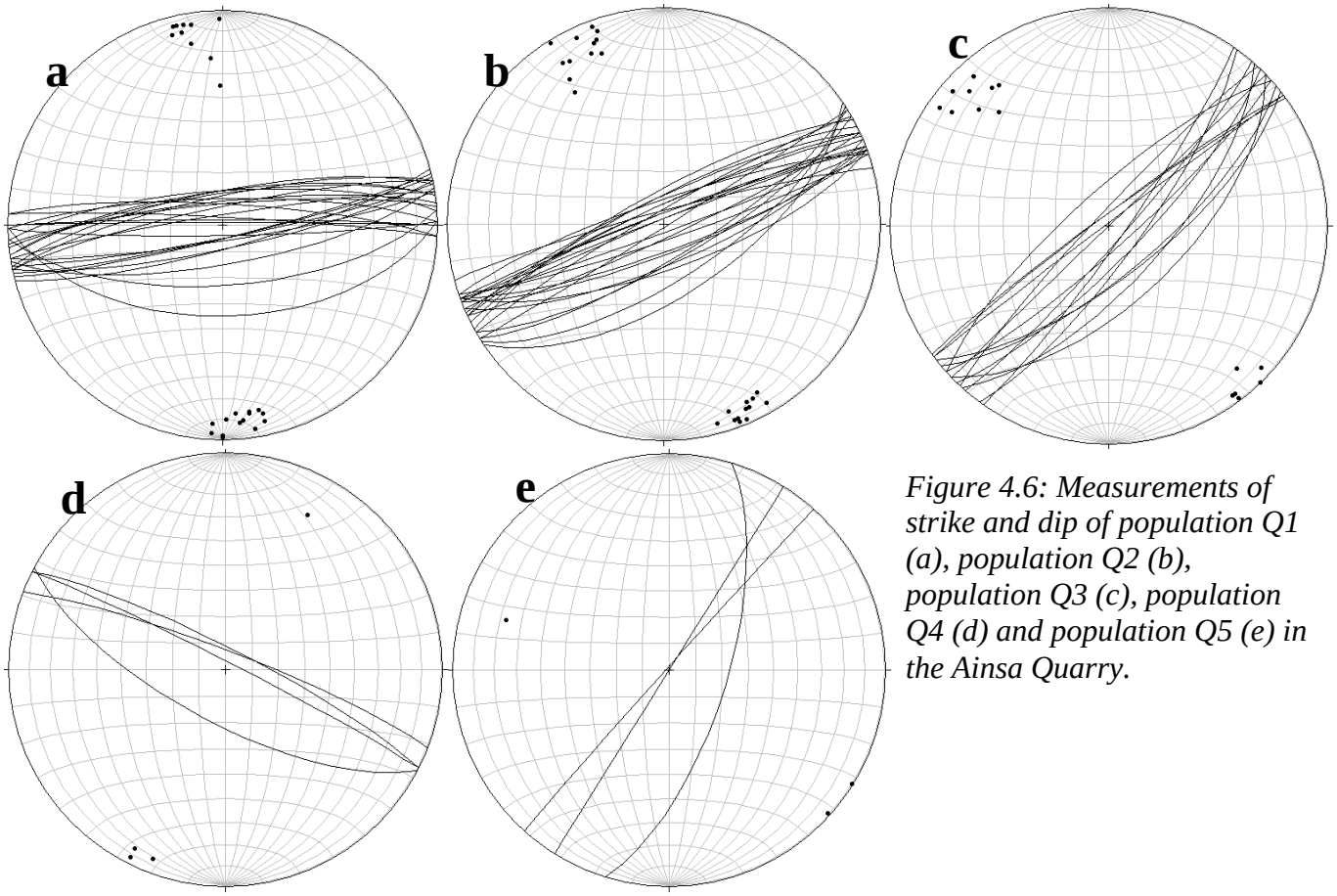

Figure 4.6: Measurements of strike and dip of population Q1 (a), population Q2 (b), population Q3 (c), population Q4 (d) and population Q5 (e) in the Ainsa Quarry.

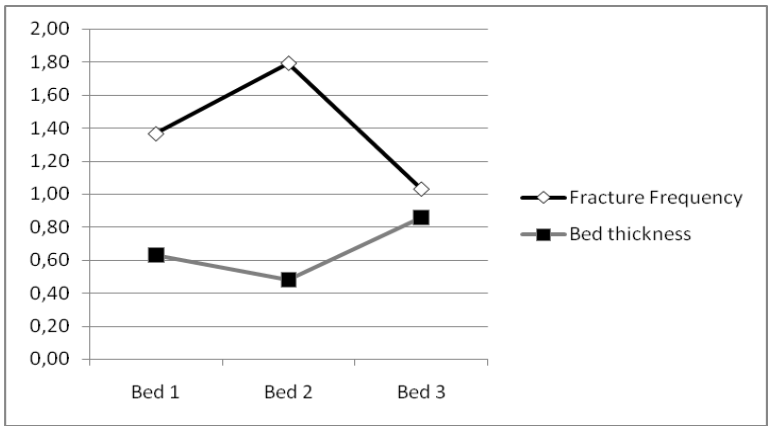

Figure 4.7: Fracture frequency in the three beds where measurements were pursued.

Population Q1

There are 24 population Q1 fractures documented from the Ainsa Quarry, with an average orientation towards N085E – N265E and with vertical dips (figure 4.8a). The fractures are tensile and the individual fractures are represented by one single plane, where 17 are straight and the last seven are wiggly. The individual fractures are limited to one single bed (i.e. single-bed fractures) although the overall population is evenly distributed in the three beds, with all architectural styles, described in chapter 1, represented (table 4.1). All fractures are calcite cemented, with antitaxial, fibrous growth. The average depth of the fractures is 15 centimeters, and all fractures are closed, with an average width of three millimeters. The fractures are systematical distributed in the three beds, with similar distance between individual fractures.

Interpretation population Q1

Due to their systematic distribution within the individual beds and that each fractures are restricted to one layer, these layers are thought to have developed during burial. Their mode (mode I) and architecture also reveals that the maximum stress axis was vertical at the time of development, which is typical for fractures related to mechanical compaction.

Bed number / Shape	Bed 1	Bed 2	Bed 3
	3	4	1
	7	5	2
	1		
		1	
			
	0	0	
	5	1	1
	6	9	2

Table 4.1: Amount of population Q1fractures with the different geometries in the various beds.

Population Q2

There are 25 population Q2 fractures documented from the Ainsa Quarry, with an average orientation of N066E – N246E and vertical dip (figure 4.8b). All fractures are tensile and the individual fractures are represented by one single plane, where 20 fractures are straight and the last five are wiggly. These are, as population Q1, evenly distributed in the three beds, with all geometries, described in chapter 1, represented (table 4.2). All fractures are calcite cemented, with antitaxial, fibrous growth. All fractures are closed, with an average width of 2 millimeters and an average depth of eight centimeters.

Interpretation population Q2

These fractures are thought to have developed during mechanical compaction, due to their systematic distribution within the individual beds and that the individual fractures are restricted to one layer. Their mode (mode I) and architecture also reveals that the maximum stress axis was vertical at the time of development. These characteristics are typical for fractures developed during burial.

Bed number / Shape	Bed 1	Bed 2	Bed 3
		1	2
	6	5	2
			3
		1	5
			
			
	1	1	3
	5	6	9

Table 4.2: Amount of population Q2 fractures with the different geometries in the various beds.

Population Q3

There are 15 population Q3 fractures documented from the Ainsa Quarry, with an average orientation of N049E – N229E and dips vertical (figure 4.8c). All fractures are tensile, where 13 of the fractures are represented by one single plane and the last two have an en echelon pattern. Nine fractures are straight and the last six are wiggly. These are mostly observed in bed one, with all geometries, described in chapter 1, represented (table 4.3). All fractures are calcite cemented, with antitaxial, fibrous growth. The average depth of the fractures is 13 centimeters. All fractures are closed, with an average width of 2, 5 millimeters.

Interpretation population Q3

These fractures are, as populations Q1 and Q2, thought to have developed during mechanical compaction, for the same reasons as population Q1 and Q2. The fractures are systematically distribution within the individual beds and the individual fractures are restricted to one layer. Their mode (mode I) and architecture reveals that the maximum stress axis was vertical at the time of development.

Shape \ Bed number	Bed 1	Bed 2	Bed 3
			
	8	3	2
			
			
	1	1	
			
	3	2	1
	6	2	1

Table 4.3: Amount of population Q3 fractures with the different geometries in the various beds.

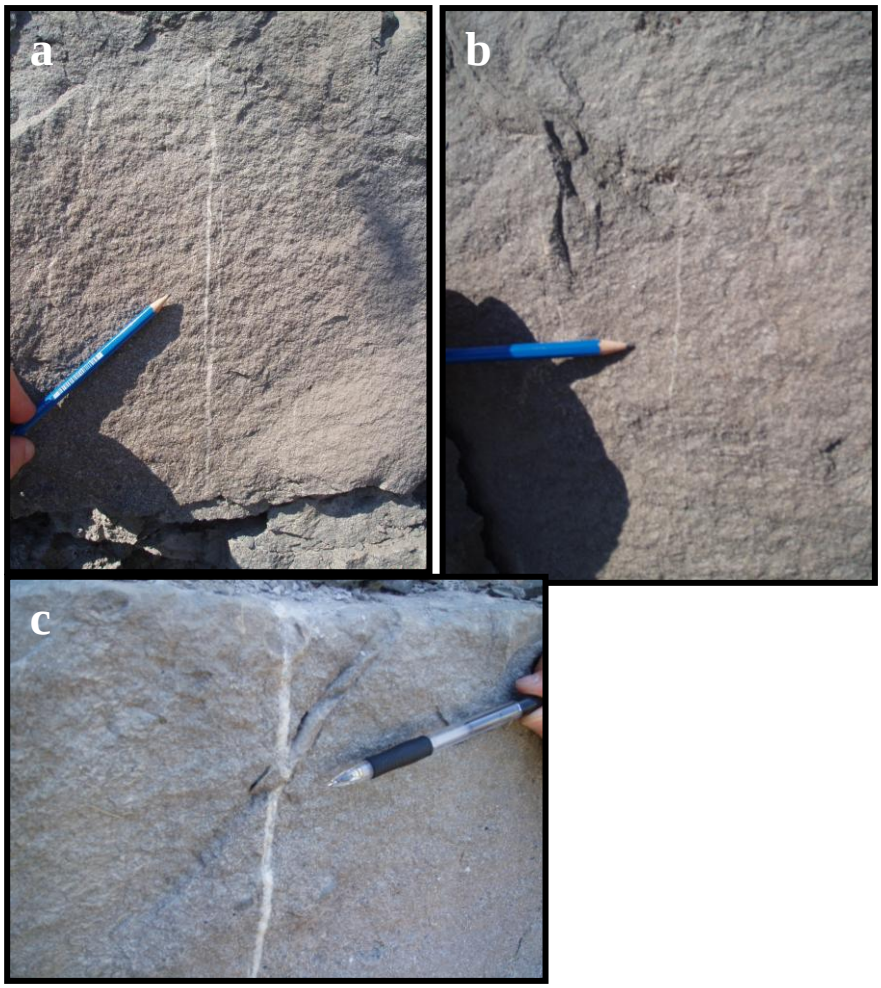

Figure 4.8: a) Population Q1 fracture. b) Population Q2 fracture. c) Population Q3 fracture. Pencil as scale.

Population Q4

There are four population Q4 fractures documented from the Ainsa Quarry, with an average orientation of N115E – N295E and dips vertical (figure 4.9). All fractures are tensile, represented by one single plane and penetrating minimum one layer boundary (i.e. multi-layer fractures). Two fractures are straight, whereas the last two are wiggly. None of the fractures are calcite cemented, and their average depth, perpendicular to bedding (S_0) is 87 centimeters. All fractures are open, with an average width of 4, 25 millimeters.

Interpretation population Q4

The mode and architectures of the fractures indicate that these developed during burial, and are thereby related to mechanical compaction. Since no calcite cement was observed in the fractures, together with the crossing of layer boundaries, these fracture have most likely developed at a different time relative to populations Q1, Q2 and Q3.

Figure 4.9: Example of population Q4 fracture. Pencil as scale

Population Q5

There are three population Q5 fractures documented from the Ainsa Quarry, where all three fractures have a strike-slip component. Their average orientation is N037E - N217E and dips vertical. These are all observed in bed two, containing calcite cement with growth lineations indicating dextral displacement (figure 4.10; growth lineation described in section 1.4). Individual fractures are represented by one single plane, penetrating the whole bed they are observed in. All fractures are straight.

Interpretation population Q5

Due to the growth lineation, showing dextral displacement, these fractures must be strike slip fractures. These fractures are therefore thought to have developed during tectonic contraction.

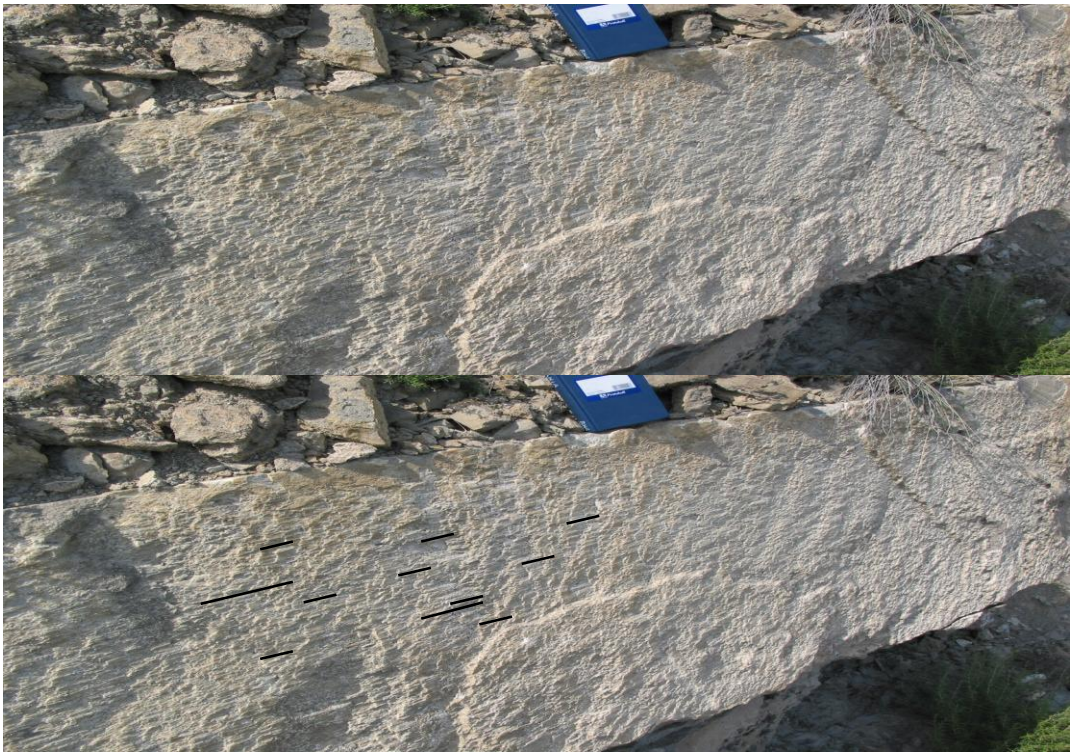

Figure 4.10: Lineation observed along population Q5 fractures at Ainsa Quarry (a), marked with black lines in b. Picture by Roy H. Gabrielsen.

4.2 – Las Uslas

Las Uslas is located approximately 1, 5 kilometers east of Mediano anticline, 15 minutes eastwards from Ainsa Town by car (figure 4.11). The UTM is 46961518N 31269444E, and the locality is represented by a 15 meter broad and five meter high section. A ladder was needed to get access to the uppermost beds in the section. The average orientation of the bedding is N116E, with an averaged dip of 16^{o} towards southwest.

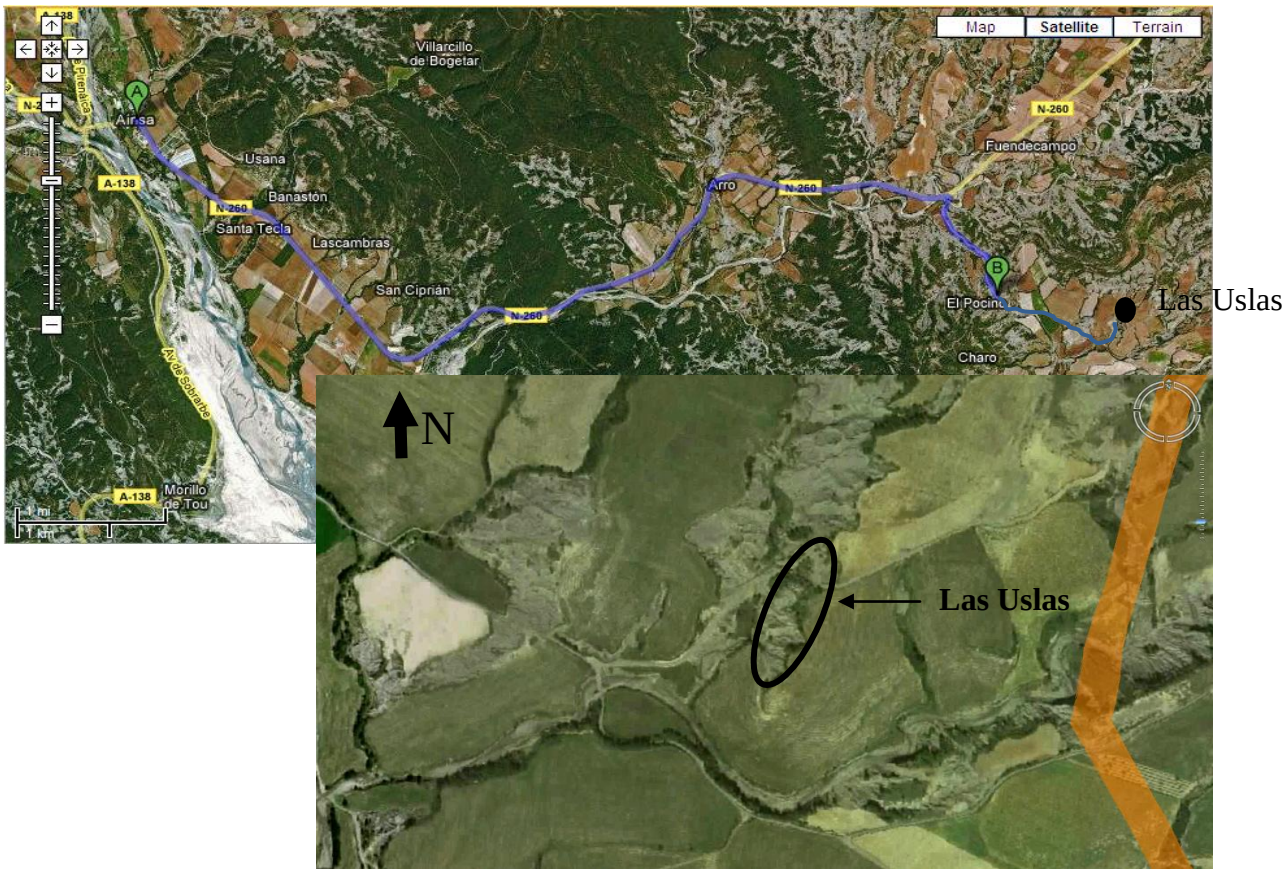

Figure 4.11: a) Road desription from Ainsa town to Las Ulsal (from googleMaps™ , 2007). b) Detailed photo of Las Uslas (from Aragon 3D, 2007).

The age of the sediments at Las Uslas are Paleocene and early Eocene (Puigdefàbregas & Souquet, 1986) (figure 4.12). The sedimentary sequence is dominated by calcareous sandstones interbedded with mudstones. The mudstones represent quiet depositional conditions while the calcareous sandstones are deposited in a depositional environment characterized by higher energy in the water masses, which developed during progradation of the coastline (Williams, 1985). Structurally, Las Uslas is situated in the south central foreland basin, which developed in Paleocene and early Eocene (see chapter 3), on the eastern limb of Mediano anticline.

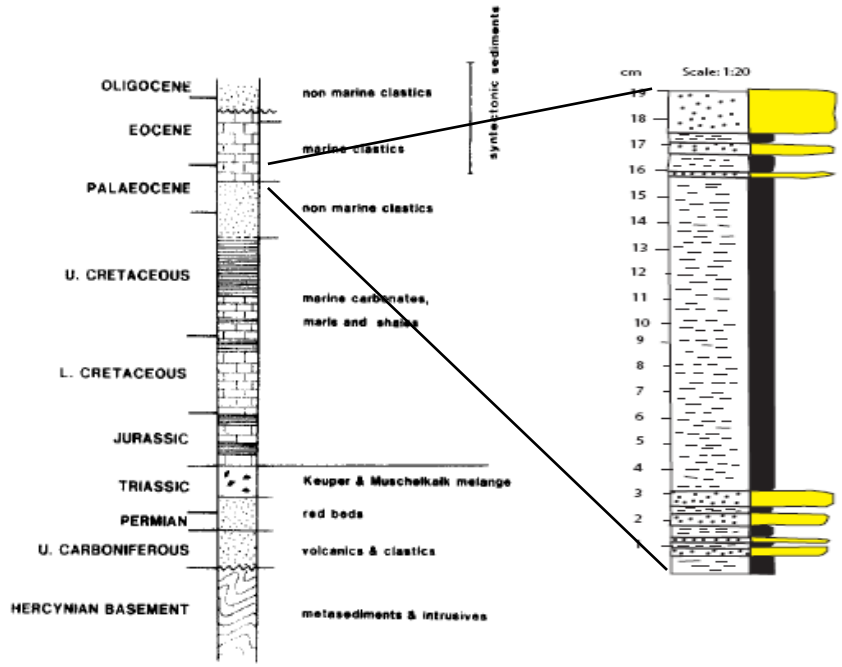

Figure 4.12: Sedimentological log from Las Uslas showing stratigraphical position of the area. The deposits are calcareous sandstone (yellow) and mudstone (black). The log to the left is from Williams (1985), while the log to the right is made in Las Uslas during field work described in section 1.2.

Las Uslas is characterized by a system of parallel faults (figure 4.13). The faults display normal displacement and listric geometry. The uppermost beds in each fault block consist of calcareous sandstone, whereas mudstones dominate the lower parts. Orientation of the faults, together with offset along them, can be measured directly. The normal displacement across each fault is rather constant, approximately 1, 5 meter.

Six faults are exposed in the 15 meter broad section at Las Uslas. The thickness of the beds increases towards the fault plane. Furthermore, the corners of the sandstone at the boundary to mudstone are smoothed (figure 4.14). It is possible to measure orientation on only four of the six mentioned fault planes, since fault plane two and six (figure 4.15) are eroded and also inaccessible due to the steepness of the exposure. All faults are parallel and the beds of the fault blocks have similar geometries and dip relations (figure 4.16). Fault five is particularly well exposed, and several measurements of the orientation and dip were obtained. In contrast, faults one, three and four are covered by mud debris in such a degree that only one (fault four) and two (fault one and three) measurements were possible. Measurements representing each fault are done along one fault plane. Calcite cement is observed along five

of the fault planes. Offsets are determined along all six fault planes. The average orientation of the four measured fault planes is N321E with an average dip of 45^{o} towards northeast.

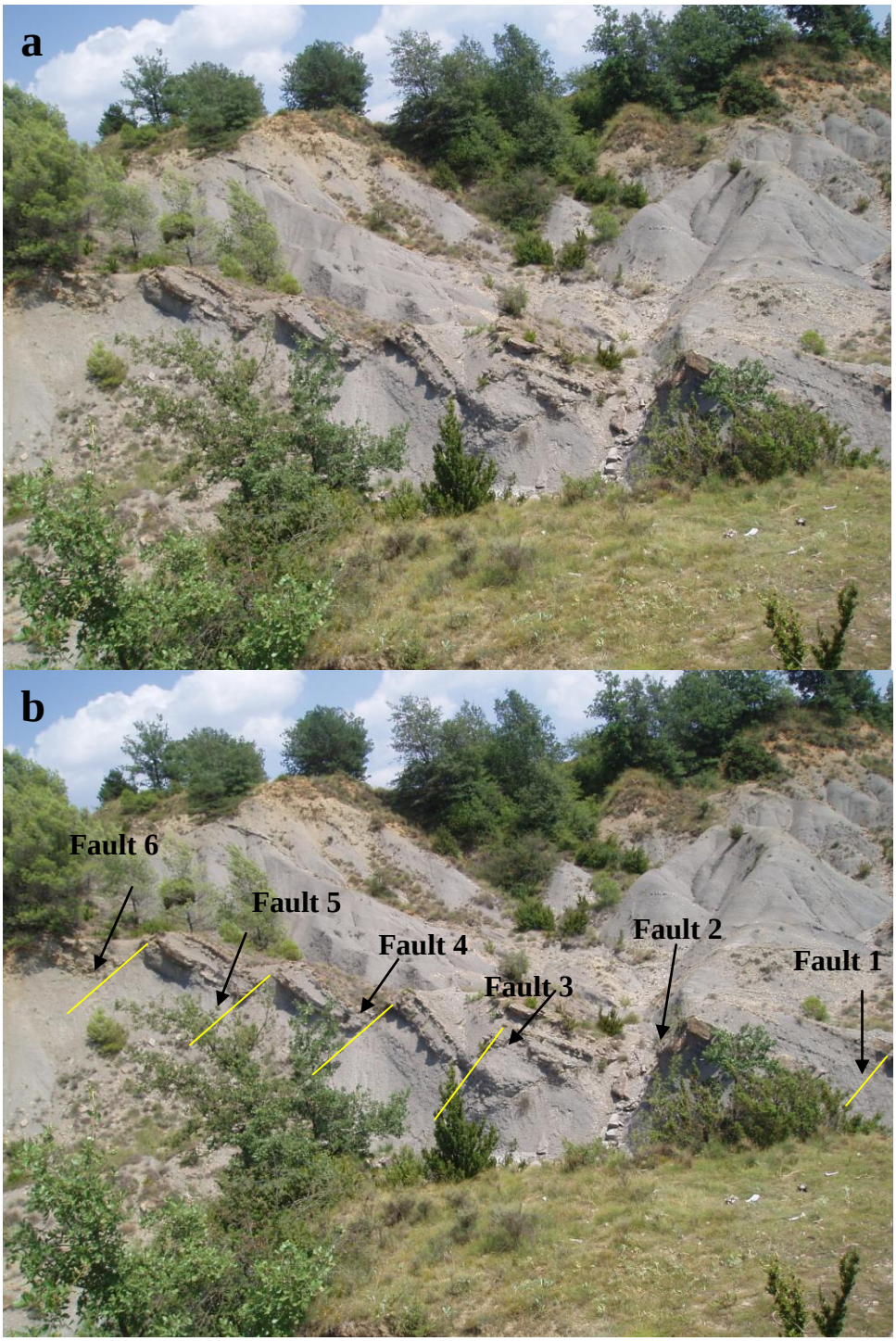

Figure 4.13:

a) The 15 meter broad section at Las Uslas.
b) The same picture as in a, including illustrations of the fault planes.

Figure 4.14: a) Picture showing rounding of corner in the sandstone. b) Picture showing Thickening of bed towards the fault.

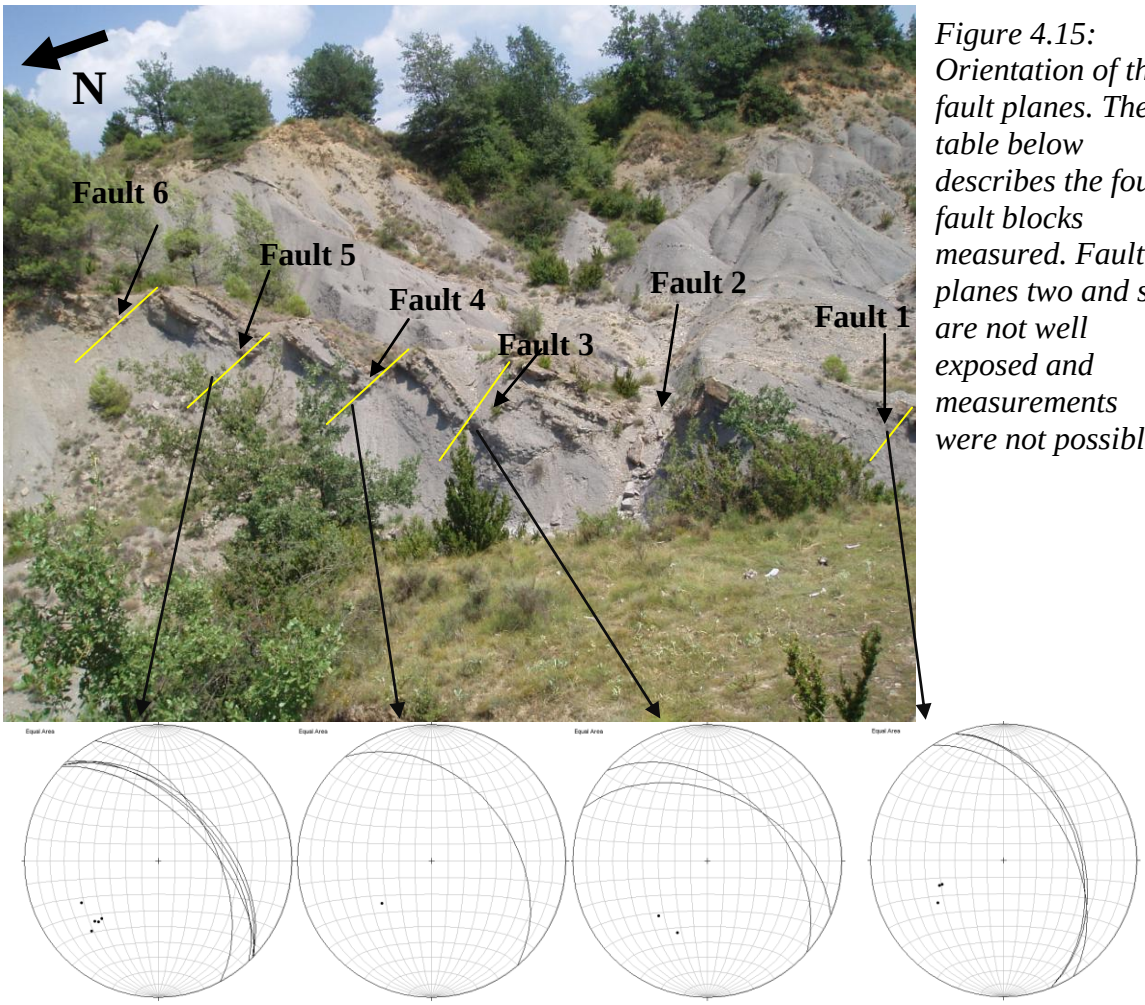

Figure 4.15: Orientation of the fault planes. The table below describes the four fault blocks measured. Fault planes two and six are not well exposed and measurements were not possible

Fault 5	**Fault 4**	**Fault 3**	**Fault 1**
Fault 5 is calcite cemented. The offset is 154 centimeters. Five measurements were done along the fault plane, with an average orientation of 315/53.	Fault 4 is calcite cemented. The offset is 160 centimeters, and the average orientation is 320/40.	Calcite cement is present in fault number 3, with lineation. The offset is 225 centimeters along this fault, and the average orientation is 312/45.	This fault is calcite cemented. The offset is 160 centimeters, and the average orientation is 339/42. Lineation is at the surface of calcite fracture fill, with an orientation of N052E and it plunges 42 degrees towards southeast.

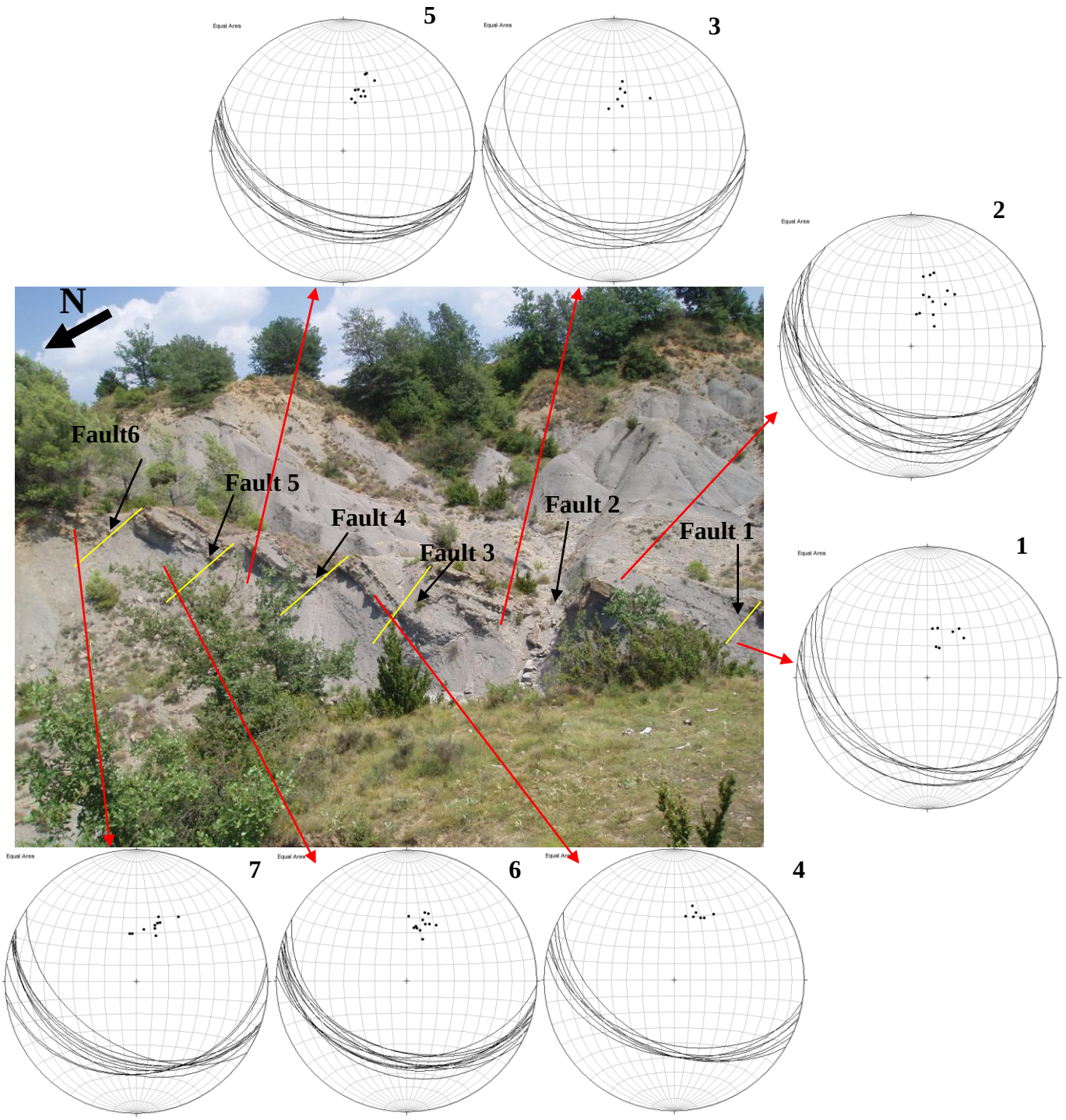

Figure 4.16: Las Uslas with corresponding measurements of strike and dip of beddings for each fault block. Measurements are taken in the calcareous sandstone beds.

Interpretation Las Uslas

As mentioned above, the beds within the fault blocks become gradually thicker towards the faults, and the corners, at the transition between mudstone and limestone at the faults, are rounded probably due to movement of mud after faulting. Both these characteristics are typical for syn-sedimentary faults (see section 1.4; Collinson, 1994; Bhattacharya & Davies, 2001; Bouroullec et.al., 2002). The third indication of syn-sedimentary faulting is that the beds immediately above the faulted sequence are un-faulted, and is not present at Las Uslas since these rocks are eroded. The bedding inside the seven fault blocks are very similar regarding the thickening relations. Also, the faults are parallel and have similar dips, which may be taken as an indication that they were activated by down-slope movements above one common floor fault. To find the true orientation of the faults at the time of development; these must be rotated according to the superimposed regional tectonic gradient. Due to the complexity in the regional deformation of which Las Uslas is a part of, the regional tectonic gradient were not possible to find from the data collected during field work. Nor are the gradient published in the literature. Therefore, the orientations of the faults described in this section are assumed to be the true orientations of which they had at the time of displacement.

4.3 - Lascorz

4.3.1 - Geological setting of Lascorz

Lascorz is an area located 15 kilometers east of Ainsa town (Figure 4.17 & 4.18) and 10 kilometer east of Mediano anticline. The area is easily accessed by car and most of the area is exposed, making field work easy to pursue.

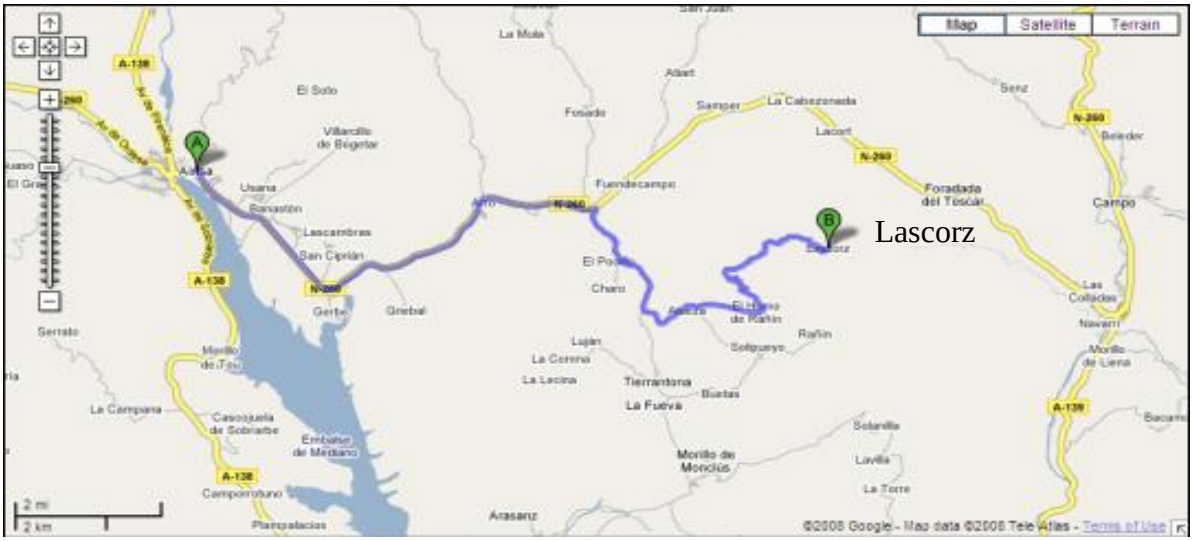

Figure 4.17: Roadmap Ainsa - Lascorz. The area is at the green bubble marked with the letter B. It takes approximately 30 minutes to drive there from Ainsa Town. From Google maps.

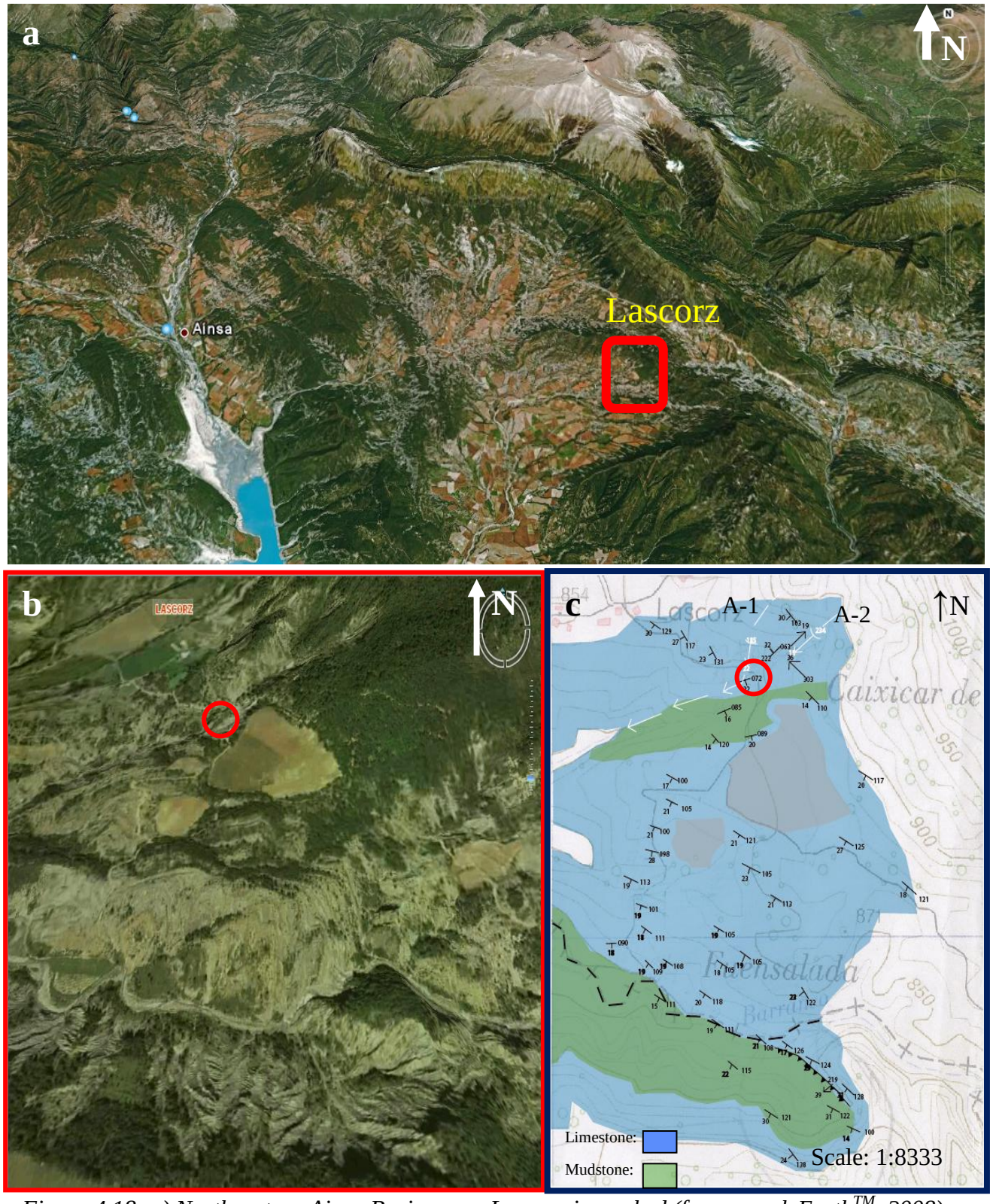

Figure 4.18: a) Northeastern Ainsa Basin, were Lascorz is marked (from googleEarth™, 2008). b) Close up aerial photo of Lascorz, which corresponds with the marked area in a (from Aragon 3D, 2007). c) Geological map of Lascorz. The area corresponds with b. Direct measurements were pursued at the red circle in b and c.

Lascorz is made up by sediments accumulated in Early Eocene (Nijman, 1998). The rock types are calcareous sandstone, where the matrix mainly consists of fossils and fossil fragments (described in chapter 3), interbedded with mudstone (figure 4.19). Since the carbonates mostly are made up by nummelites, which needed warm oxygen-rich conditions and much sunlight (Reading, 1996), the depositional environment must have been shallow marine at the time of accumulation of sandstone, with shorter transgressions and quite water conditions at the time of accumulation of mudstone. The sedimentary rocks at Lascorz represent a carbonate land-attached ramp, active in Early Eocene time (Puigdefabregas & Souquet, 1986; Woyessa, In Prep.).

Structurally, Lascorz area is situated one kilometer south of Peña Montanesa, within the thrust imbricate fan system related to the Cotiella Nappe system (Travè et. al., 1998), and approximately seven kilometers east of Mediano anticline. The Lascorz area is characterized by meso scale deformation, related to macro scale deformation, both represented by folds and fractures. The average orientation in the area is N119E, with an average dip of 23^{o} towards SSW.

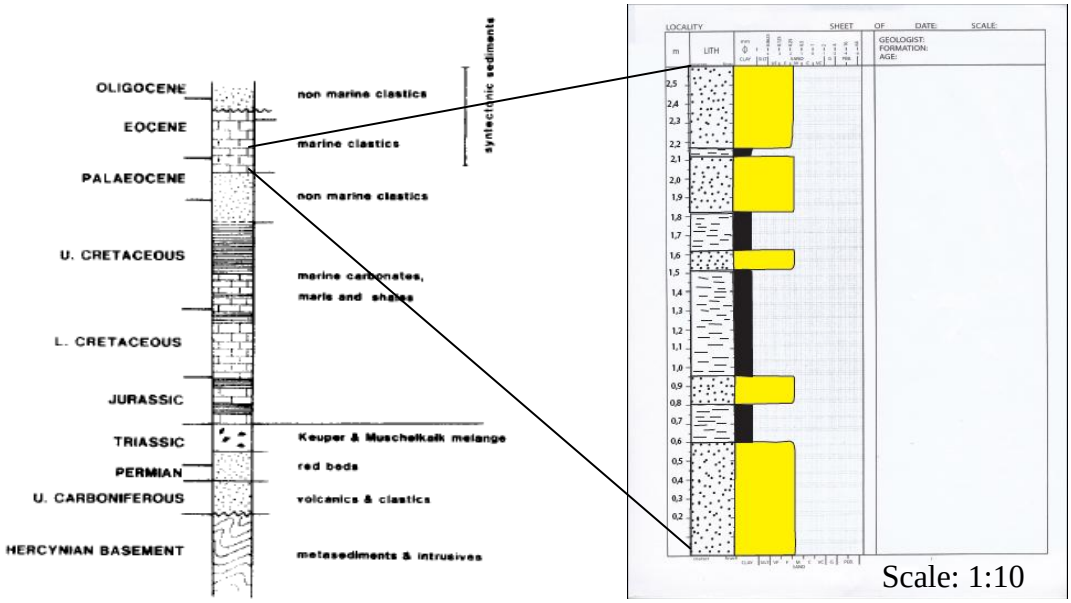

Figure 4.19: The stratigraphic position of the Paleocene Lascorz limestone and mudstone (Puigdefabregas & Souquet, 1986).The log to the right displays the stratigraphy in the Lascorz area, at Barranco river. The lithostratigraphic column to the left is from Williams (1985).

Three folds are influencing the local geology at Lascorz. The fold influencing most of the northwestern part of Lascorz, denoted A-1 in figure 4.18, is an anticline, of which strikes N185E and plunges 22^{o}, as derived from direct measurement at Caixicar de pardina (figure 4.20). The anticline A-1 is therefore striking parallel to the macro scale structures in the Ainsa Basin in general (i.e. Mediano and Boltana anticlines), in a NNE-SSW direction, and it is obliquely to the macro scale structures in the Pyrenees overall. A-1 is classified as an open fold, with amplitude of approximately 50 meters and a wavelength of approximately 300 meters. The fold axis is not straight, but shifts its orientation westwards along strike (i.e. southern part of the fold).

Figure 4.20: Fold axis of A-1 (a), were the beds are marked in b. Picture by Roy H. Gabrielsen.

Ten meters east of A-1, from where direct measurement of A-1 was pursued at Caixicar de pardina, another fold is located (denoted A-2 in figure 4.18). This fold has a wavelength of three meters and amplitude of two meters (figure 4.21). A-2 is gently open, and the orientation of its fold axis is N234E, with a plunge of 15^{o}.

Fold axes of A-1 and A-2 were also determined in stereoplots (β-plots) by construction from measurements of bedding (S_0) of each side of the fold axes (figure 4.22). By doing this, β-plots are documented close to the direct measurements, with A-1 striking N170E and plunging 19^{o}, and A-2 striking N235E and plunging 18^{o}.

Lineations were measured in calcite cement, located on the surface of calcareous sandstone beds at Caixicar de Pardina. They display two main directions, namely N59E and N315E (figure 4.23). The lineations are surface lineations which reflect the direction of movement (surface lineations described in section 1.4).

Figure 4.21: A-2, with yellow, dotted lines on the lower picture. Hammer as scale.

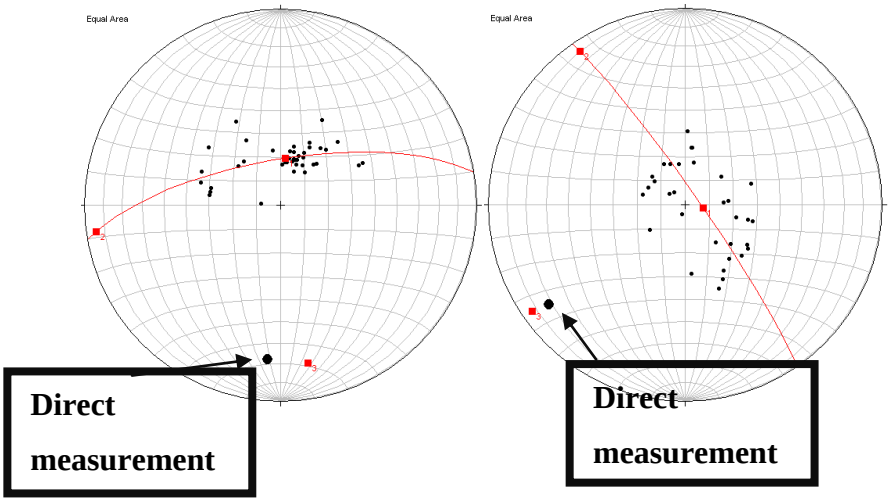

Figure 4.22: Fold axes of A-1 to the left and A-2 to the right, both direct measurements and stereographic (red square).

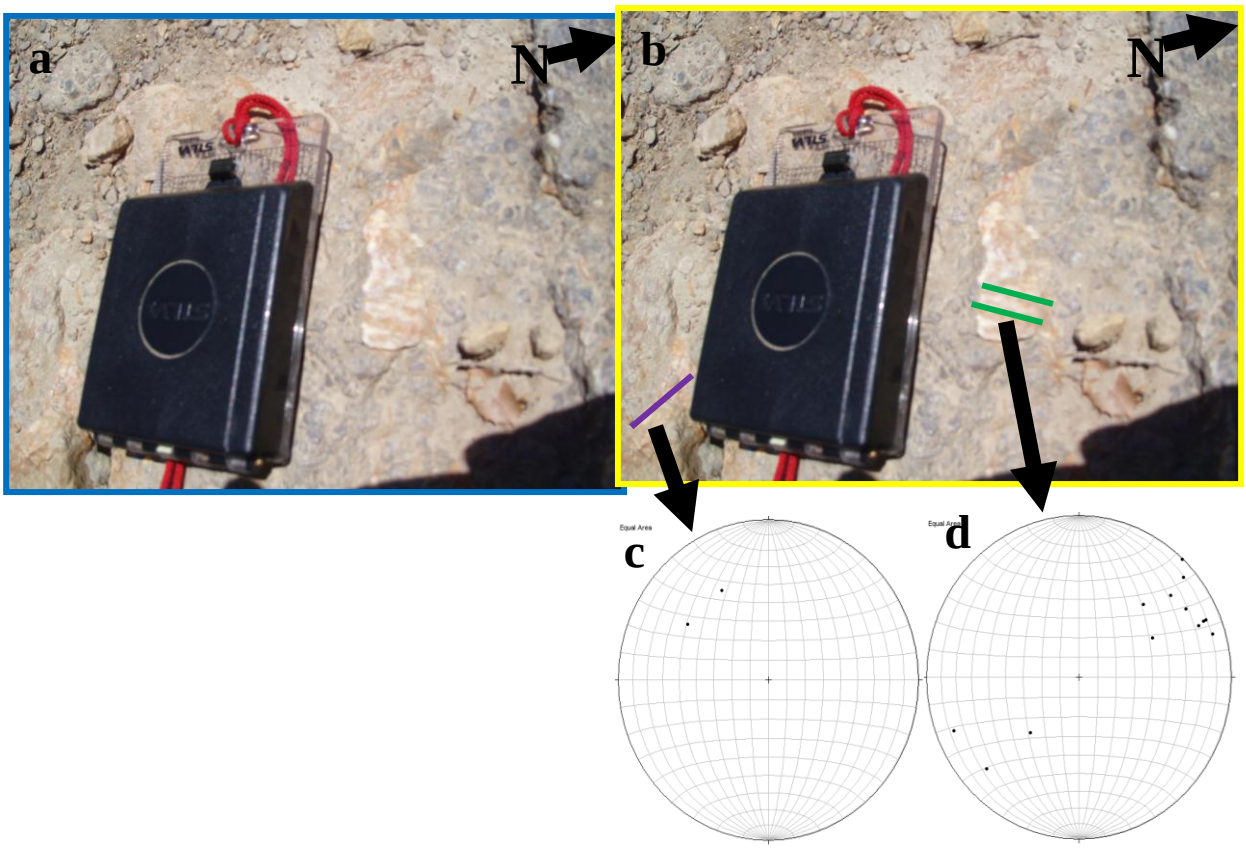

Figure 4.23: a) The two sets of lineations, further illustrated in b. c) Stereoplots of measurements of the lineation set with an average plunge of N315E. d) Stereoplots of measurements of lineation set with an average plunge of N059E.

The southern limb of the third fold, A-3, is exposed and influencing the rocks over most of the Lascorz area, except at central Caixicar de pardina, where A-1 and A-2 influences the rocks. The average orientation of bedding is N119E, indicating a NW-SE trend of the fold axis, approximately N299E. The dip of the beddings is constant, with an average of 23^{o} towards southeast. Its fold axis is parallel to the Cotiella Nappe system, represented in the northeastern Ainsa Basin (Cotiella, Los Molinos and Atiart thrusts), but it is obliquely oriented relative to the overall macro scale structures in the Pyrenees, together with the two other anticlines A-1 and A-2 (figure 4.24 and 25). A-3 is an open anticline with a wavelength of approximately 3, 5 kilometers, and the amplitude is approximately 600 meters.

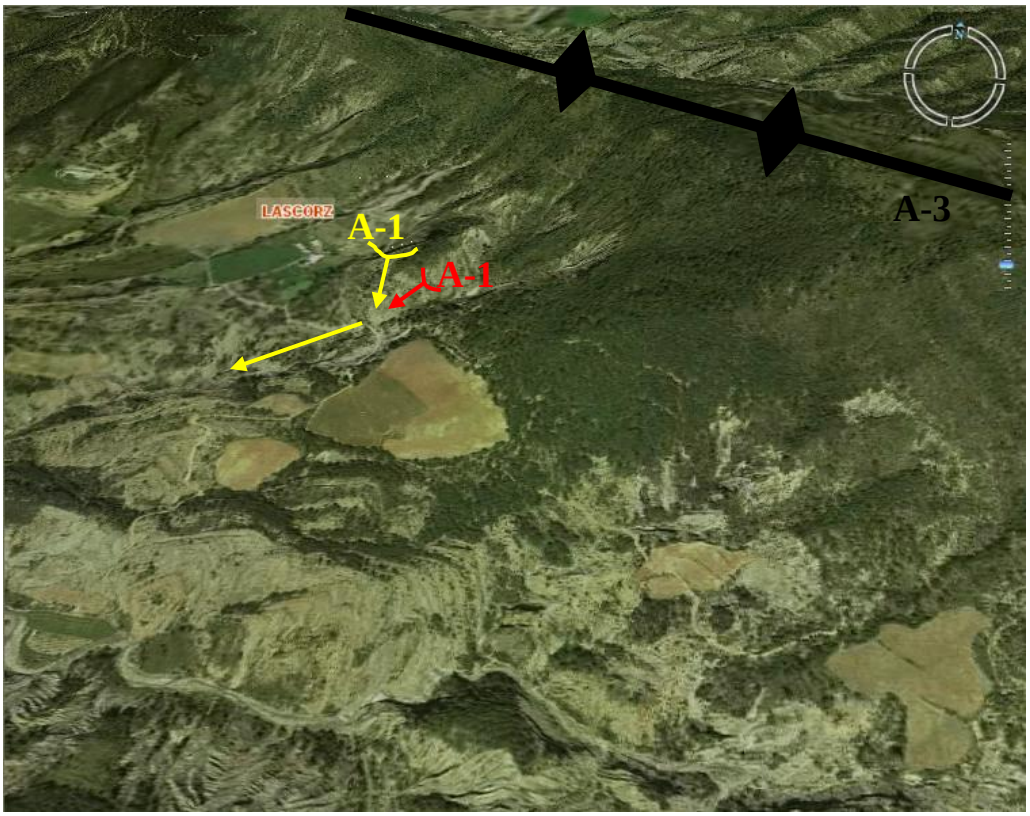

Figure 4.24: Aerial photo of Lascorz showing presence of the three anticlines A-1, A-2 and A-3. A-1 and A-2 strikes in the same direction as the arrows, while strike direction of A-3 it either northwest or southeast (approximately N280E or N100E). Aerial photo from Aragon 3D (2007).

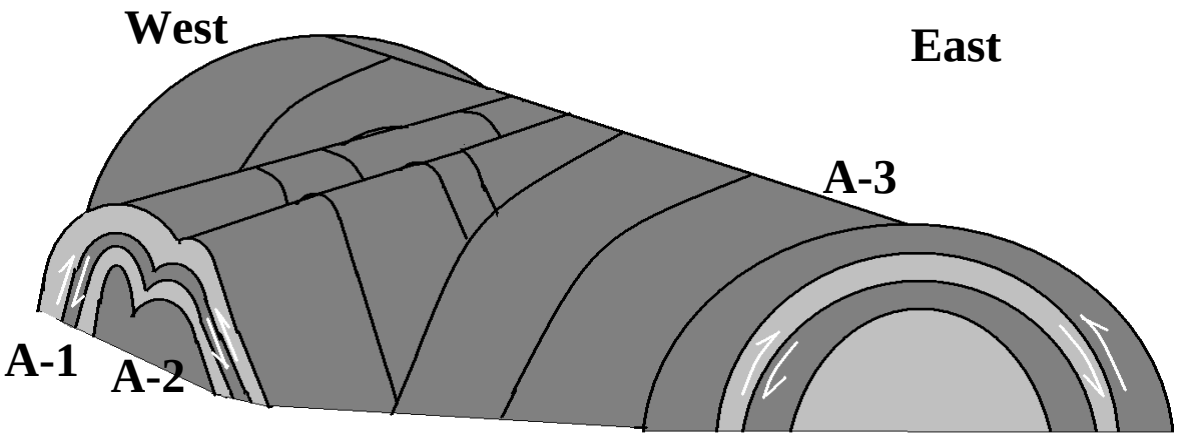

Figure 4.25: Orientation of the three folds relative to each other.

4.3.2 – Fractures

Fracture measurements were pursued at five localities in Lascorz, and these are presented in a sequence so that the least deformed localities are presented first. Fractures at central Caixicar de Pardina is therefore presented first, followed by northern Caixicar de Pardina, northern Fuensalada, central Fuensalada and southern Fuensalada (figure 4.26). Of the five localities at Lascorz, three of them are accessible by car, while a three minutes walk is needed to access northern Caixicar de pardina and southern Fuensalada.

As previously mentioned, nine fracture populations were observed in the Lascorz area (L1-L9) Populations L1 and L2 were observed in both northern Caixicar de Pardina and central Fuensalada. Since northern Caixicar de Pardina is less deformed then central Fuensalada, L1 and L2 fractures from central Fuensalada are included when describing the structures in northern Caixicar de Pardina.

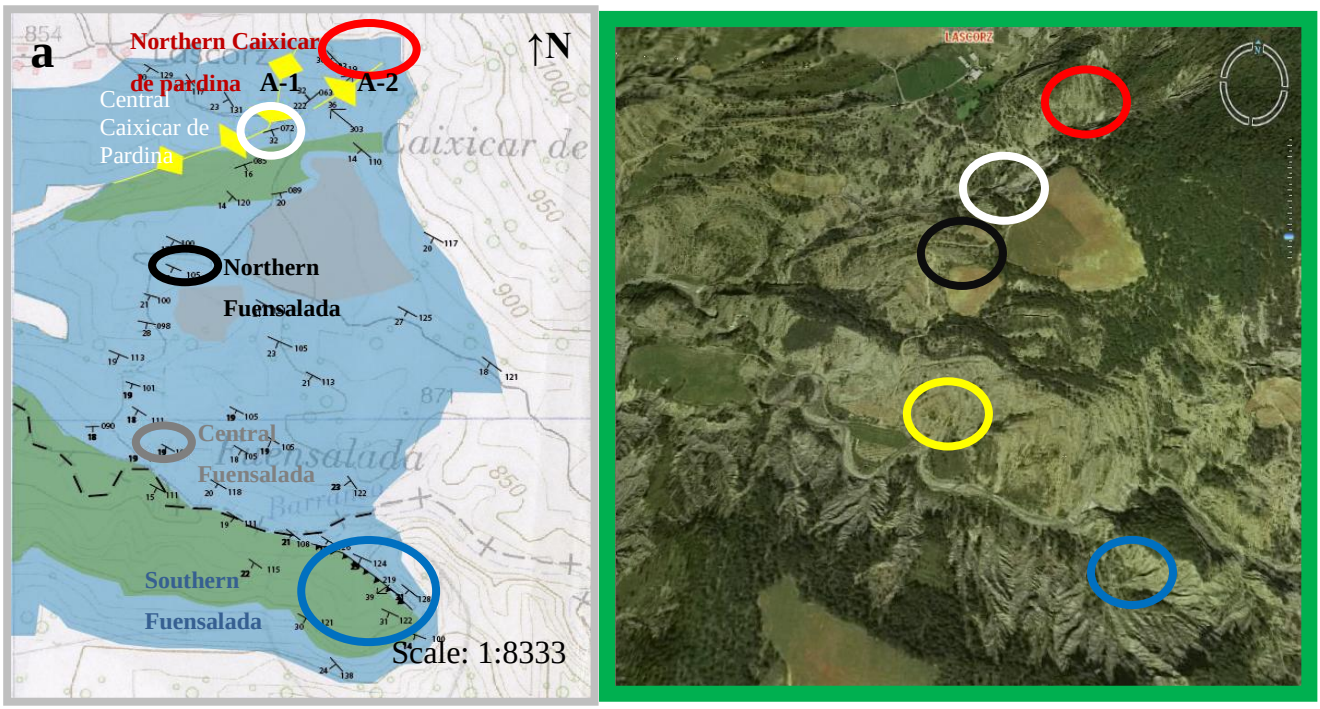

Figure 4.26: a) Geological map of Lascorz. Fracture patterns were observed and documented at the localities marked on the map. b) Aerial photo of Lascorz. The localities are marked and the colors correspond with a (from Aragon 3D, 2007).

4.3.2.1 - Fractures at central part of Caixicar de Pardina

Central Caixicar de Pardina is located at the fold axis of A-1 (figure 4.26). The UTM is 31279554 E, 4697451 N. The locality is represented by an excellent exposed 25 meters broad and five meters high section (figure 4.27). The sedimentary sequence consists of calcareous sandstones interbedded with mudstones, with an increasing sandstone/mudstone ratio upwards in the section. The overall geological setting and Lithological nature is the same as for Lascorz overall. The average orientation of the bedding (S_0) is N082E, and the average dip is 27^o towards SSE.

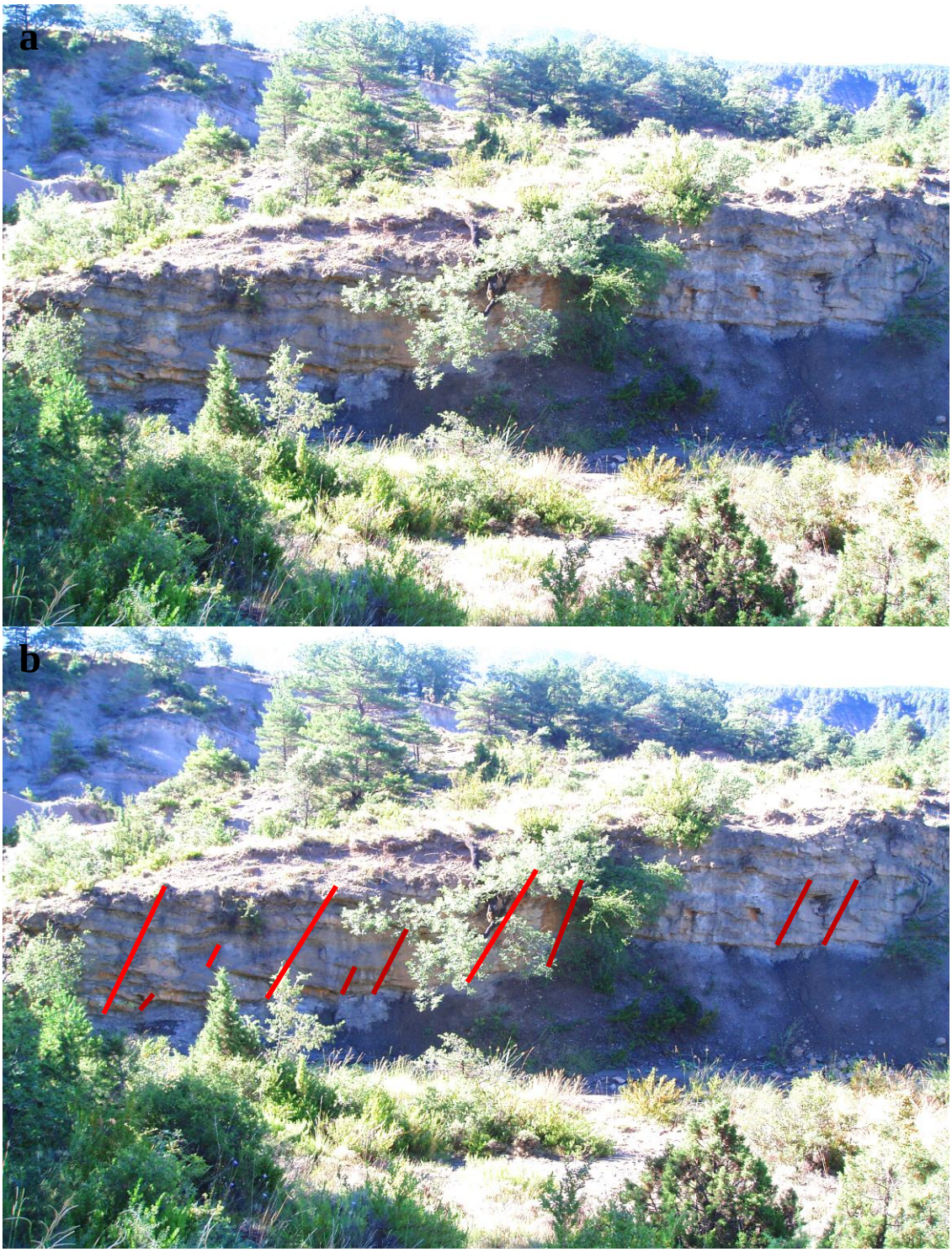

Figure 4.27: a) Section representing central Caixicar de Pardina. b) Ten of the 17 faults are marked. The last seven fractures are located behind the vegetation to the left and in central parts of the picture.

Central Caixicar de Pardina is characterized by a system of parallel faults (figure 4.27), which display normal displacement. Orientation of the faults, together with offset along them, can be measured directly, and the normal displacement across each fault is rather variable, from 1 centimeter to 1, 5 meters.

Seventeen faults are exposed in the 25 meter broad section at central Caixicar de Pardina. All faults are parallel (figure 4.28), were nine of the faults have a straight morphology, whereas the last eight are curved. Four of the 17 faults are calcite cemented, and the average orientation of the fault planes is N321E with an average dip of 45^{o} towards northeast. All faults at central Caixicar de pardina have one or several of following characteristics (figure 4.29):

1. The thickness increases towards the fault.
2. The lower boundary between limestone and mudstone are rounded at the faults. This illustrate that the sediments where still not consolidated during faulting.
3. Beds that are located higher up in the section are not faulted.

Compared to Las Uslas, Caixicar de Pardina is not characterized by numerous fault blocks, but consists of several minor fault planes. The respective hanging walls consist of calcareous sandstones faulted into underlying mudstones.

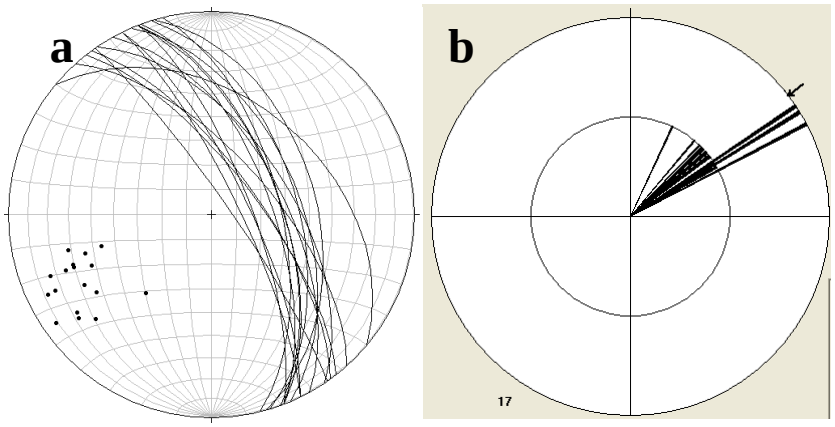

Figure 4.28: a) Measurements of strike and dip at central Caixicar de Pardina b) Rose diagram illustrating direction of faulting of the syn-sedimentary faults. The circles within the rose diagram represents amount of faults with that particular orientation of dip.

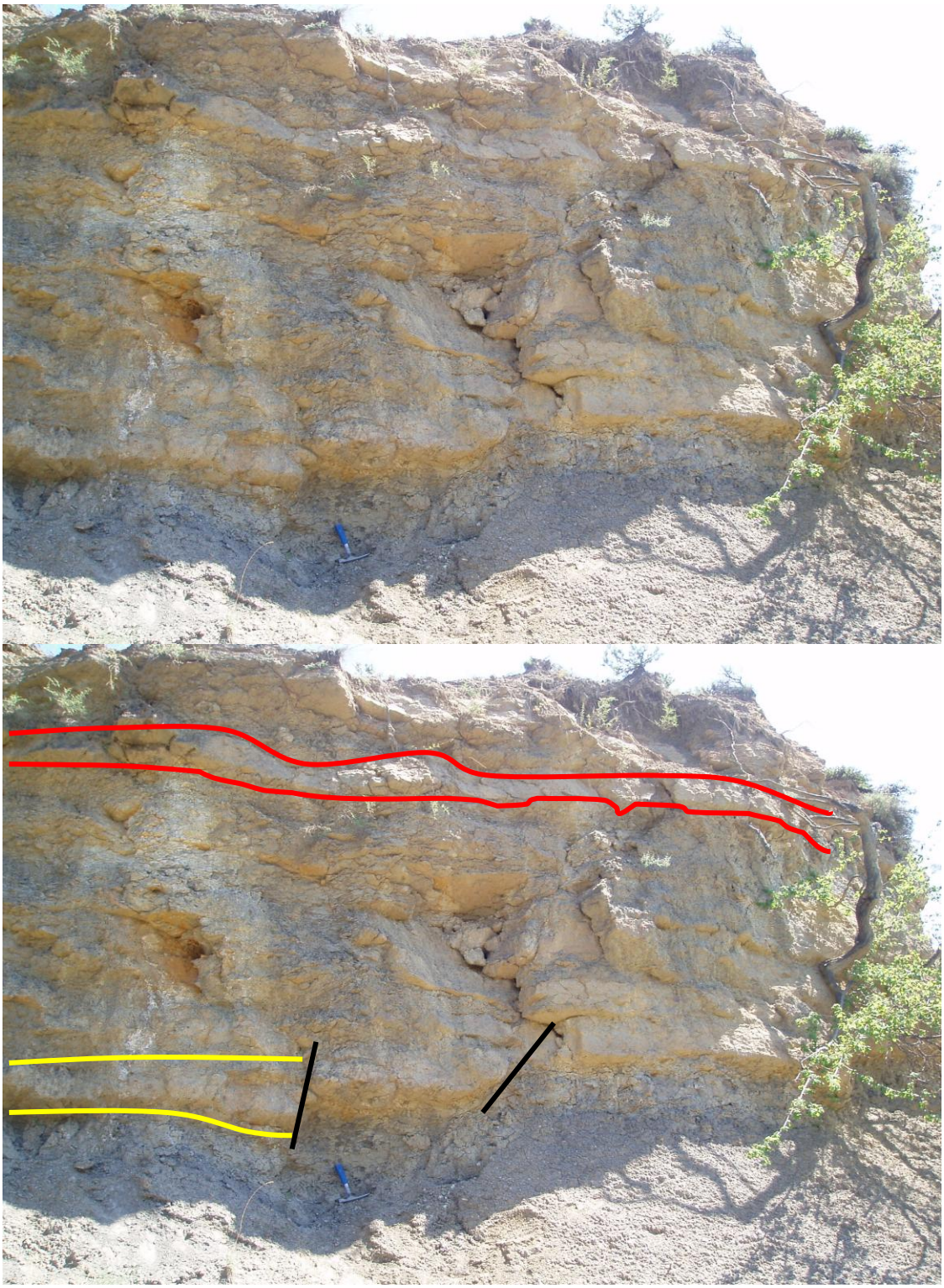

Figure 4.29: Illustration of the three characteristic features represented at Caixica. The fault (dark line) is rounded in the transition between sandstone and mudstone, and the sandstone bed, marked by red lines, is not faulted. The sandstone marked by yellow lines is thickening towards the fault straight above the hammer. The picture is taken from locality 2, marked in figure 4.14.

Interpretation

As mentioned above, the calcareous sandstone beds become gradually thicker towards the faults, the corners at the transition between mudstone and sandstone at the faults are rounded and beds immediately above the faulted sequences are un-faulted. These are the three criteria for syn-sedimentary faulting (described in section 1.4). The fractures are therefore thought to be syn sedimentary faults. Since the faults are syn-sedimentary, the faults must be re-oriented according to the superimposed tectonic gradient. By re-orienting the faults according to the superimposed regional tectonic gradient, true orientation of the faults at the time of development are found. Since the area is mostly influenced by A-3, the faults are re-oriented according to the orientation of this fold (using the method described by Ramsay (1961)). By doing this, a similar orientation, but steeper dip of the faults are obtained (figure 4.30). The direction of faulting, and thereby the down-dip direction, was towards northeast.

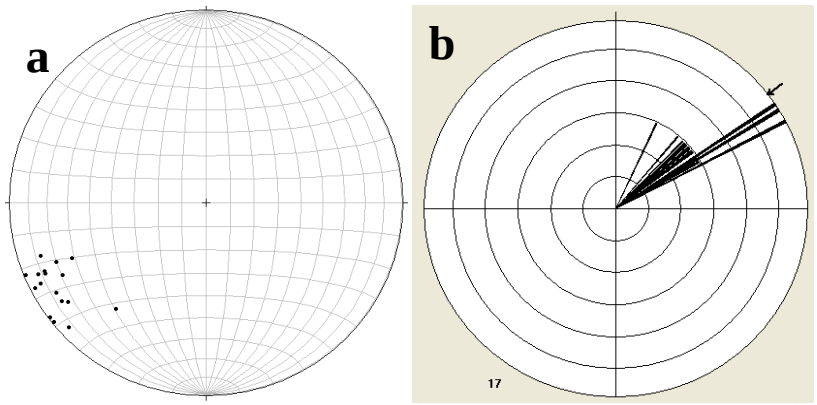

Figure 4.30: a) Measurements of strike and dip of the various syn-sedimentary faults after re-orienting them according to the regional tectonic gradient. b) Direction of movement was towards northeast, illustrated by the rose diagram.

4.3.2.2 - Fractures at the northern part of Caixicar de pardina

Northern Caixicar de pardina is represented by a 10 meter long section in E-W direction and 15 meters in N-S direction. The locality is 300 meters northeast from were direct measurements of the fold axes were pursued (described in section 4.3.1), with the UTM equal to 31279743 E, 4697671 N. The locality represents the surface of the ground, so thickness of the bedding cannot be documented. The average orientation of the bedding (S_0) is N103E, with a dip of 29^o towards southwest. The locality is characterized by two fracture

populations (denoted L1 and L2), distinguished by their orientation since architecture; mode and presence of calcite cement are similar. Both populations L1 and L2 were also observed in central Fuensalada (figure 4.26; a locality described in section 4.3.2.4). These fractures, in central Fuensalada, are therefore described in this section.

Population L1

Population L1, documented at northern Caixicar de pardina and central Fuensalada, has an average orientation of N259E, with an average dip of 60^{o} towards north, i.e. vertical relative to bedding (figure 4.31 and 4.32). 14 fractures were documented in northern Caixicar de Pardina, whereas 17 fractures were documented from bed four and five at central Fuensalada (figure 4.33; table 4.4). All population L1 fractures, in both localities, are straight with en echelon architecture. Calcite cement was observed in all fractures, and their average thickness is eight centimeters. The fractures are penetrating through the beds and their minimum lengths are approximately 10 meters, but cannot be measured accurately since they exceed the exposures in both localities. The fracture frequency is 1, 07 fractures per meter in northern Caixicar de Pardina and 1, 15 in central Fuensalada.

Interpretation population L1

Population L1 fractures are strike-slip fractures, mainly based on the en echelon architecture of the fractures, together with the close to vertical dip relative to bedding. This population has similar mode and orientation as Q5, documented from Ainsa Quarry, and they have developed during tectonic contraction.

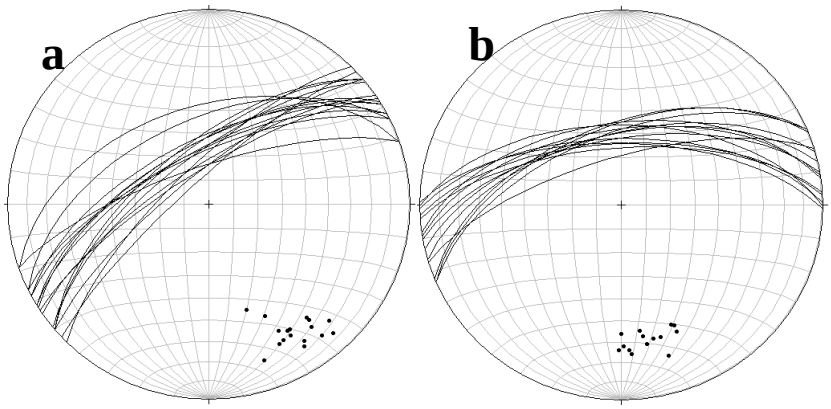

Figure 4.31: Measurements of strike and dip of population L1 fractures at central Fuensalada and northern Caixicar de Pardina.

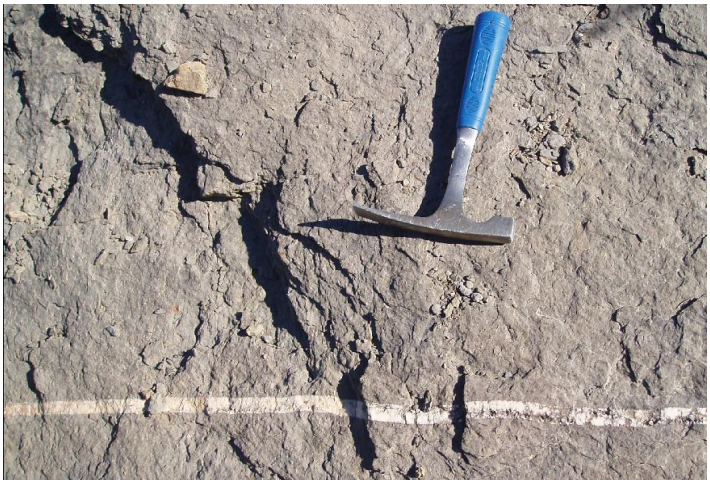

Figure 4.32: Population L1 fracture at central Fuensalada. Hammer as scale

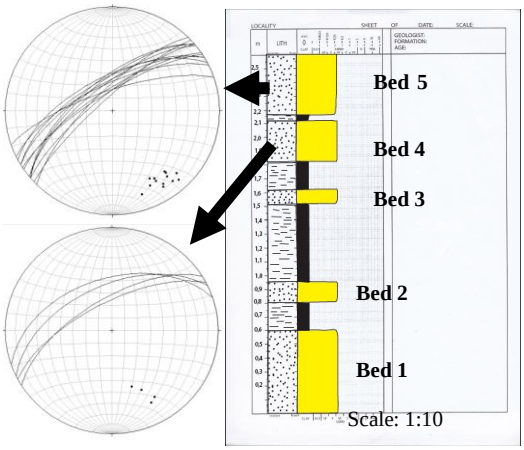

Figure 4.33: Measurements of strike and dip of population L1 fractures in bed four and five at central Fuensalada (described in detail in section 4.3.2.4).

Locality / Shape	Northern Caixicar de Pardina	Central Fuensalada
	14	17
	14	17
	14	17
Fracture Frequency	1, 07 fractures per meter	1, 15 fractures per meter
Minimum lengths	10 meters	10 meters

Figure 4.4: Relationship between population L1 at northern Caixicar de Pardina and central Fuensalada.

Population L2

Population L2 at northern Caixicar de pardina and central Fuensalada has an average orientation of N335E and dips 73^{o} towards northwest (figure 4.34 and 4.35). Three fractures were documented at northern Caixicar de Pardina, were all are straight, whereas 19 fractures are documented from central Fuensalada, were six are straight, 11 wiggly and one is curved (table 4.5). All population L2 fractures, at both localities, have en echelon architecture. Calcite cement was observed in all fractures, both northern Caixicar de Pardina and central Fuensalada. The fractures have an average thickness of eight centimeters, and their depths are equal to the thickness of the beds. Population L2 fractures has a minimum length of approximately 15 meters in northern Caixicar de Pardina, whereas their minimum lengths are 10 meters in central Fuensalada. As with population L1, the accurate length is not possible to measure since they exceed the exposures. The fracture frequency at northern Caixicar de Pardina is 0, 3 fractures per meter, whereas it is 0, 3 and 0, 6 in bed one and five, respectively, at central Fuensalada.

Interpretation population L2

Populations L2 fractures are strike-slip fractures, mainly based on their en echelon architecture. These fractures have developed during tectonic contraction, similar to population L1.

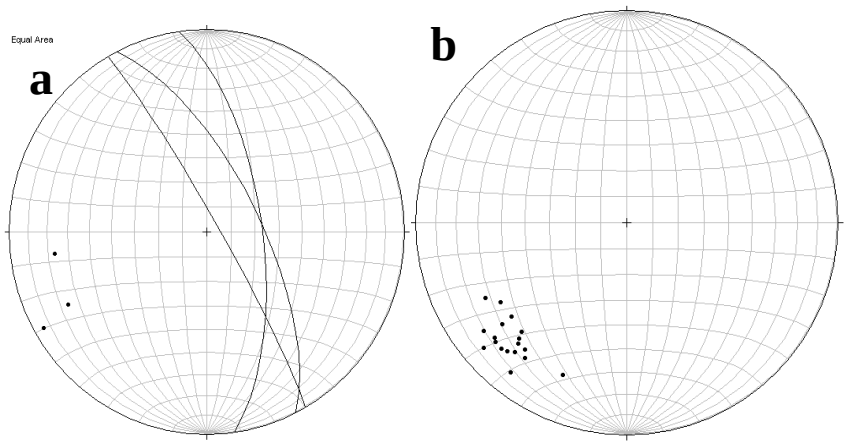

Figure 4.34: a) Plot of strike and dip measurements of fracture population L2 at northern Caixicar de pardina. b) Plot of strike and dip measurements of fracture population L2 at central Fuensalada

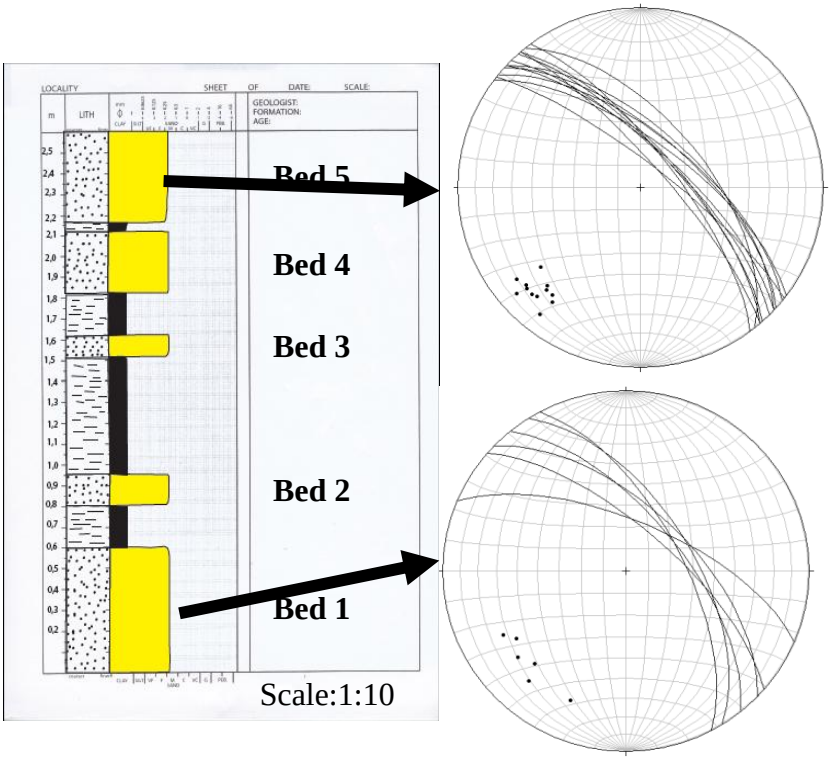

Figure 4.35: Measurements of strike and dip of the population L6 fractures in bed one and five at central Fuensalada.

Locality / Shape	Northern Caixicar de Pardina	Central Fuensalada
	3	19
	3	19
	3	6
		11
		1
Fracture Frequency	0, 3	0, 6
Minimum lengths	15 meters	10 meters

Table 4.5: Relationship between population L2 at northern Caixicar de Pardina and central Fuensalada.

4.3.2.3 - Fractures in the northern part of Fuensalada

Northern Fuensalada, with its systematic fracture pattern, has the UTM equal to 31279244 E, 4697297 N (Figure 4.36). The northern Fuensalada is located on the southwestern limb of A-3, and the locality is situated on the upper surface of one 12 centimeters thick calcareous sandstone bed. Fractures at the northern Fuensalada were measured from an area which is 8, 5 meters wide in the E-W direction, and 11 meters wide in the N-S direction. The local orientation of the bedding is N115E, with an average dip of 21^{o} towards southwest. 65 fractures were measured at northern Fuensalada altogether, divided in two populations based on orientation, since mode, lack of calcite cement and architectures are similar in both populations (i.e. population L3 and L4; figure 4.37). The fracture frequencies of population L3 and L4 are 2, 75 and 4, 1, respectively (figure 38).

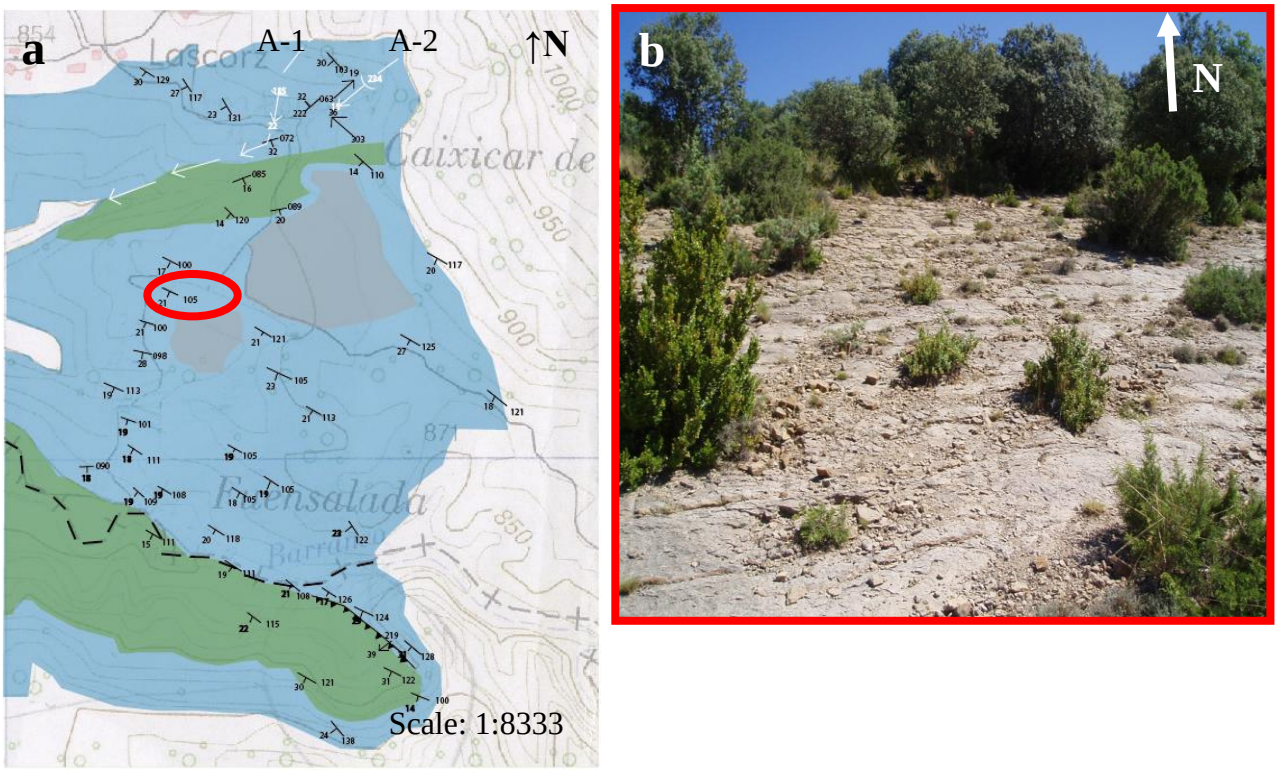

Figure 4.36: a) Geological map of Lascorz, where the northern part of Fuensalada is marked by the red circle. b) Overview picture of northern Fuensalada.

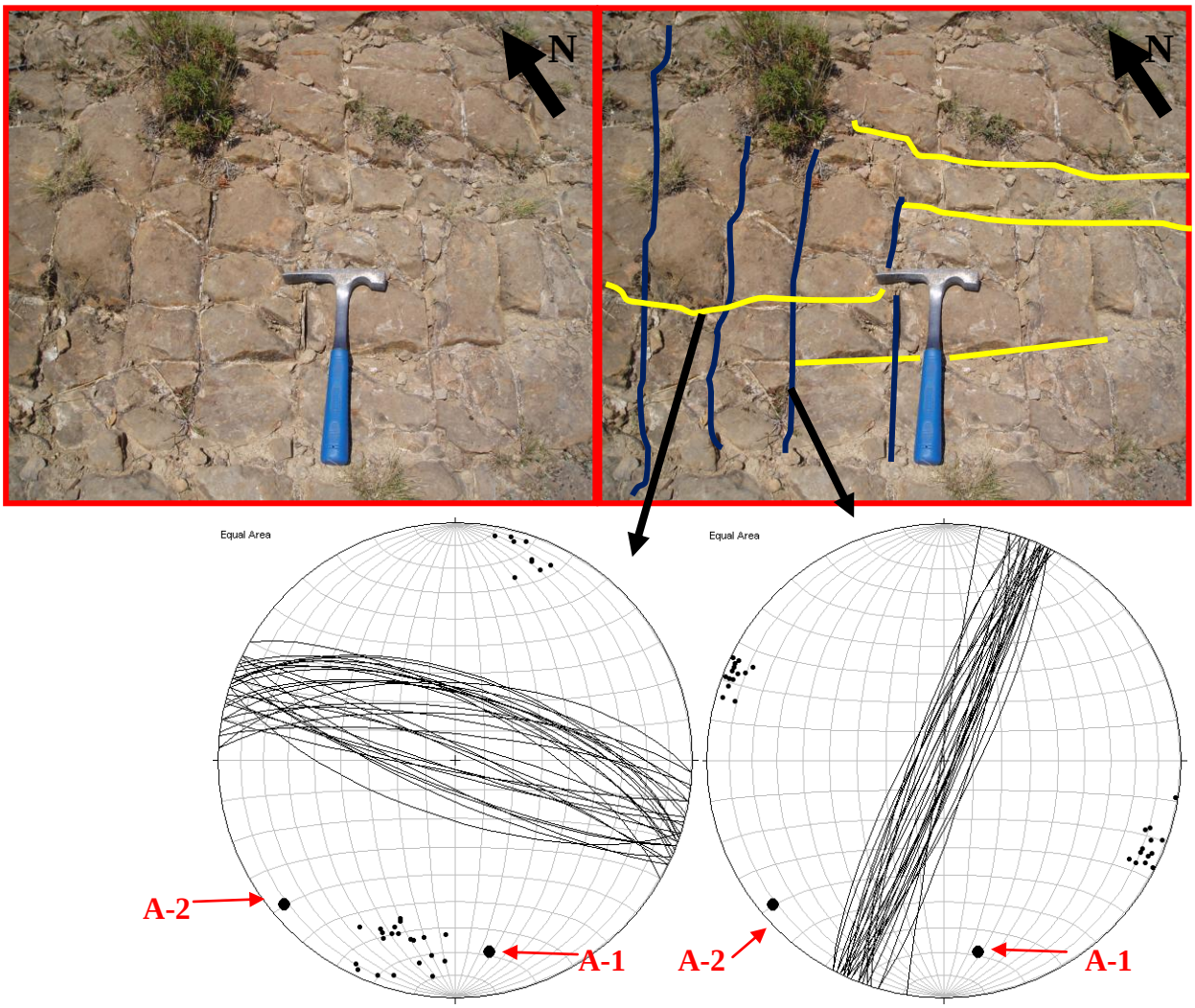

Figure 4.37: The two fracture populations at northern Fuensalada. The stereoplot to the left is of population L3 (yellow lines), and to the right is population L4 (blue lines). The fold axes of A-1 and A-2 are the ones found stereographically.

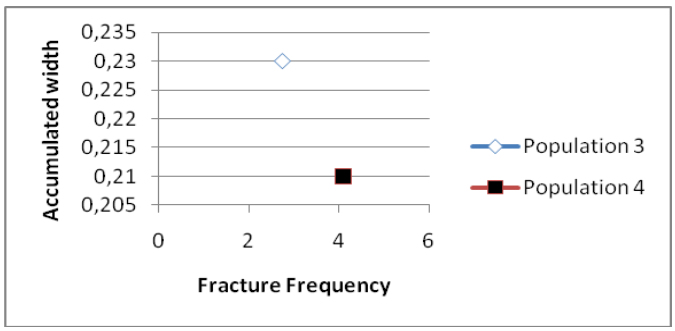

Figure 4.38: Fracture frequency of populations L3 and L4.

Population L3

Population L3 fractures are mode I fractures and they have an average orientation towards N200E, and dips 71^{o} towards northwest (i.e. vertical relative to bedding (S_0)). 33 fractures belong to this population, were 14 of them are straight, 15 are wiggly and the last four are curved (table 4.7). Each fracture is represented by one single plane, branching out from population L4 fractures in an orthogonal fracture pattern (figure 4.37). None of the fractures are calcite cemented, but all of them contain clay-fill. The average width of the fractures is 6, 9 millimeters together with an average length of 1, 3 meters. Fracture frequency of population L3 is 2, 75 fractures per meter (figure 4.38).

Population L4

Population L4 fractures are tensile fractures and they have an average orientation towards N290E, and dips 72^{o} towards northwest (i.e. vertical relative to bedding (S_0)). 32 fractures belong to this population, were all of them are straight. Each fracture is represented by one single plane in an orthogonal fracture pattern together with population L3 (figure 4.37). None of the fractures are calcite cemented, but all of them contain clay-fill. The average width of the fractures is 6, 6 millimeters and their average length is 1, 2 meters. Fracture frequency of population L3 is 4, 1 fractures per meter (table 4.7).

Interpretation populations L3 and L4

Orthogonal fracture patterns due most often develop during burial, population L3 and L4 have developed during mechanical compaction (orthogonal fracture pattern described in section 1.4). Simultaneously, fractures in both populations have similar properties (e.g. mode and geometry) as population Q1, Q2 and Q3 in Ainsa Quarry, which strengthens this hypothesis since Q1, Q2 and Q3 are related to burial.

	Population L3	Population L4
	33	32
	4	0
	15	0
	14	32
Average width	6, 6 mm	9 mm
Average length	1, 2 meters	1, 3 meters
Fracture frequency	4,1 fractures per meter	2, 75 fractures per meter

Table 4.7: Amount of population L3 and L4 fractures with the various shapes (see section 1.4 for further description).

4.3.2.4 - Fractures in the central part of Fuensalada

Central Fuensalada is located at the Barranco River on the southwestern limb of A-3 (figure 4.39). The UTM for this locality is 31279198E, 4696957N. The average orientation of the bedding (S_0) is N107E, with an average dip of 21^o towards southwest. The entire section making up locality 5 is 20 meters broad in the N-S direction, 20 meters in the E-W direction and 5 meters vertically (figure 4.40). The lithologies at central Fuensalada are the same as for the rest of Lascorz, with calcareous sandstones interbedded with mudstones. All fractures are documented in calcareous sandstones, and one rock sample was gathered from bed number two to investigate the host rock in thin section (figure 4.41). The calcareous

sandstone is composed of calcite mostly, were the main component is fossil fragments of nummolites.

Central Fuensalada is interesting from a structural geological point of view due to its prominent fracture system. The fractures are documented from the upper surface of calcareous sandstone beds, whereas the mudstones between are un-fractured. Together with populations L1 and L2, described in section 4.3.2.2, three populations are recognized, separated according to their geometry, fracture fill and orientation (figure 4.42). Fractures with similar characteristics are considered the same population even when they appear in different beds.

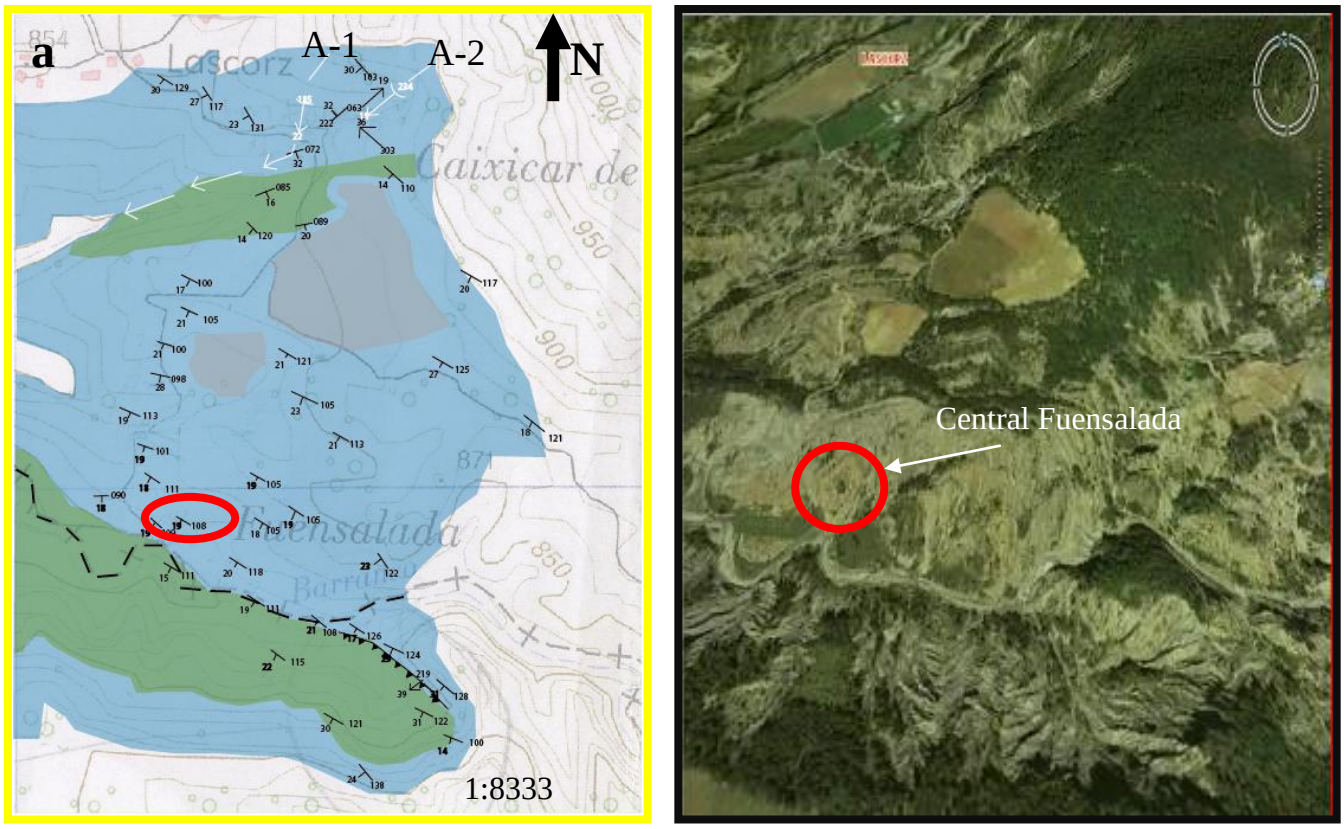

Figure 4.39: a) Geological map of Lascorz, were central Fuensalada is marked in red. b) Aerial photo of Lascorz were central Fuensalada is marked in red (from Aragon 3D, 2007).

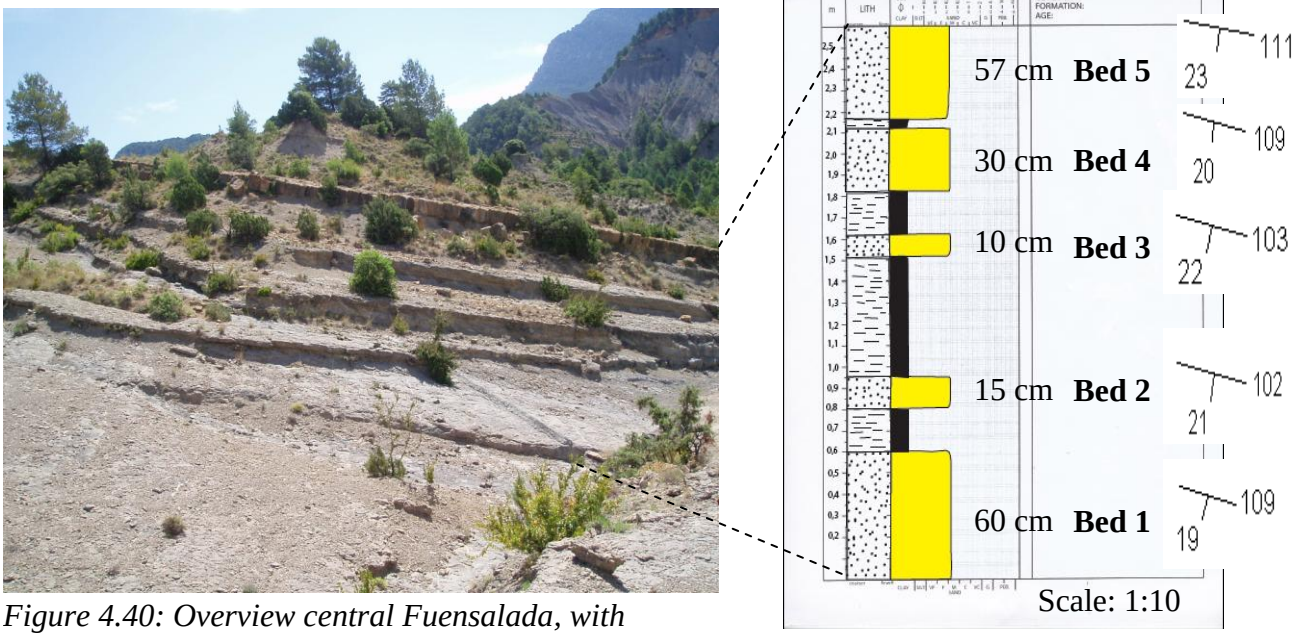

Figure 4.40: Overview central Fuensalada, with corresponding sedimentary log.

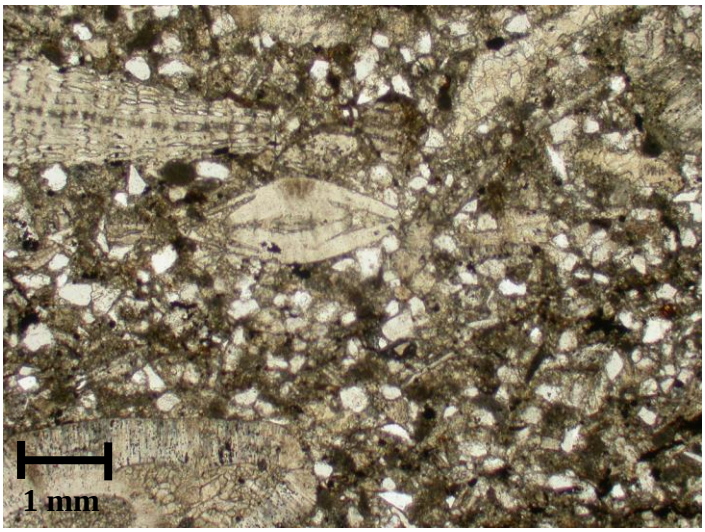

Figure 4.41: Host rock at central Fuensalada. Several fossils are observed in the picture. The matrix consists of mainly fossil fragments. The picture is taken with 5 optical zoom.*

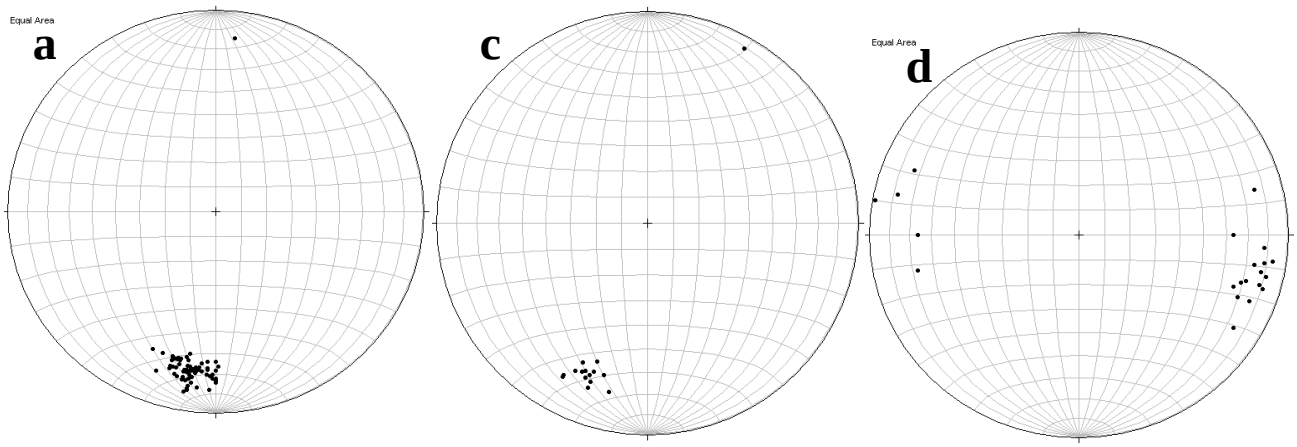

Figure 4.42: a) Measurements of strike and dip of population L5 fractures. b) Measurements of strike and dip of population L7 fractures c). Measurements of strike and dip of population L8 fractures.

Population L5

Population L5 fractures have an average strike, regardless of which bed they are located in, of N280E and dips 69^{o} towards NNE, which indicate a sub-parallel strike of the fractures relative to the bedding (S_0) (figures 4.43 and 4.44). The fractures are systematically distributed, with equal spacing between individual fractures. Population 5 consists of 73 fractures altogether, represented by 53 straight, 19 wiggly and one curved (table 4.8). All fractures are comprised by one single line, together with presence of calcite cement. Thin sections of fracture fill were investigated, showing calcite growth parallel to the opening direction of the fractures, together with one median in the central part of the fractures (figure 4.45). The fractures are cutting vertically through the beds they are located in, with an average length of 14 meters and average width of 34 millimeters. Their lengths are most probably longer, but the fractures exceed the length of the exposure making accurate measurements impossible.

In bed five, population L5 fractures are observed to cut population L8 fractures (described in detail further down) (figure 4.46), whereas populations L1 and L2 fractures (described in section 4.3.2.2) are observed to cut population L5 (figures 4.47 and 4.48).

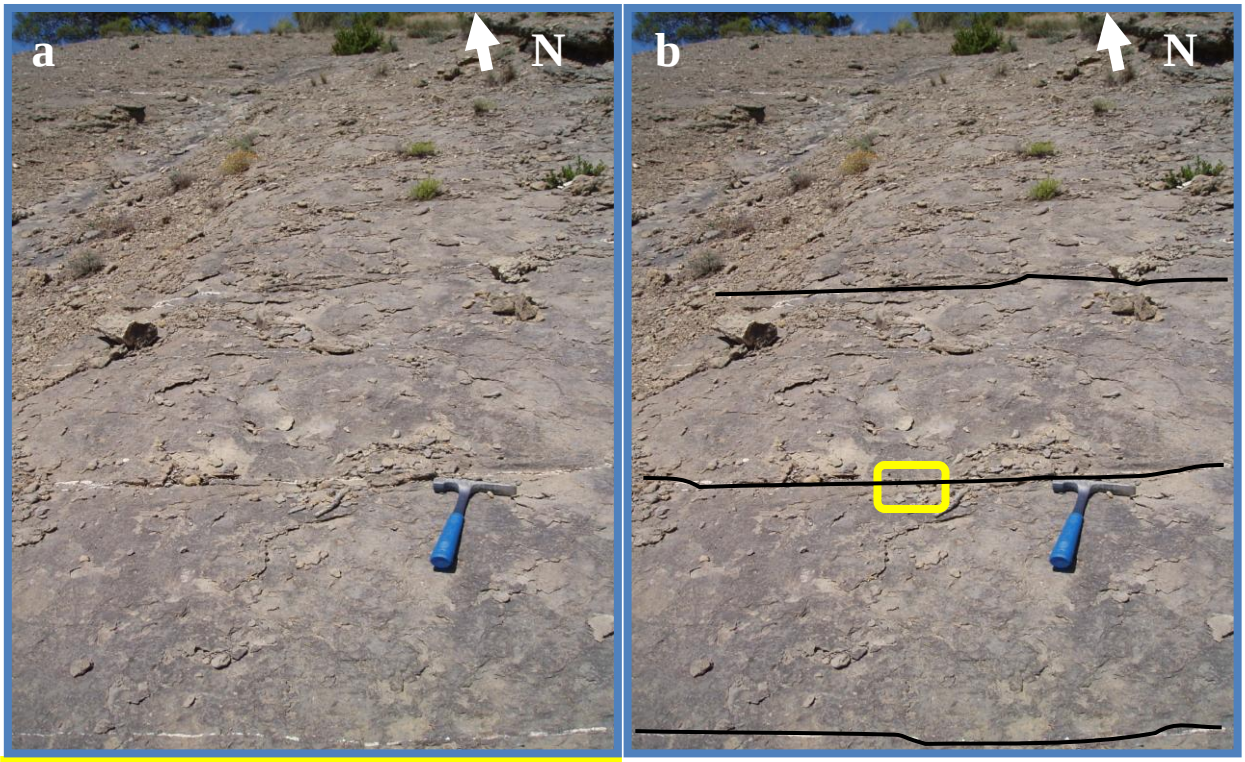

Figure 4.43: a and b) Population L5 fractures at central Fuensalada. c) Detailed picture of a population L5 fracture at central Fuensalada. The picture corresponds with the yellow square in b.

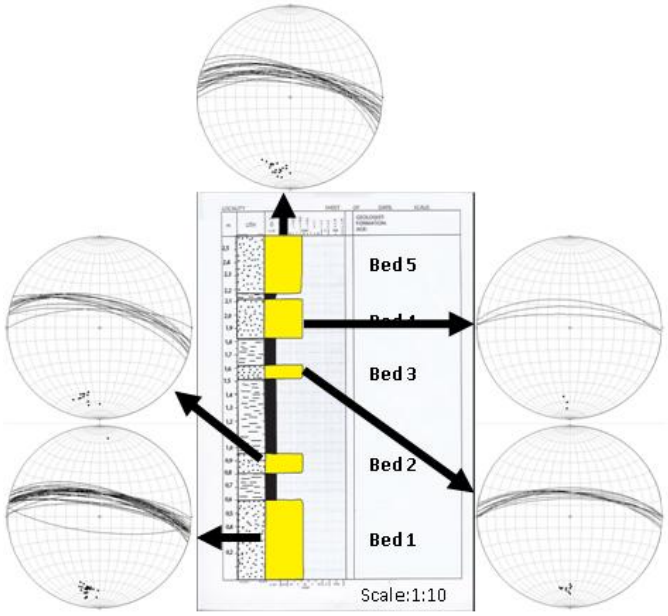

Figure 4.44: Stereoplots of strike and dip measurements of population L5 fractures in the various beds at central Fuensalada.

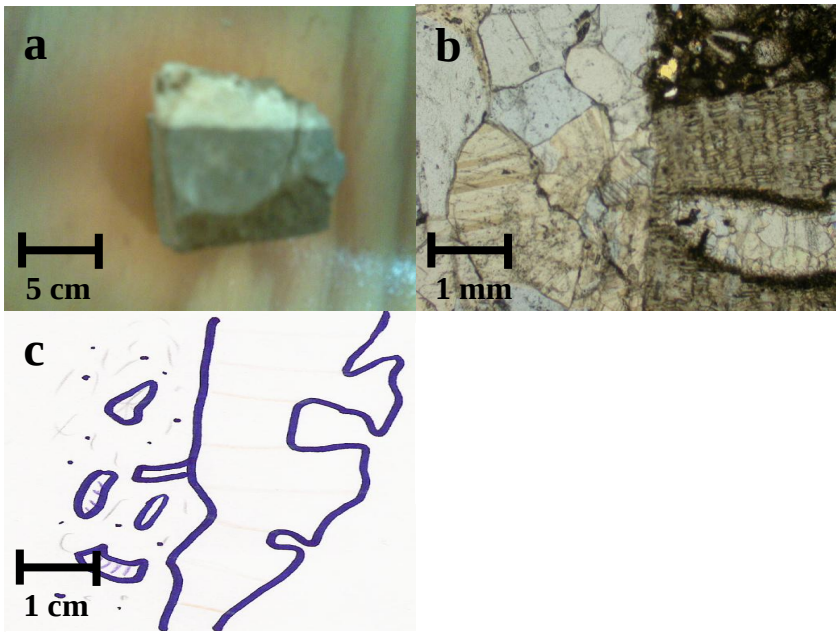

Figure 4.45: a) Rock sample of L5 fracture. b) Thin section, illustrating cutting of fossil fragment together with tensile growth (5 optical zoom). c) Drawing of the thin section.*

Figure 4.46: Population L5 fracture (black line) cutting population L8 fracture (red line).

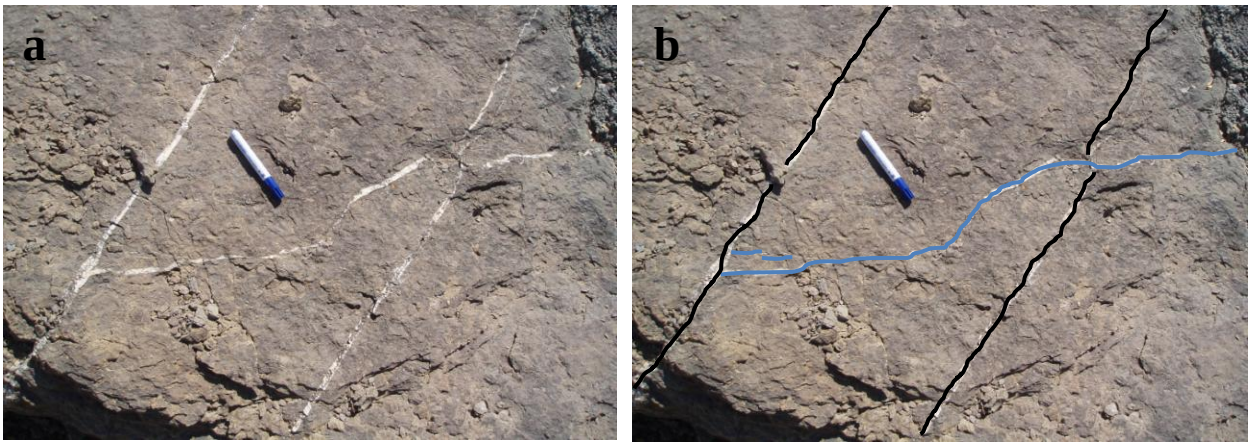

Figure 4.47: a) Population L5 fracture offset by a population L2 fracture. The fractures are marked in b with black lines and blue line, respectively.

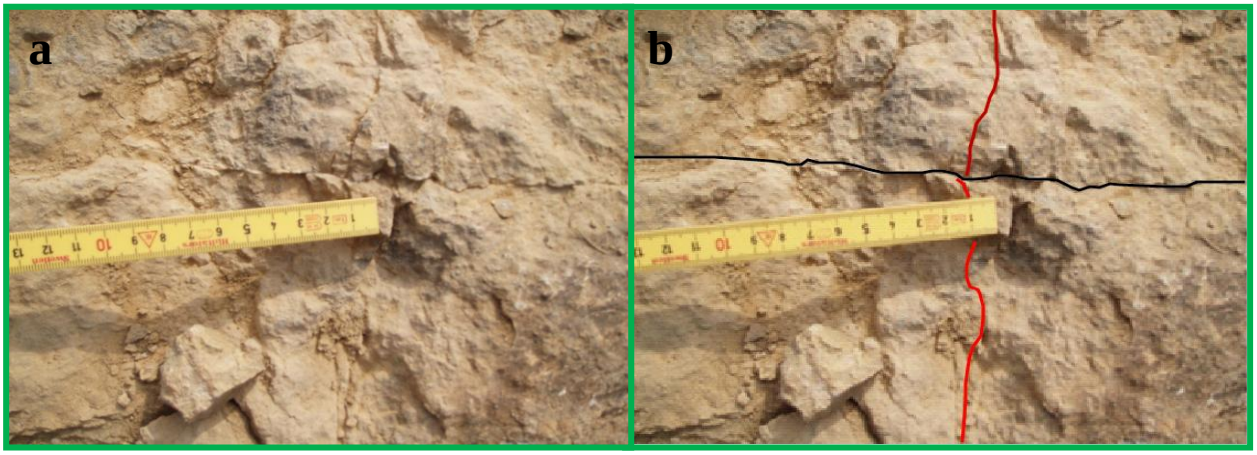

Figure 4.48: a) Population L5 fracture cut by a population L1 fracture. The fractures are marked with red and black lines in b, respectively.

Interpretation population L5

Due to the morphology of the calcite cement, together with the development of one central median, it is suggested that calcite cement has grown syntaxially. It is interpreted that calcite cement grew with its c-axis parallel to the direction of opening, so that fractures were gradually filled in during opening of the fractures. The morphology and architecture of this fracture population is very un-similar with the fractures documented in the Ainsa Quarry. Population L5 fractures are interpreted to be tectonically derived.

Population L6

Population L6 fractures are localized in bed three and four, and have an average orientation of N296E – N116E and dips 88^{o} towards SW-NE (figures 4.49 and 4.50). Fractures are documented, were all patterns described in section 1.3 are represented, with 10 straight, four wiggly and one curved. Eleven fractures are comprised by one single plane, whereas the last four have en echelon architecture. The fractures are open with an average width of 4 millimeter, and neither shear displacements were observed along the fractures, nor any fracture fill (table 4.8). They have an average length of 1, 5 meters, recorded on the upper surface of the beds. The fractures are evenly distributed in bed three and four.

Interpretation population L6

Population L6 fractures are tensile, and the fractures have similar characteristics as the fracture population Q4 documented from the Ainsa Quarry. Population L6 have formed during mechanical compaction.

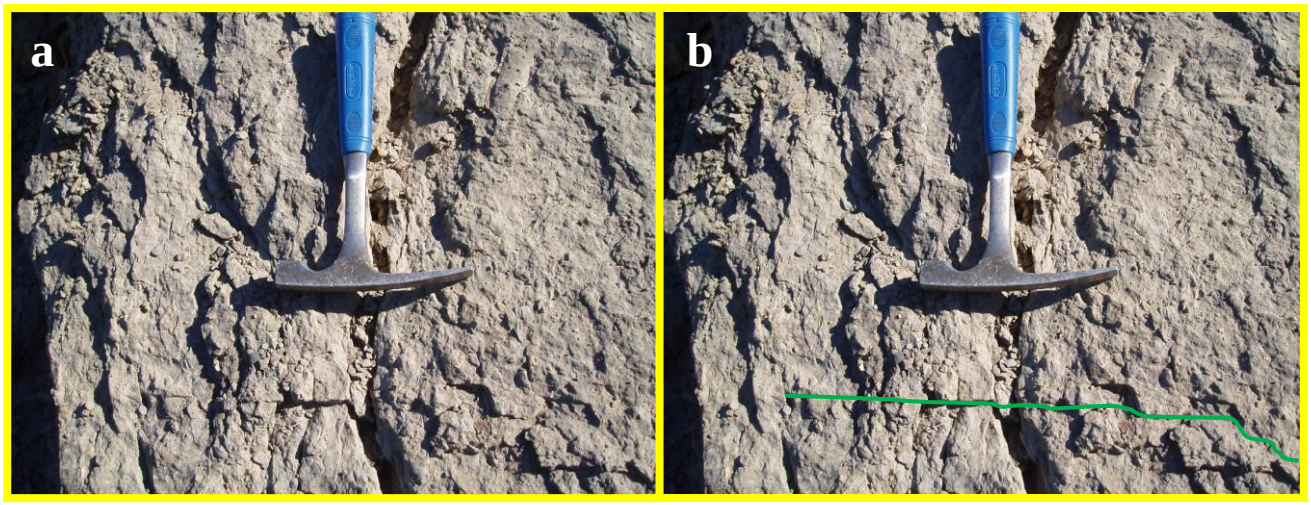

Figure 4.49: a and b) Example of population L6 fracture in bed four at central Fuensalada in a, further marked with green line in b. Hammer as scale.

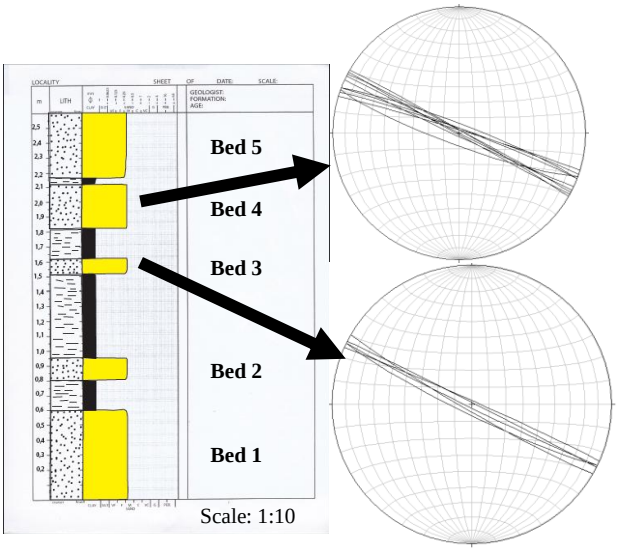

Figure 4.50: Measurements of strike and dip of the various population L6 fractures in bed three and four at central Fuensalada.

Population L7

Population L7 fractures was observed in bed two, three and five, with an average orientation of N192E and dips 75^{o} towards WNW (figures 4.51 and 4.52), which indicate a perpendicular orientation relative to the fold axis of A-3. 21 fractures are measured altogether, were eight are straight, 10 are wiggly and three are curved (table. 4.8). All fractures are closed, with an average width of two millimeters, and each fracture is represented by one single plane. There are no shear displacements, nor any fracture fill, observed along the fractures. All population L7 fractures seem to penetrate the whole bed,

and their average length is seven meters. As mentioned above, population L7 fractures are cut by population L5 fractures (figure 4.45).

Interpretation population L7

Population L7 fractures are tensile. Due to the perpendicular orientation relative to A-3, these fractures are interpreted to be related to tectonic contraction in the study area. Since population L7 fractures are cut by population L5 fractures, L7 fractures must have developed earlier then population L5 fractures.

Figure 4.51: Picture of population L7 fracture in bed 5. The fracture migrates from upper left to lower right below the hammer. It is not calcite cemented.

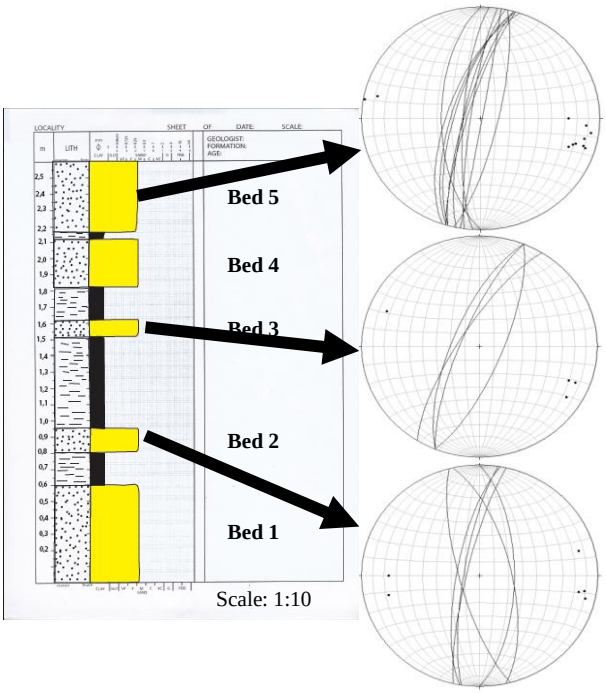

Figure 4.52: Measurements of strike and dip of population L7 fractures in the various beds at central Fuensalada. No population L7 fractures were observed in bed one and four.

	Population L5	Population L6	Population L7
	73	15	21
		4	
	1	1	3
	19	4	10
	53	10	8
Average width	34 mm	4 mm	2 mm
Average length	14 meters	1, 5 meters	7 meters

Table 4.8: Amount of fractures with the various characteristics among populations L5, L6 and L7, recorded from central Fuensalada. See section 1.3 for explanations of the various figures in the table.

4.3.2.5 - Fractures in the Southern Fuensalada

Southern Fuensalada is represented by a ravine (figure 4.53), close to Barranco River. The UTM are around 31279690 E, 4696701 N, and the locality is situated on the southwestern limb of A-3. The depositional environment and age of the sediments are the same as for the rest of Lascorz, described in section 4.3.1. A five minutes' walk along the Barranco River from locality 5 at central Fuensalada is needed to reach the ravine. The average orientation of the beddings (S_0) is N128E, with an average dip of 31^o towards southwest.

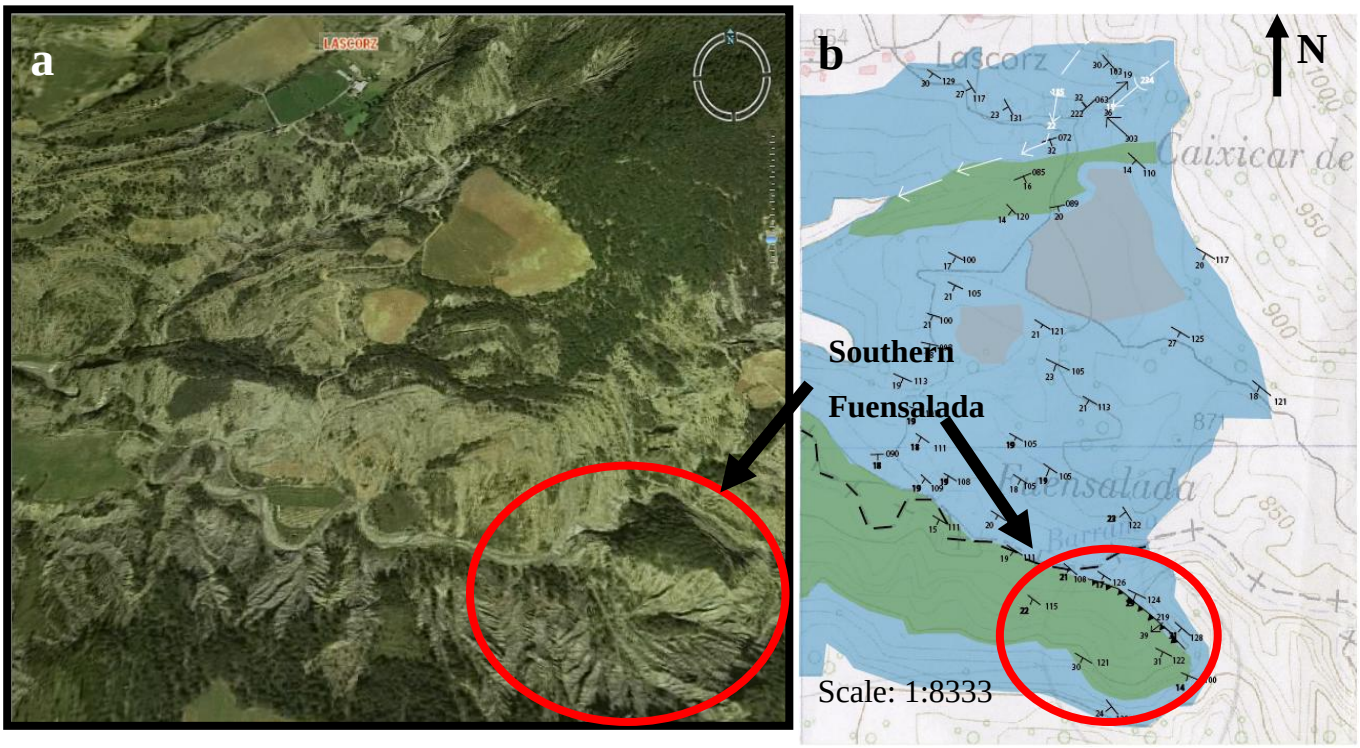

Figure 4.53: a) Aerial photo of Lascorz, where the Canyon at the southern Fuensalada is marked in red (from Aragon 3D, 2007). b) Geological map of Lascorz, and the same area is marked in the red circle.

The lower part of the ravine is highly fractured (figure 4.54), with two prominent fracture sets, namely one oriented sub-parallel to bedding and one cutting the bedding towards northeast with an average angle of 60^o. These fracture sets are denoted population L8 and L9 and are distinguished from each other by their orientation, while presence of calcite cement, mode and geometry are similar.

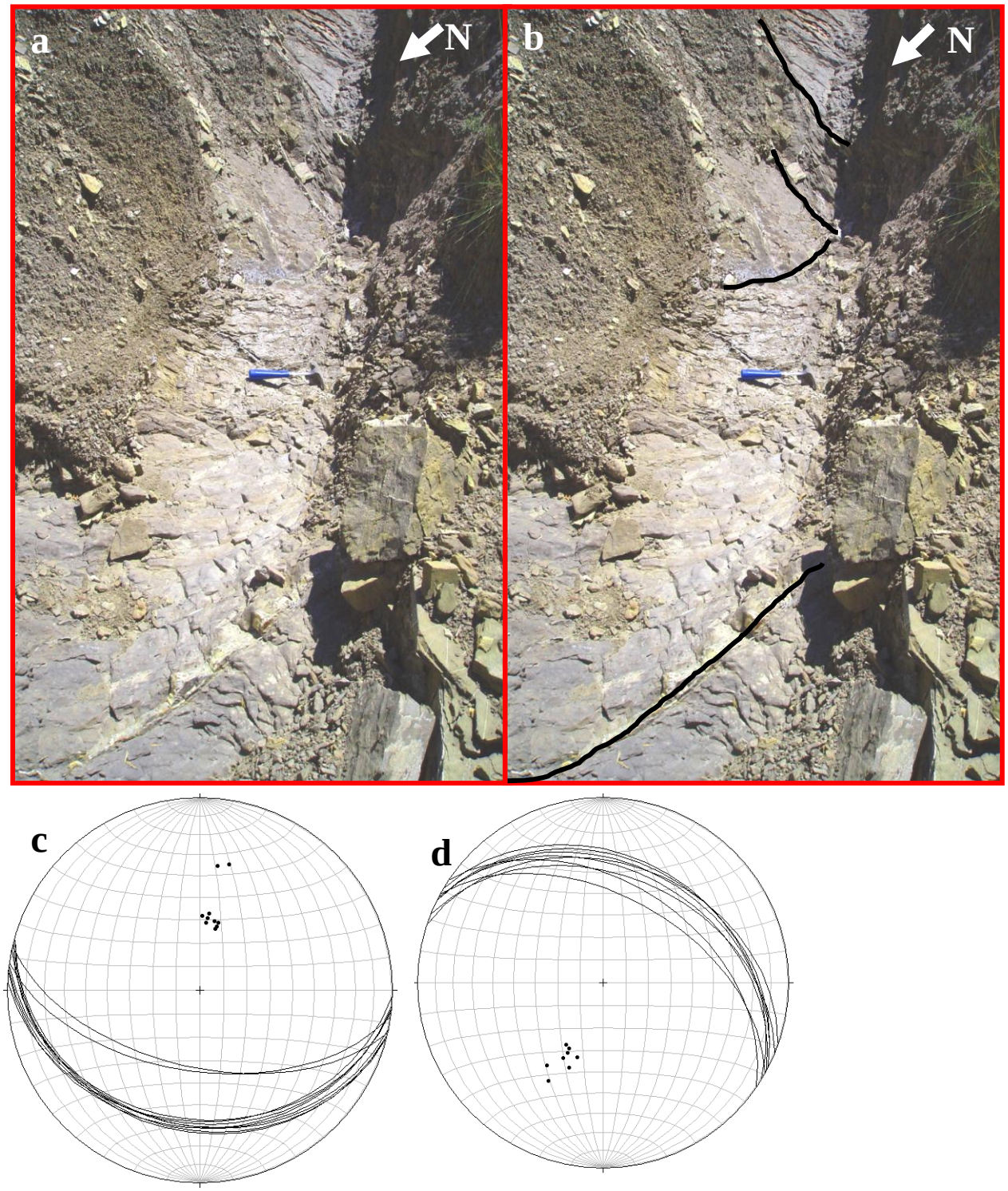

Figure 4.54: a) Population L8 fractures documented from the bottom of the ravine. Fractures marked in b. The fractures are seen both on bedding surface (blue lines) and sub-parallel to bedding (black lines). Notice hammer as scale. c) Measurements of strike and dip of population L8 fractures. d) Measurements of strike and dip of population L9 fractures. Note hammer as scale.

Population L8

Ten population L8 fractures were recorded from the mudstone in the bottom of the ravine. The fractures are sub-parallel to bedding, with an average length of minimum 3, 5 meters. The fractures are probably longer, but this cannot be documented due to limited exposure. All fractures contain calcite cement; they are closed and their average width is 34 millimeters (table 4.9). The average orientation is N100E and dips 33^{o} towards southwest.

Interpretation population L8

These are shear fractures, developed during tectonic compression of the rocks.

Population L9

Ten population L9 fractures were recorded from the mudstone in southern Fuensalada. Their average orientation is N296E and dips 34 ^{o} towards northeast. All fractures are straight and contain calcite cement. Their average length is 2, 5 meters, but, due to limitations regarding exposure, this can only be considered as their minimum length. The fractures are cutting the layer boundaries with an angle of approximately 60^{o}. All fractures are closed and have an average width is 45 millimeters (table 4.9).

Interpretation population L9

Population L9 fractures are shear fractures, developed during tectonic compression.

	Population L8	**Population L9**
Minimum length	3, 5 meters	2, 5 meters
Average width	34 mm	45 mm

Table 4.9: characteristics of population L8 and L9 fractures.

Chapter 5 – Discussions

Several geological models have been proposed for the formation and evolution of the Ainsa Basin and its related structures (figure 5.1) (e.g. Puigdefabregas & Souquet, 1986; Munoz, 1992; Travè et. al. 1998; Munoz et. al., 1998). In the light of the data collected and analyzed in the present work, the aim of the discussion chapter is to contribute the existing models and to construct an integrated structural model based on the data documented from the Ainsa Quarry, Las Uslas and Lascorz.

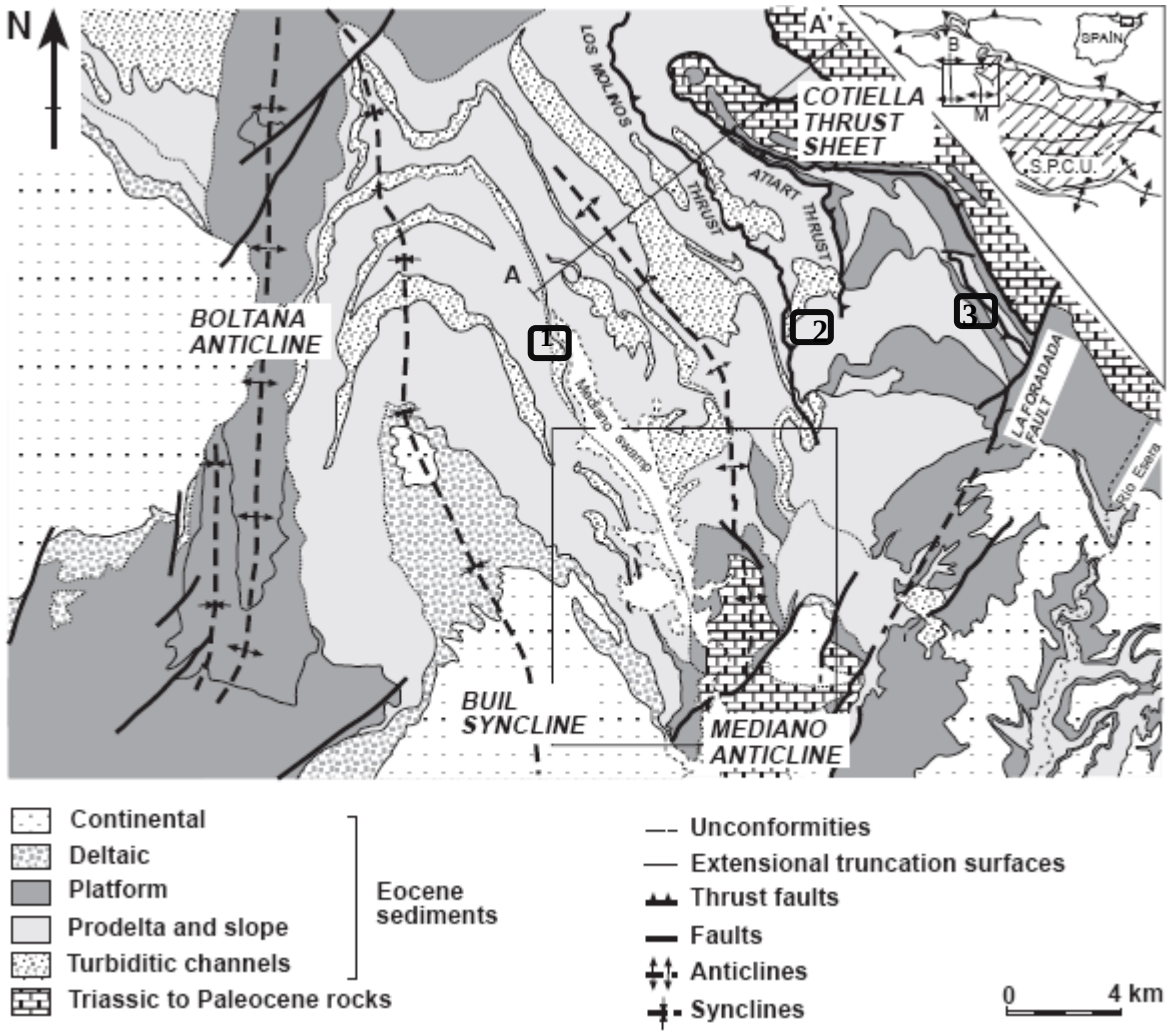

Figure 5.1: Ainsa Basin with its main structural elements. The localities described in chapter 4, Ainsa Quarry, Las Uslas and Lascorz, are marked in black squares, numbered 1, 2 and 3 respectively. Map from Munoz et. al., 1998)

The development of the Pyrenees involved collision between the Iberian plate with the Eurasia plate in late Cretaceous – Miocene time. The collision was rotational, with the first compression in the east, diminishing westwards (Warren, 1955; Choucroune & Seguret, 1973; Nijman, 1989; Sibuet et. al. 2004).

The thrust sheets in the southern Pyrenees have propagated southwards, with Boixols, Montsec and Sierras Marginales as the main thrusts related to the south central unit (Bentham et. al., 1992; Munoz et. al., 1992). The southern Pyrenees consisted of a foreland basin, which became separated into several minor piggy-back basins by thrusts that were oriented perpendicular and oblique relative to the main strike of the Pyrenean orogen (Choukroune & Seguret, 1973; Munoz, 1992; Munoz et. al., 1992). The Ainsa Basin is one such piggy-back basin. It encompasses the Mediano and Boltana anticlines and Buil syncline (figure 5.1), developed in Lutetian – Bartonian time. These are striking NNW - SSE, which is perpendicular to the main strike of the Pyrenean orogeny.

The Mediano anticline is situated within the greater study area, developed in Lutetian time. This is a 20 kilometer long and 9 kilometer wide anticline, interpreted to be a detachment fold (Travè et.al, 1998). The fold axis plunges towards north in the southern part, but rotates towards northwest, eight kilometers southeast of Ainsa town (figure 5.1). The fold is open and symmetric (Poblè et. al. 1998). To the northeast of Mediano anticline, Ainsa Basin is deformed by a thrust system with a top to southwest, represented by the Cotiella Nappe system (i.e. Cotiella, Atiart and Los Molinos thrusts) (Farrell et. al., 1987; McClay et. al. 1994; Munoz et. al., 1998). These thrusts represents a thrust-imbricate fan, related to the Peña Montanesa thrust (figure 5.2), and developed in Late Ypresian time (Poblè et.al., 1998; Travè et.al., 1998). According to Farrell et. al., (1987), several back-thrusts are observed in relation to the thrust imbricate fan, with a top to NNE. A left-stepping thrust system is documented, represented by the La Foradada tear fault, which is related to the Peña Montanesa thrust system (Atkinson et. al., 1987; Nijman, 1989). These thrusts are strike-slip faults with dextral displacement (figure 5.3), and are used as direct indicators for the rotational model of the compression associated to stress release along the La Foradada tear fault (Nijman 1989). The sole thrust related to the Mediano anticline is thought to be the

same sole thrust as the one the thrust imbricate fan branches out from in the study area (figure 5.2).

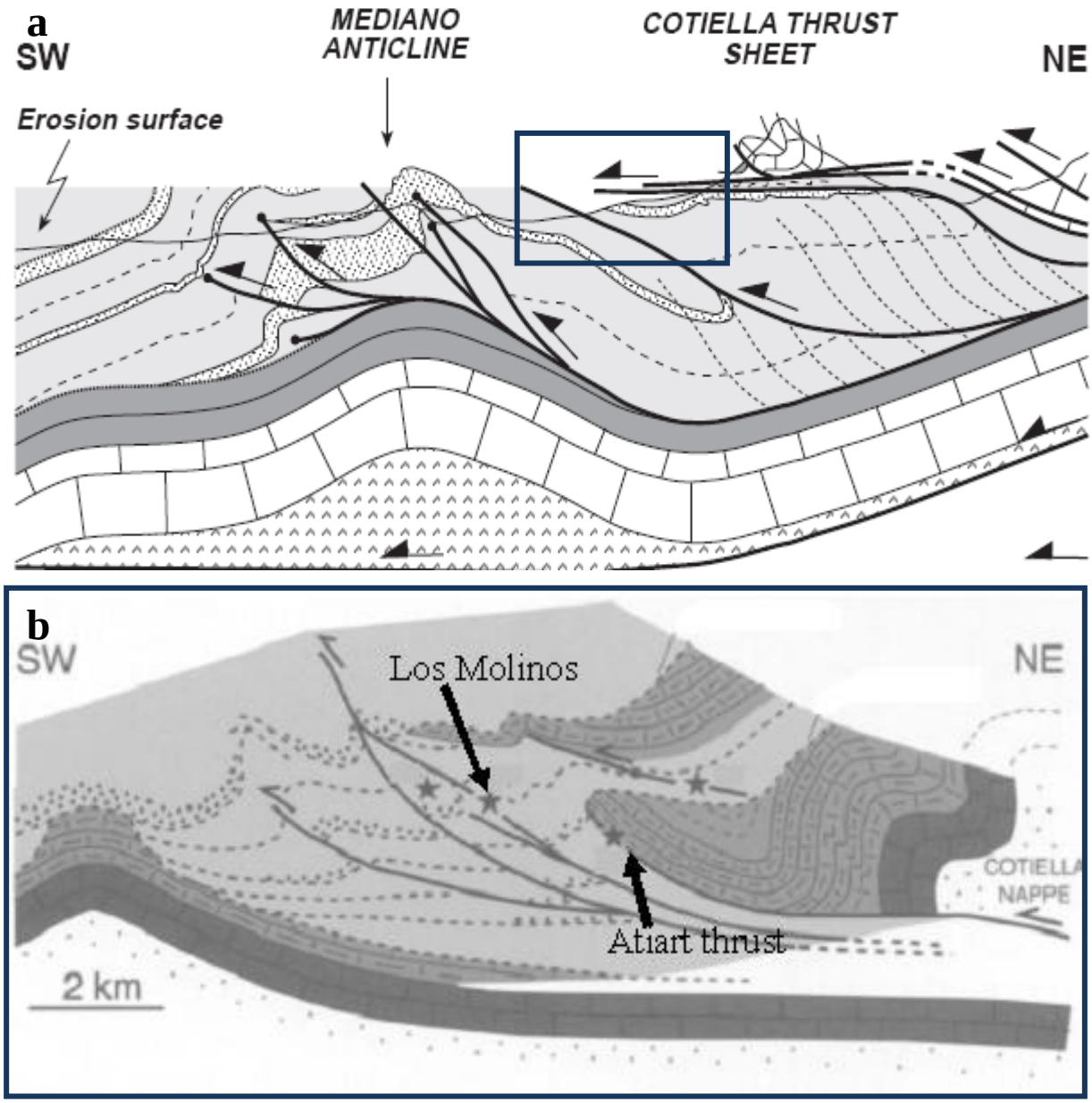

Figure 5.2: a) Cross-section of the northeastern Ainsa Basin (from Poblè et. al., 1998). b) Close up cross-section of the Cotiella thrust sheet (from Travè et. al. 1998). The cross-section in b is situated at the position of the blue square in a.

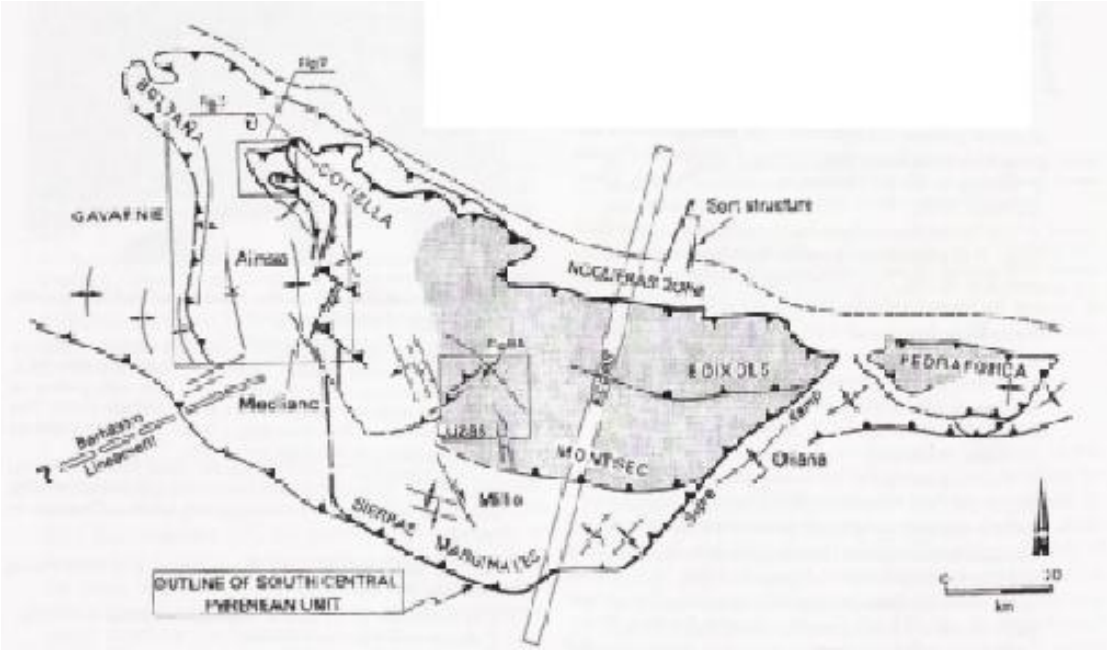

Figure 5.3: Structural elements in the south central Pyrenees. The left-stepping tear faults are seen just south of Cotiella thrust (figure from Nijman, 1989).

The structures documented in chapter 4 are discussed in the order of timing relative to each other. Syn-sedimentary faults are therefore discussed first, followed by fractures related to mechanical compaction, both through burial and uplift since these processes are similar, whereas fractures and folds related to tectonic contraction are discussed in the final part of this chapter.

5.1 - Syn-sedimentary faults

Configuration, architecture and mechanism typical for syn-sedimentary faulting are well documented in the literature (e.g. Bhattacharya & Davies, 2001; Bouroullec et.al. 2002; Marzo et. al., 2002; Hunt & Kosa, 2005). The syn-sedimentary faults documented at both Las Uslas and Caixicar de Pardina are found in strata interpreted to be related to a carbonate ramp, were the continent was located towards SSE and down-dip direction, towards the deepest part of the basin, was towards NNW (Puigdefabregas & Souquet, 1986; Woyessa, In Prep.). Three mechanisms are possible for initiation and development of the syn-sedimentary faults, namely

1) The development and evolution of the Mediano anticline (figure 5.4a)
2) Primary slope of the basin (figure 5.4b)
3) Development and evolution of Cotiella Nappe and A-3 (figure 5.4c)

Of the three hypotheses, the development of Mediano anticline is thought to be the most likely, because the syn-sedimentary faults are striking NW-SE, and dipping towards northeast. Since the Mediano anticline is located west of Las Uslas and central Caixicar de Pardina and plunges towards north (Poblè et. al, 1998), faults at both localities dip in opposite direction, i.e. away from its axial surface. This is as expected since syn-sedimentary faults dip towards the deepest part of the basin, whereas the Mediano anticline most like where a submarine high during faulting.

The carbonate ramp itself is not likely to have controlled the syn-sedimentary faults at Las Uslas and central Caixicar de Pardina, since its down-dip direction, and the deeper parts of the basin was towards northwest (Puigdefabregas & Souquet, 1986; Woyessa, In Press). This means that syn-sedimentary faults related to the ramp would be oriented towards southwest and dip towards northwest. The Cotiella Nappe thrust system and A-3 are not likely either, since both Las Uslas and central Caixicar de Pardina are located SSW of these structural features (figure 5.1). This means that syn-sedimentary faults, which were triggered as a consequence of displacement along these thrusts, would most likely be oriented towards southeast and dip towards southwest.

According to Puigdefabregas & Souquet (1986) and Woyessa (In Prep.), the carbonate ramp was active during early phase of development and evolution of Mediano anticline, in Lutetian - Bartonian time. According to Travè et. al. (1998), Cotiella Nappe, with its related back-thrusts, developed in Late Ypresian time, which is prior to accumulation on the carbonate ramp. Displacement along the Cotiella Nappe thrust and A-3 are therefore not likely to have triggered displacement along the syn-sedimentary faults since the rocks, were the faults are located, had not yet been deposited at the time of evolution of the thrust imbricate fan.

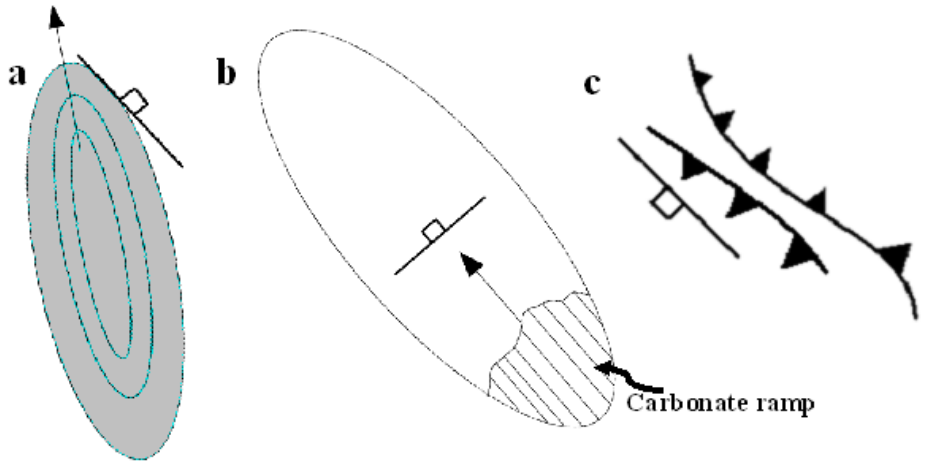

Figure 5.4: a) Mediano anticline would trigger syn-sedimentary faults towards northeast. b) Primary slope of the basin would trigger syn-sedimentary faults to dip towards northwest. c) Cotiella Nappe and A-3 would trigger syn-sedimentary faults towards southwest.

5.2 - Fractures related to burial and uplift

Several fracture populations related to burial and uplift were recorded from Ainsa Quarry and Lascorz during field work.

Fractures related to mechanical compaction in the Ainsa Quarry (chapter 4) are divided into four populations based on orientation and presence of calcite cement, since mode is the same in all populations (figure 5.5). Here, populations Q1, Q2 and Q3 are single-layer tensile fractures, distinguished from each other by their orientation. These three fracture sets have similar geometry, and are all cemented by calcite. Population Q4 is distinguished from population Q1, Q2 and Q3 by their orientation, lack of calcite cement and that they are multi-layer fractures.

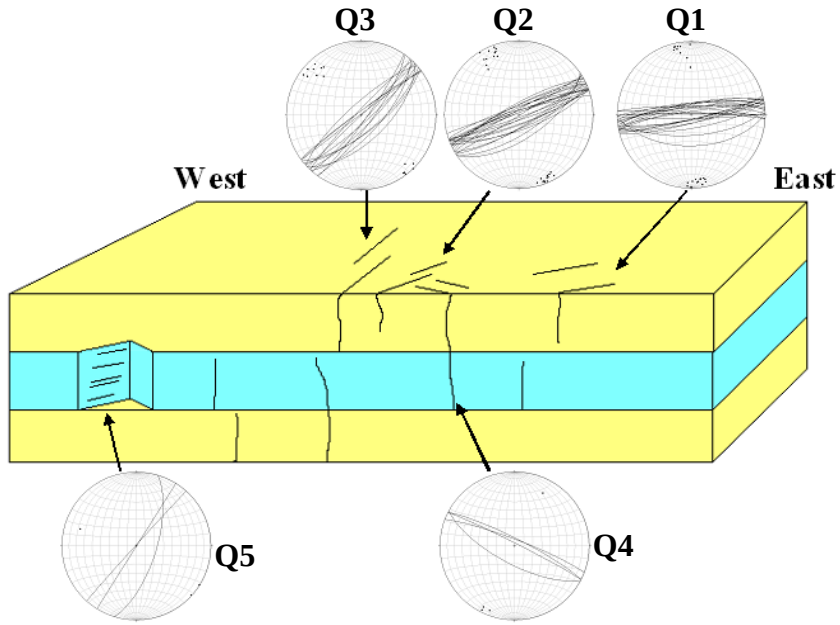

Figure 5.5: Illustration of the orientation of fracture systems in the Ainsa Quarry.

Three fracture populations related mechanical compaction were documented in the Lascorz area, distinguished from each other by orientation and architecture, whereas mode and lack of calcite cement is similar. These are the populations L3, L4 and L6, were all are tensile fractures, and L3 and L4 is an orthogonal fracture system.

5.2.1 – Fractures related to burial

Fractures related to burial are most often tensile (mode I) fractures in the upper part of the crust (e.g. Engelder, 1985; Maltman, 1988; Gabrielsen et.al, 1998). Such tensile fractures are vertical relative to bedding (S_0) and develop by vertical maximum stress axis,

$$\sigma_1 = \sigma_v = \rho g h,$$

where σ_1 is maximum stress axis, σ_v is vertical stress axis, ρ is density of the rock, g is gravity and h is overburden (e.g. Price & Cosgrove, 1990). Such fractures are also commonly often equally spaced, and the spacing appears to be related to layer thickness (Ladeira & Price, 1981; Bai & Pollard, 2000), and they are often restricted to one bed (i.e. single-layer fractures).

In the Ainsa Quarry, population Q1, Q2 and Q3 fits these criteria, and, accordingly most likely developed by a vertical σ_1. The difference in orientation is related to the orientation of minimum stress axis (σ_3), since the openings of tensile fractures are parallel to σ_3, indicating that the orientation of the minimum stress axis shifted by 20° during burial and evolution of the three populations (figure 5.6 and table 5.1).

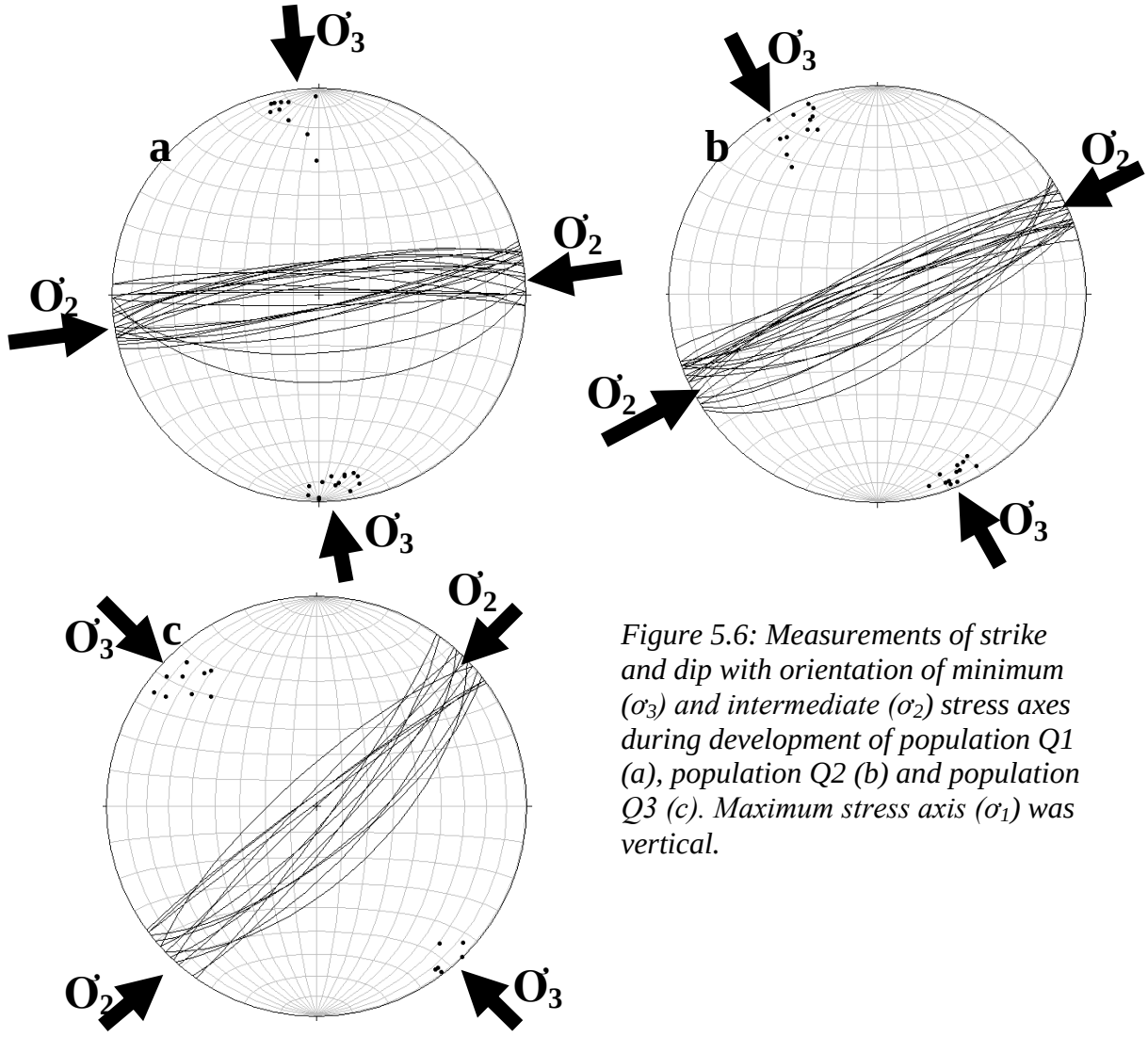

Figure 5.6: Measurements of strike and dip with orientation of minimum (σ_3) and intermediate (σ_2) stress axes during development of population Q1 (a), population Q2 (b) and population Q3 (c). Maximum stress axis (σ_1) was vertical.

Several studies have been published regarding orthogonal fracture patterns (e.g. Bahat, 1991; Ghosh, 1988; Dunne & North, 1990; Dunne & Hancock, 1994; Petit et. al., 1994; Aydin et. al, 2002). According to these authors, orthogonal fracture patterns tend to develop after a 90°

rotation of maximum ($\sigma_H = \sigma_2$) and minimum ($\sigma_h = \sigma_3$) horizontal stress axes, whereas maximum stress axis (σ_1) is vertical. The fractures are tensile, where each population has developed parallel to the $\dot{O}_H$.

In Lascorz, Population L3 and L4 at northern Fuensalada (described in chapter 4) represent an orthogonal fracture system, where the individual populations has the same characteristics as populations Q1-Q3 in Ainsa Quarry (e.g. mode, geometry). The fractures are tensile, and population L3 is oriented N200E whereas population L4 is oriented N290E. No offsets are observed, and the lengths of the population L3 fractures are controlled by the distance between individual population L4 fractures, which again is controlled by the distance between population L3 fractures.

This fracture system has developed during mechanical compaction, through burial, when maximum stress axis was vertical. The intermediate stress axis ($\dot{O}_2$) and the minimum stress axis ($\dot{O}_3$) were parallel and perpendicular to the strike of the fractures, respectively. The two fracture populations have thereby developed after a rotation of maximum horizontal stress axis ($\dot{O}_H = \dot{O}_2$). Population L3 developed while $\dot{O}_2$ was oriented NNE-SSW and $\dot{O}_3$ was oriented ESE-WNW (figure 6.16a), whereas population L4 developed while $\dot{O}_2$ and $\dot{O}_3$ were oriented ESE-WNW and NNE-SSW, respectively (figure 5.7 and table 5.1).

Population L3 fractures are NE-SW oriented, which is similar to population Q1-Q3 in Ainsa Quarry. Population L3 has therefore most probably developed in the same stress field as Q1-Q3. Population L4 fractures developed after a 90^o rotation of σ_2, a rotation which most probably was local since no fractures with similar orientation were observed in Ainsa Quarry, nor are there documented any orthogonal fracture systems in published literature from the study area.

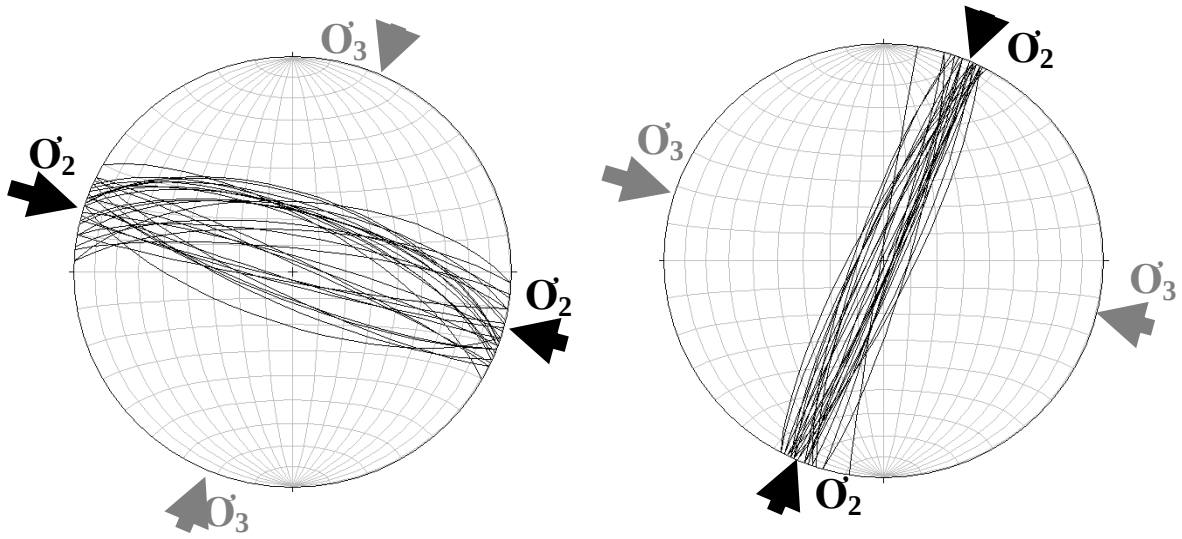

Figure 5.7: a) Stress regime during development of population L3. b) Stress regime during development of population L4. Average orientations of intermediate and minimum stress axes are seen in the tables below the stereonets. Maximum stress axis was vertical

	Strike (σ_2)	**Orientation of σ_3**	**Orientation of σ_1**
Population Q1	N265E	N175E – N355E	Vertical
Population Q2	N246E	N156E – N336E	Vertical
Population Q3	N229E	N139E – N319E	Vertical
Population L3	N020E – N200E	N110E – N290E	Vertical
Population L4	N110E – N290E	N020E – N200E	Vertical

Table 5.1: Orientation of the various fracture populations related to burial.

5.2.2 – Fractures related to uplift

Fractures related to uplift are difficult to distinguish from fractures related to burial (e.g. Engelder, 1985; Bahat, 1991; Bahat, 1999). According to these authors, fractures related to uplift are often multi-layer fractures, crossing layer boundaries. They also seem to be less systematic with wider spacing between individual fractures, compared to fractures related to

burial. The key difference between stress regime during development of fractures related to uplift and fractures related to burial is the decreasing difference in magnitude between maximum and minimum stresses. Maximum stress axis is vertical also during uplift, but its magnitude decreases compared to minimum stress axis as a function of decreasing overburden (i.e. erosion).

$$\frac{\sigma 1}{\sigma 3} \rightarrow 1$$

As described in chapter 4, population Q4 at Ainsa Quarry and L6 at Lascorz share the same characteristics (e.g. orientation, mode, fracture frequency) and are therefore considered to belong to the same fracture system. These fractures are crossing layer boundaries, the spacing between the fractures is wider than what is observed for populations Q1 – Q3 and L1 - L2, and they contain no calcite cement. The lack of calcite may be taken as an indication that the initiation of the fractures occurred after populations Q1 – Q3. The stress regime during development of the fractures was similar to population Q1, Q2 and Q3, with maximum stress axis (σ_1) vertical, whereas minimum stress axis (σ_3) was NE-SW (figure 5.8). Population Q4 and L6 fractures are therefore interpreted to have developed as a consequence of contraction of the rocks while unloading during uplift.

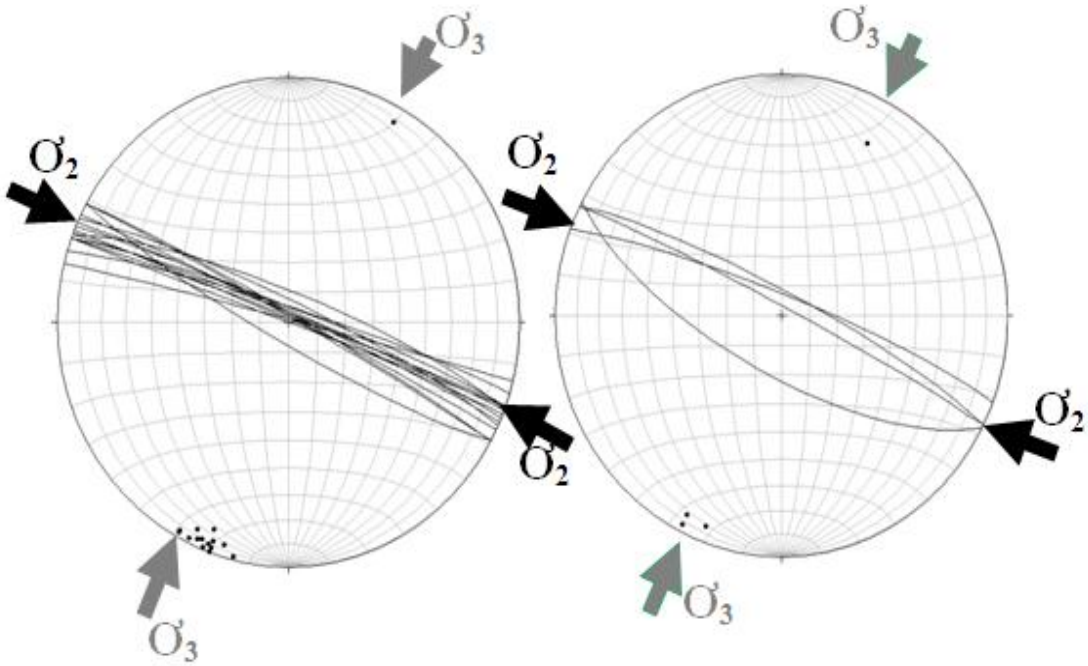

Figure 5.8: Measurements of strike and dip of population Q4 (a) and L6 (b). σ_1 is was vertical at the time of development.

5.3 – Development of the folds

5.3.1 - Fold mechanism

Based on the observations described in chapter 5, together with published literature, three hypotheses are possible for the development and evolution of the folds documented in the study area, and particularly fold A-3; namely:

1) The first model describes A-3 as a detachment fold (figure 5.9a; Poblè et. al., 1998).
2) The second model relates to a fault propagation fold (figure 5.9b; Moores & Twiss, 1992; Tavani et. al., 2006),
3) The third model relates to a fault-bend fold (figure 5.9c; Rich, 1934; Johnson & Berger, 1989; Moores & Twiss, 1992).

Detachment folds are characterized by rotation of the back limb along-strike during evolution, with simultaneously change of dip. Fault-propagation folds are characterized by constant dip of the back limb, and they often become overturned. Fault-bend folds are characterized by planar fold-limbs and are rarely overturned (see section 1.4 for more detailed description of these three fold-mechanisms). As previously mentioned, the Mediano anticline and the Cotiella Nappe formation are the main regional structures in the northeastern Ainsa Basin. The Mediano anticline is a detachment fold (Poblè et. al., 1998), a hypothesis based on the increase in dip southward along strike of the fold. The Cotiella Nappe formation is a thrust imbricate fan related to the Peña Montanesa thrust, with related back-thrusts (Farrell et. al., 1987; Mutti et. al., 1988; Travè et. al., 1998), a hypothesis which is mainly based on data collected from outcrops of the thrusts.

Based on field data and observations from aerial photos, A-3 is a fault-propagation fold, evolved on a back-thrust related to the thrust imbricate fan as described by Farrell et.al. (1987) and Travè et. al., 1998). This is based on the observed constant dip (i.e. 19^{o} towards

southwest) as in the Lascorz area, where neither of the fold limbs changes along strike. Aerial photos of the fold indicate a much steeper northeastern side of the fold axis, together with similar orientation of the bedding as the bedding recorded from the southwestern side of A-3 (figure 5.10). This indicates that A-3 is overturned on its northeastern limb. A-3 is therefore thought to be a fault-propagation fold, associated with top-to northeast displacement. Fault-propagation folds with similar orientation are documented from the north eastern Ainsa Basin in the literature (Farrell et. al., 1987; Travè et. al., 1998; Ako, in prep.)

A detachment fold mechanism is not likely since the kinematics of detachment folds often results in different dip-angles on the back limb at different localities along the fold (Poblè et.al., 1998). This is not observed along A-3, and no indication for this is observed in aerial photos. Furthermore, a fault-bend mechanism requires that the bedding on the northeastern side of A-3 should have been horizontal; alternatively dipping towards northeast, since fault-bend folds rarely appear as overturned folds (Johnson & Berger, 1989).

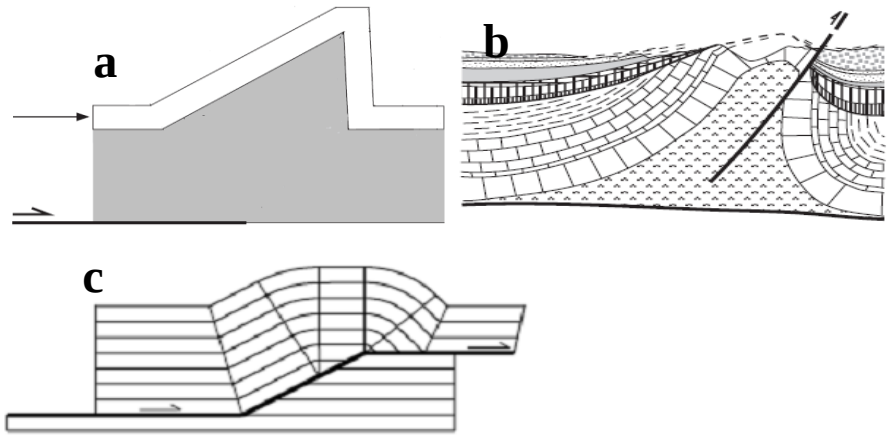

Figure 5.9: a) Detachment fold (figure from Poblè et. al., 1998). b) Fault-propagation fold (figure from Poblè et. al., 1989). c) Fault-bend fold (figure from Tavani et. al., 2004).

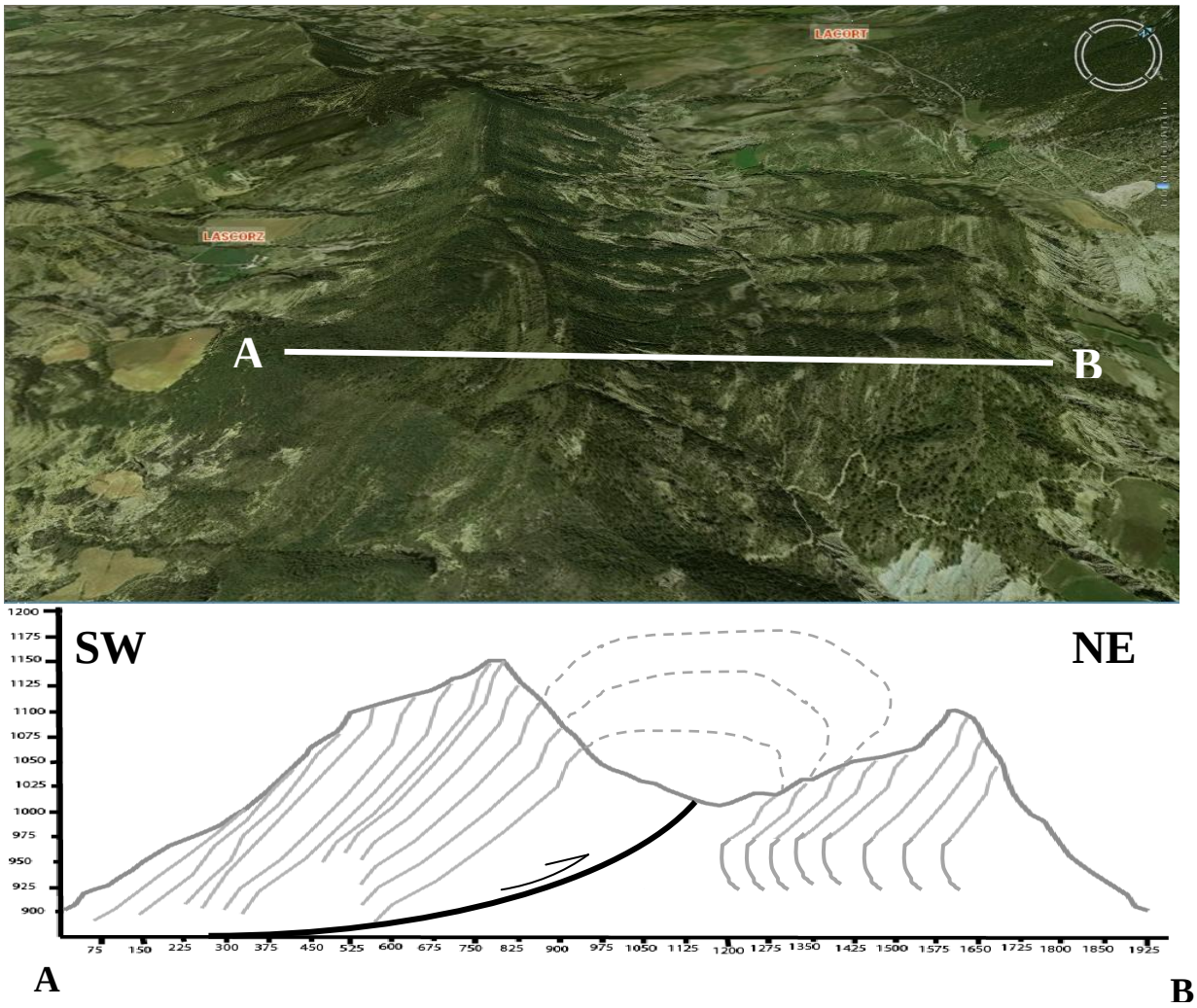

Figure 5.10: The character of each side of the fold axis is very different, indicating a steeper limb on the northeastern side of the fold axis, together with bedding dipping towards southwest. The cross-section is between A – B. From Aragon 3D (2007).

5.3.2 – Strain markers in contractional areas and determination of stress

As documented in chapter 4, two fold trends where observed in the Lascorz area. These are crossing folds, where A-1 is oriented NNE-SSW, parallel with Mediano anticline, and A-3 is oriented NW-SE, parallel with the Cotiella Nappe system. A-1 is an open fold and has an amplitude and wavelength of 50 meters and 300 meters, respectively. On its eastern limb, A-2 is observed, documented as a minor fold with similar orientation (described in chapter 4). A-2 is interpreted as a parasite fold, which is gently open and has an amplitude of two meters and a wavelength of three meters. A-3 is an open fold with amplitude of 600 meters and wavelength of 3, 5 kilometers (figure 5.11).

Two populations of bedding surface (S_0) lineation (described in section 1.4) is documented from the upper surface of calcareous sandstone beds at central Caixicar de Pardina (described in chapter 4). These display bedding – parallel displacement, where one of the populations is perpendicular to the fold axes of A-1 and A-2, whereas the second population strikes perpendicular relative to the fold axis of A-3. Such lineations are often observed in buckle folds (buckle folding described in section 1.4), which indicate bedding parallel displacement perpendicular to the fold axis (5.12; buckle folding described in section 1.4) (e.g. Davis, 1984).

According to Alsop et. al. (1996), double folding is typical in areas where a contractional deformation has been overprinted by another and where the new maximum stress ($\sigma_1 = \sigma_{H,max}$) deviates significantly (more than 30^o) from the previous. A-1 and A-3 represent two distinct fold events, were A-3 is a back-thrust related to the thrust imbricate fan developed while maximum stress axis was oriented NE-SW and A-1 and A-2 is related to the same stress field as Mediano anticline, developed while maximum stress axis was oriented ESE-WNW (figure 5.12).

According to Poblè et. al. (1998), Mediano anticline developed in Lutetian time, whereas the main displacement along the thrust imbricate fan is Ypresian of age. Since the orientation of A-3 is similar to the thrusts related to the Cotiella Nappe formation (i.e. Cotiella, Los Molinos and Atiart), these have developed in the same stress field at the same time period. Folds A-1 and A-2 have similar orientation as the Mediano anticline, indicating development in the same stress field and at the same time period. A-3 did thereby develop in Late Ypresian time, prior to A-1 and A-2 which developed in Lutetian time.

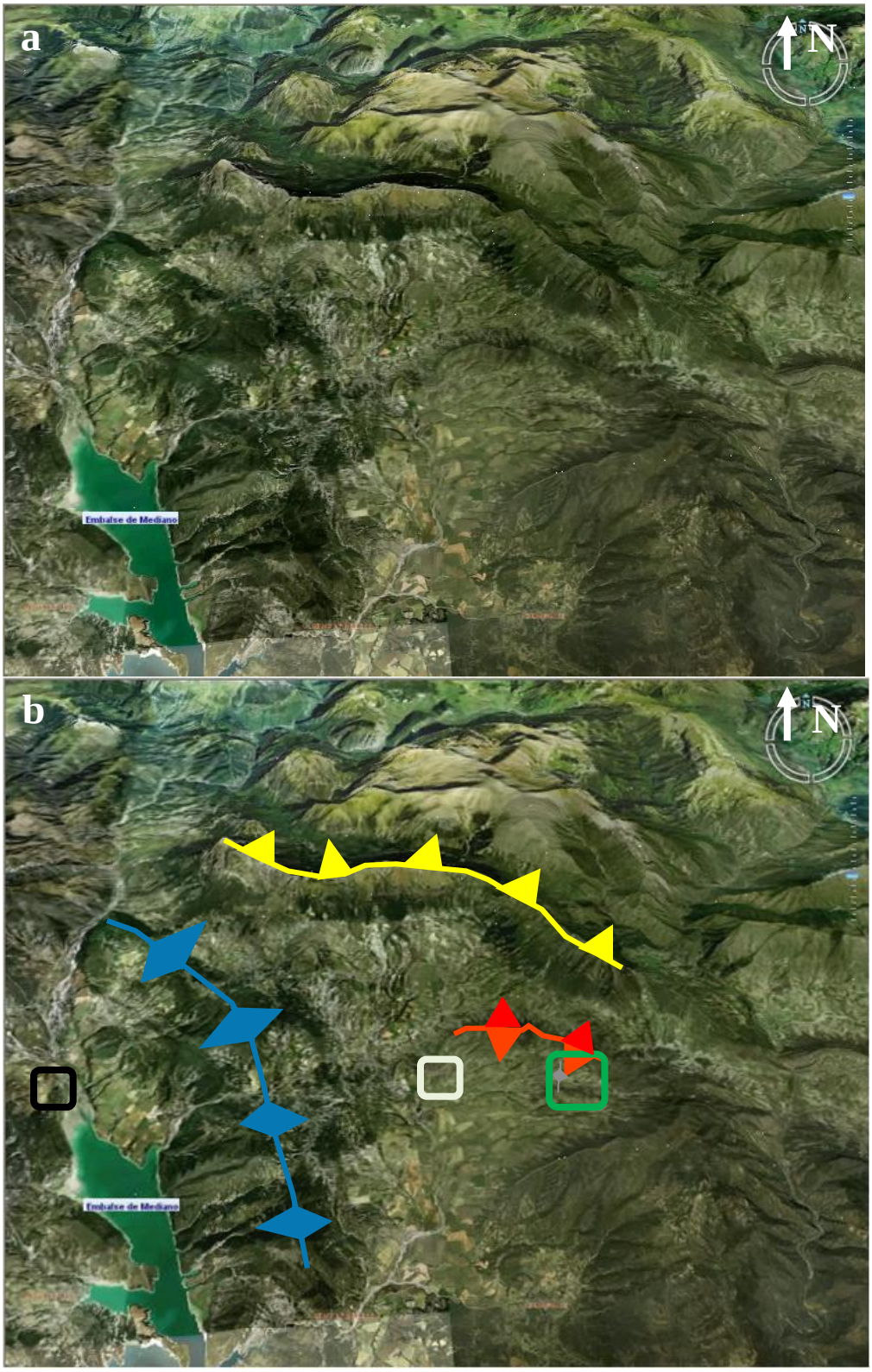

Figure 5.11: a) Overview of northeastern Ainsa Basin. b) Same as a, with Cotiella thrust (yellow), Mediano anticline (blue) and A-3 (red) marked. Ainsa Quarry, Las Uslas and Lascorz are marked in black, white and green squares, respectively. (The aerial photos are from Aragon 3D, 2007).

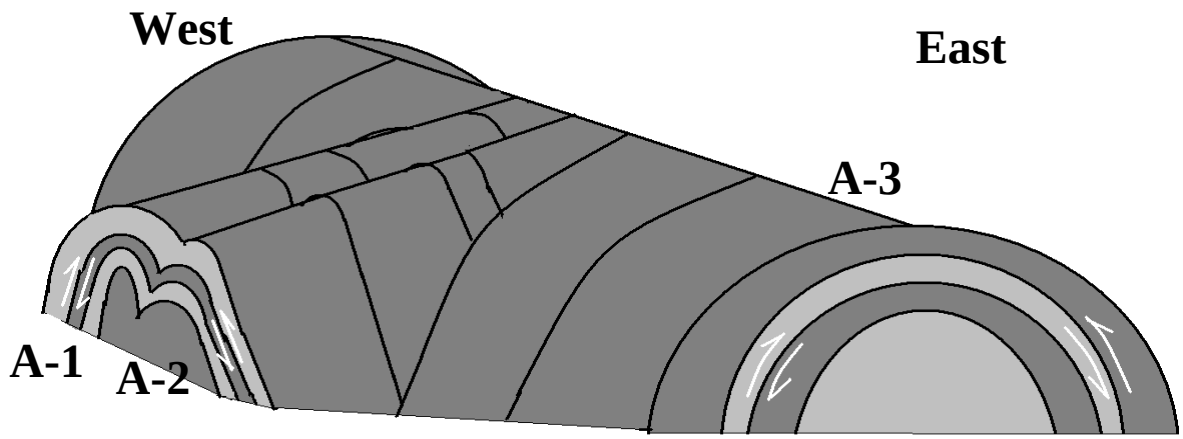

Figure 5.12: Orientation of the three folds relative to each other. Same figure as figure 4.25.

5.3.3 - Fractures related to folding

The folds documented from the Lascorz area are buckle folds with displacement parallel to bedding and parallel to the fold axes (figure 5.12). Four fracture populations were observed in the field, related to tectonic contraction (i.e. L1, L2, L5 and L7) (figure 5.13).

There are two fold populations recorded in the study area, were A-1 and A-2 is oriented NE-SW, whereas A-3 is oriented NW-SE (figure 5.14).

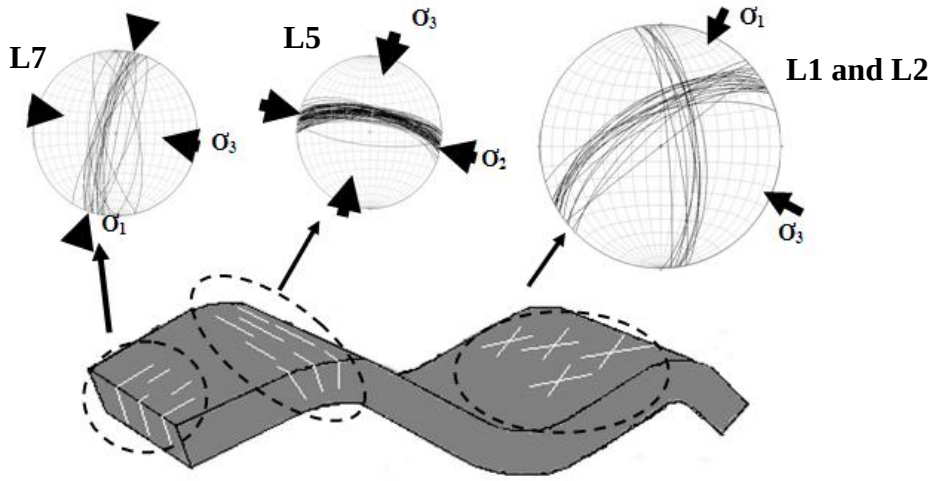

Figure 5.13: Fractures interpreted to be genetically related to the development of A-3.

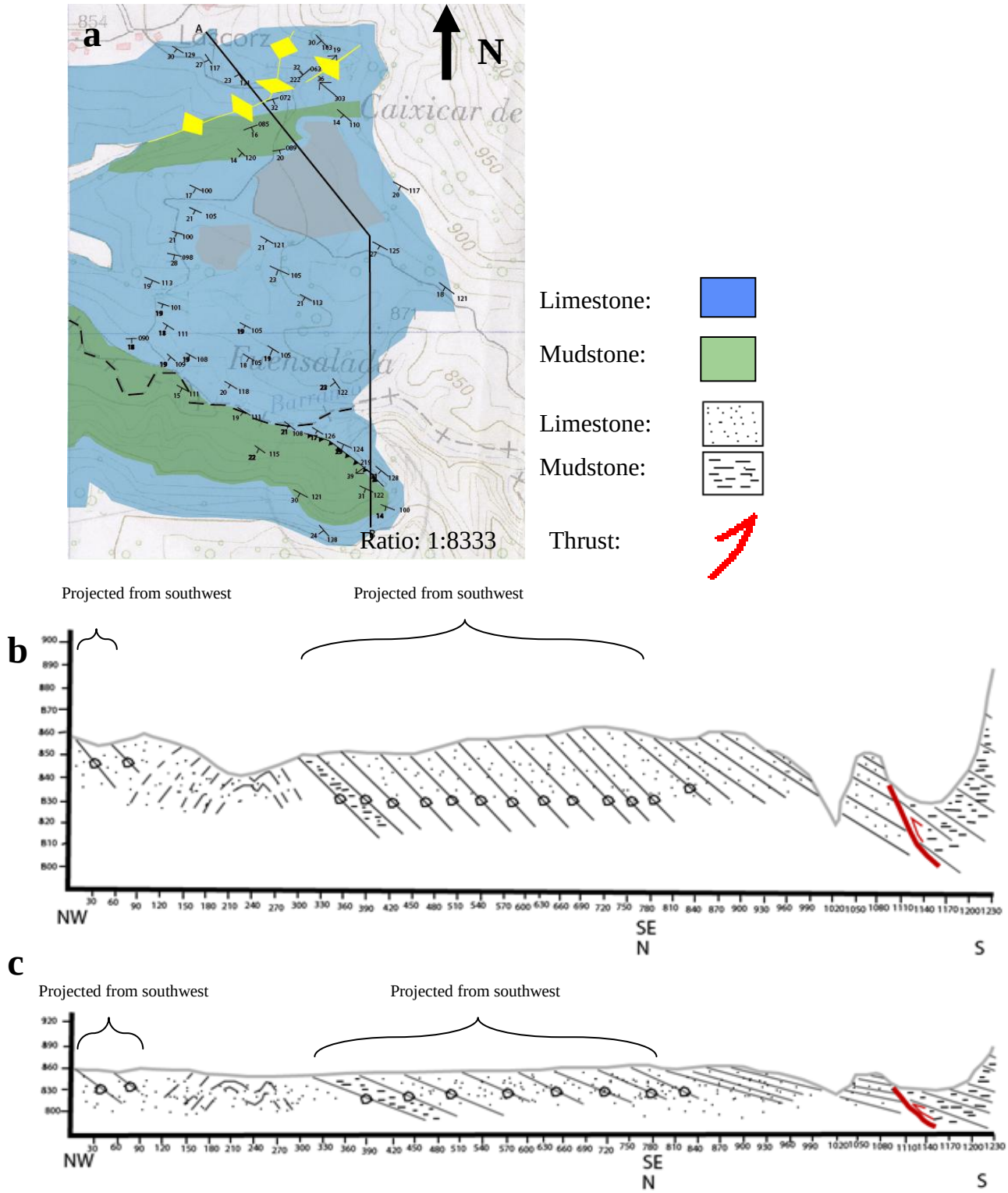

Figure 5.14: a) Map of Lascorz with cross-section between A-B in b and c. The two cross-sections have different scale, were b has 1:3, whereas c has 1:1. Bedding planes with circle illustrate dip towards the reader.

Population L5

As documented in chapter 5, population L5 fractures consist of tensile fractures with an average strike NW - SE (N285E), which is close to parallel with the axial surface of A-3. The fractures are also regularly distributed, with equal distance between the individual fractures, together with a vertical dip relative to bedding. They are also cutting population L8 fractures, indicating a later development. From these observations, population L5 fractures are interpreted as axial surface cleavage. Since the area is subjected to tectonic contraction, maximum regional stress axis (σ_1) was oriented perpendicular to the strike of the fractures, i.e. NE-SW, whereas intermediate stress axis (σ_2) and Minimum stress axis (σ_3) was parallel with the strike of the fractures and vertical, respectively. Locally, the stress field must have been different since tensile fractures strikes perpendicular to minimum stress axis. The intermediate stress axis (σ_2) was oriented parallel with the fractures, and σ_3 and σ_1 were oriented perpendicular to the fractures and vertical, respectively (figure 5.15).

Several studies have been published regarding this type of fracture system (e.g. Ramsay, 1967; Stearns, 1964). According to these authors, axial surface cleavage strikes parallel to the axial surface and dip perpendicular relative to the bedding in buckle folds. The cleavage is tensile fractures, and has a systematic fracture system with more or less equal spacing between individual fractures. The fractures develop after an increase in the curvature of the beds. Then, considerable reduction of the compressive stress will take place in the upper parts of the beds, so that, locally, σ_3 acts parallel to the main compressive direction. σ_1 is then, locally, vertical, whereas σ_2 is parallel with the strike of the fractures (e.g. Price & Cosgrove, 1990).

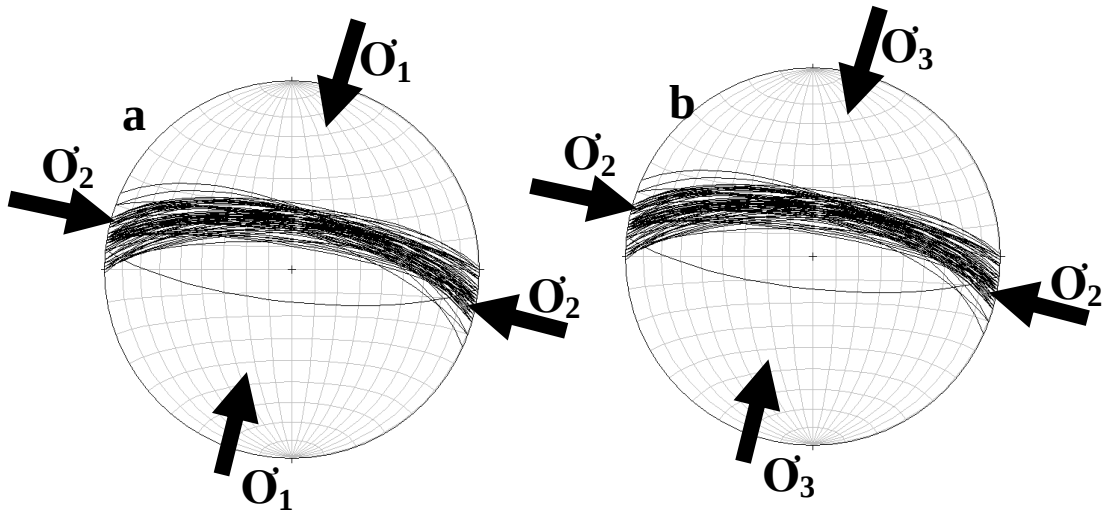

Figure 5.15: a) Regionally.σ_1 was perpendicular to the strike of the fractures during development, whereas σ_2 was parallel to the strike. $\dot{O}_3$ was vertical. b) Locally. $\dot{O}_3$ was perpendicular to the strike of the fractures during development, whereas σ_2 was parallel to the strike of the fractures. $\dot{O}_1$ was vertical.

Population L7

Population L7 fractures, described in chapter five, have an average orientation of N200E and close to vertical dip relative to bedding. This population is thereby oriented perpendicular relative to A-3. The fractures are tensile, with equal spacing between individual fractures (approximately 1, 5 meters, table X in appendix II). The fractures are also documented to pre-date the axial surface foliation (i.e. population L5). The perpendicular orientation relative to A-3 indicate that the fractures are striking approximately parallel with the maximum regional stress axis ($\dot{O}_1 = \dot{O}_{H,maks}$) during development of A-3 (i.e. N029E - N209E), which then also represent $\dot{O}_1$ during development of population L8. Intermediate stress axis ($\dot{O}_2$) was vertical during evolution of the fractures, whereas minimum stress axis ($\dot{O}_3$) was parallel to the direction of opening (i.e. N110E – N290E) (figure 5.16). Regionally, σ_3 was vertical and σ_2 was oriented N110-N290E.

Since population L7 fractures are cut by population L5 fractures, these fractures must have developed earlier than the L5 fracture set.

Fracture systems oriented parallel with σ_1 during folding is described in the literature (e.g. Hancock, 1985; Bergbauer & Pollard, 2004; Bellahsen et. al., 2006). The fractures are,

according to these authors, often systematically distributed, with more or less equal spacing between individual fractures. This fracture system develops when $\dot{O}_2$ is vertical and the fluid pressure approaches, or just exceeds, the vertical pressure (Cosgrove & Price, 1990). They strike parallel with maximum stress axis during folding and are often observed to pre-date axial-plane foliation.

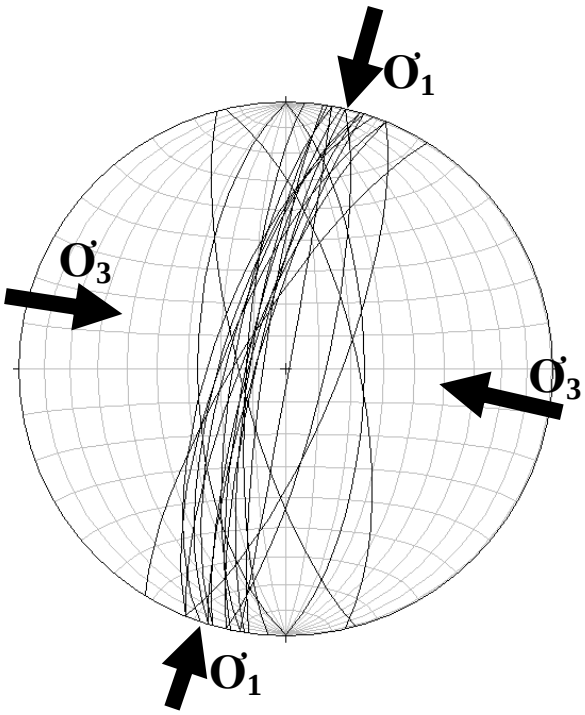

Figure 5.16: Maximum stress axis is parallel with the strike of the fractures, whereas intermediate stress axis is perpendicular to the strike. Since the fractures are developed in a compressional regime, minimum stress axis is vertical.

Population L1 and L2

Both population L1 and L2 consists of strike-slip fractures (figure 5.17) (described in chapter 4). When comparing these fracture sets to the folds documented from the Lascorz area, genetic relationships are observed. The orientations of populations L1 and L2 are N237E and N351E respectively, while the fold axis of A-3 is oriented N299E. Both fracture sets are thereby oriented approximately 30^o away from the maximum stress axis (σ_1) during development of A-3 (i.e. N209E – N029E). Locally, both populations have developed while maximum stress axis ($\dot{O}_1 = \dot{O}_{H,max}$) was perpendicular relative to the axial surface of A-3, i.e. NE-SW, minimum stress axis ($\dot{O}_3$) was parallel with the fold axis of A-3, i.e. NW-SE, and intermediate stress axis ($\dot{O}_2$) was vertical (figure 5.17). This is slightly different from the regional stress field, were σ_2 and σ_3 , were oriented NW-SE and vertical, respectively.

Since population L1 and L2 fractures cuts population L5 fractures, these developed at a later stage of folding compared to population L5 fractures. They therefore also developed at a later stage then population L7 fractures, since these were observed to be cut by population L5 fractures.

This type of fracture pattern was first documented by Anderson (1951), and further described by e.g. Stearns (1964); Price & Cosgrove (1990); Pollard & Olson (1991); Bellahsen et. al. (2006). This fracture pattern is described as strike-slip fractures obliquely oriented relative to its related fold axis. It develops when fluid pressure is not quite high enough to cause hydraulic fractures, simultaneously with a maximum stress axis (σ_1) perpendicular to the fold axis. The σ_1 has also been sufficiently high so that $(\sigma_1 - \sigma_3) > 4T$, where T is the tensile strength of the rock (e.g. Price & Cosgrove, 1990).

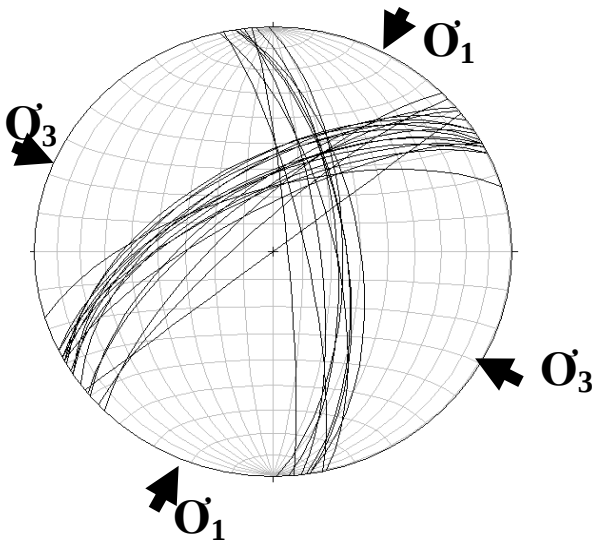

Figure 5.17: Stress field during development of populations L1 and L2.

In Ainsa Quarry, fracture population Q5 strike N223E, with a strike-slip displacement along the fractures, and are thereby oriented sub-parallel with population L1. During displacement, maximum stress axis ($\sigma_1 = \sigma_{H,max}$) must have been obliquely, approximately 30^o, relative to the strike of the fractures (figure 6.12) (e.g. Price & Cosgrove, 1990). Minimum stress axis (σ_3) was 90^o relative to maximum stress axis (i.e. NNW-SSE), whereas intermediate stress axis (σ_2) was vertical.

Since the fractures are parallel with population L1, together with the same mode, these fractures may have developed within the same stress field as the conjugate shear fractures at Lascorz. But, since only one population was observed, the maximum stress axis may also have been oriented NE – SW (figure 5.18).

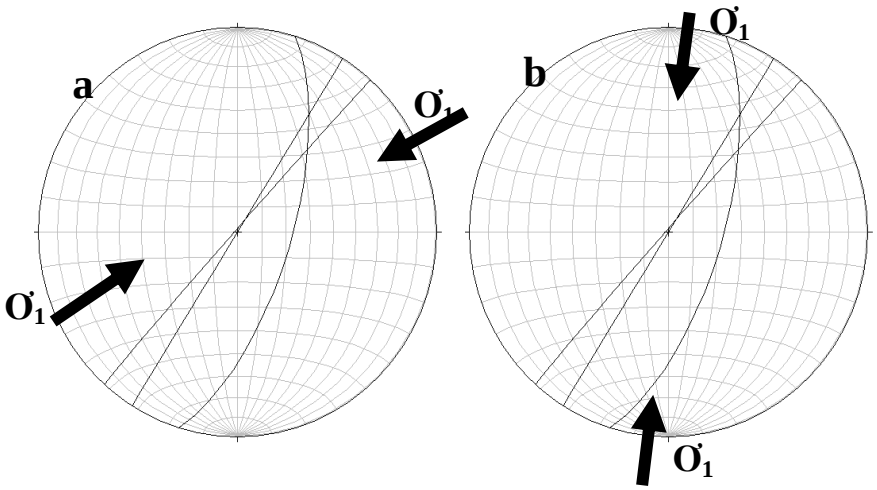

Figure 5.18: Since strike-slip fractures are oriented 30^o on the maximum stress axis (σ_1), σ_1 may have been oriented either NNE-SSW (a) or ENE-WSW (b).

5.4 - Fractures related to a fault zone

Fault zones are characterized by closely spaced joints and shear fractures (e.g. Davis & Reynolds, 1996). They are often associated with conjugate shear fractures, of where their line of intersection is parallel with the intermediate stress axis (conjugate shear fractures and fault zones described in more in detail in section 1.4).

In the study area, populations L8 and L9, documented from the southern Fuensalada (described in chapter 4), are shear fractures sub-oriented parallel, in a NW-SE direction. Population L8 are sub-parallel to the bedding (S_0), dipping in average 33^o towards southwest, whereas population L9 is dipping obliquely relative to the dip of the bedding (S_0), 34^o towards northeast. These are conjugate shear fractures related to a fault zone, where the individual populations dip 67^o from each other.

The conjugate shear fractures are used to discuss direction of displacement along the fault, and thereby also type of fault, which can be either;

1) a thrust,
2) a normal fault, or
3) a strike slip fault

Since the study area is located in an area, subjected for tectonic contraction, none normal faults (except syn-sedimentary faults) have been documented from the area in published literature. As discussed in section 6.2.1, A-3 is a fault-propagation fold related to a thrust with top to northeast, whereas the Cotiella Nappe system has a top to southwest (Poblè et. al., 1998). The La Foradada fault is a strike-slip tear fault related to the Peña Montanesa thrust, and is oriented N-S.

Of these three types of faults, the conjugate shear fractures in southern Fuensalada are thought to be related to a thrust with top to northeast. This is based on the orientations and dips of the fractures, together with a distance view of the fault plane (figure 5.19). As stated above, population L8 and L9 are oriented sub-parallel to each other, while their angles of dip are 67^{o} from each other. This indicates that the intersection plane between the fractures, and thereby also orientation of intermediate stress axis (σ_2), is parallel to the strike of the fractures, i.e. WNW - ESE. The maximum stress axis (σ_1) was oriented approximately 30^{o} to the angles of dip of both fracture populations and perpendicular relative to the intermediate stress axis. Populations L8 and L9 dips towards SSW and NNE, respectively, which is parallel to the σ_1 at the time of development. Minimum stress axis (σ_3) was vertical at the time of development (figure 5.20). This stress field reflects the regional stress field during development of the Pyrenean orogeny.

The conjugate shear fractures are not likely to be related to a strike slip fault similar to La Foradada, due to the orientation of the intersection plane between the two fracture populations. This would then be oriented vertically.

The thrust is not likely to have a top to southwest due to the direction of dip of the fault plane seen in figure 5.19. If the thrust had a top to southwest, the fault plane in figure 4.19 would dip in the opposite direction.

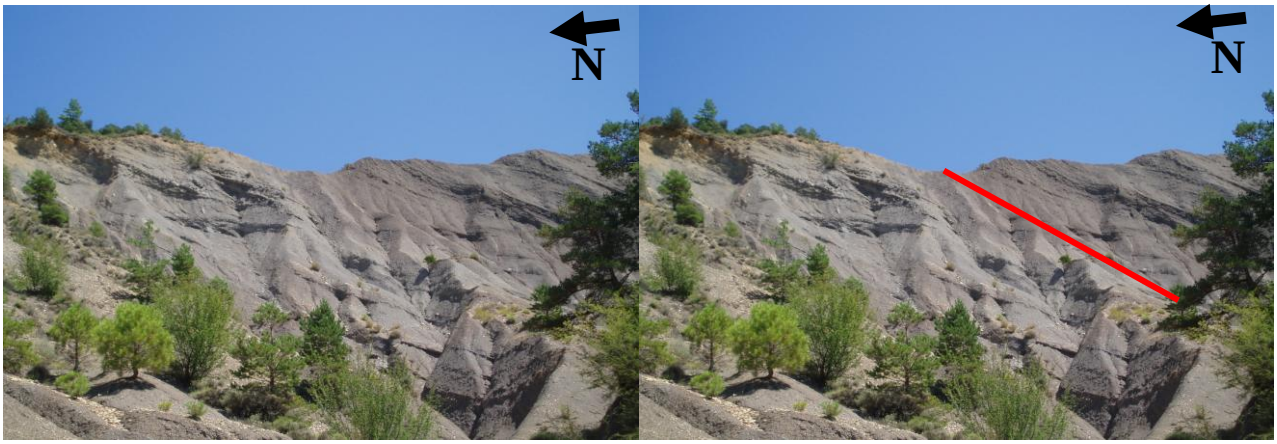

Figure 5.19: The red line illustrates where the fault is located on the picture to the right.

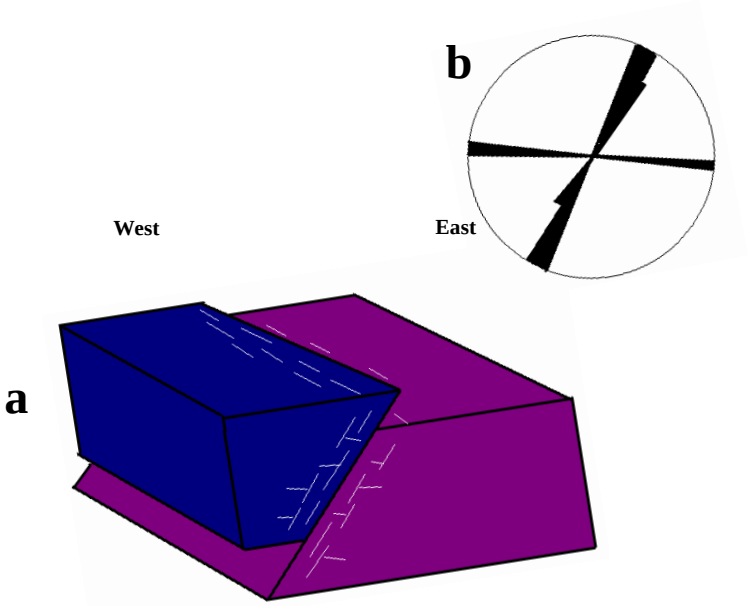

Figure 5.20: a) Orientation of the reverse fault with the conjugate shear fractures illustrated in the fault zone. b) Dip directions of the two populations. σ_1 is oriented NE-SW, σ_2 is oriented NW-SE, whereas σ_3 is vertical.

Chapter 6 – Conclusion

The main objective of this work is to study the structural development of the Ainsa area, starting with syn-sedimentary faults analysis, followed fractures related to burial and uplift and the structures affiliated with contraction.

Displacement along the syn-sedimentary faults at Las Uslas and Caixicar de Pardina were activated by the growth of Mediano anticline. The Mediano anticline was at the time of faulting probably a submarine high located to the WSW of the faults, whereas the deepest part of the basin was towards northeast. These structures developed during accommodation of sediments, prior to tectonic contraction of the same rock (table 7.1)

The fractures related to mechanical compaction at Ainsa Quarry and Lascorz, developed as a consequence of burial, while tectonic contraction was trivial. Since the minimum (σ_3) and intermediate (σ_2) stress axes are similar in magnitude, these have, as observed by the various populations in Ainsa Quarry, shifted during burial. The fractures related to uplift developed in the same regional stress field as those related to burial, with maximum stress axis vertical.

The fold A-3 is a fault propagation fold, were the related thrust has a top to northeast. A-3 is associated with a well developed fracture system, represented by axial plane cleavage, tensile fractures striking parallel with σ_1 during folding and conjugate shear fractures striking 60^o from each other and 30^o from the σ_1 during development of A-3.

The conjugate shear fractures at southern Fuensalada are related to a thrust with top to northeast, parallel oriented relative to A-3.

A-1, and its parasite fold, A-2, is positioned on the southwestern limb of A-3 and oriented obliquely relative to it. The folds developed while maximum stress axis was oriented WNW-ESE.

The orientation of A-3 and the thrust documented from the southern Fuensalada corresponds well with the back thrusts related to the Cotiella Nappe system, described by Farrell et. al. (1987), Nijman (1989) and Travè et. al. (1998). Both structures have thereby developed in Ypresian time, while maximum stress axis was oriented NE-SW.

The orientations of A-1 and A-2 corresponds well with the southern parts of Mediano anticline (e.g. Poblè et. al. 1998). These structures have thereby developed in Lutetian time, in the same stress field as the Mediano anticline. The growth of A-1 and A-2 indicates a rotation in the stress field relative to development of A-3, from NE-SW orientation of maximum stress axis to WNW-ESE orientation.

Timing	**Process**
1 - Ypresian	Syn-sedimentary faults, documented from Las Uslas and central Caixicar de Pardina
2	Fractures related to burial, documented from Ainsa Quarry and northern Fuensalada
3	Growth of A-3 with related fracture sets
4	Displacement along the reverse fault, documented in southern Fuensalada
5 – Lutetian	Growth of A-1 and A-2
6	Fractures related to unloading, documented from Ainsa Quarry and central Fuensalada

Table 7.1: Age relationship between the different structures in the study area.

Chapter 7 – References

Adams, F. D. 1901. The excursion to the Pyrenees in connection with the eighth international geological congress. The Journal of Geology, v.9. 28-46.

Ako, O. J., In Prep. Structural development of the Ypresian-Lutetian sequence of the northeastern Ainsa Basin, Pyrenees, Spain. Master Thesis in Geoscience, Petroleum Geology and Geophysics, Department of Geosciences, University of Oslo.

Alhgren, S. G., Bump, A. P., Davis, G. H. & Garcia, P. E., 1999. Conjugate riedel deformation band shear zones. Journal of structural geology. v.22. 169-190.

Allen, P. A., Homewood, P. & Williams, G. D. 1986. Foreland Basins: an introduction. In: Foreland Basins (Edited by Allen, P. A. & Homewood, P.). Blackwell scientific publications.

Alsop, G. I., Holdsworth, R. E. & Strachan, R. A., 1996. Transport-parallel cross folds within a mid-crustal Caledonian thrust stack, northern Scotland. Journal of structural geology. v.18. 783-790.

Alvarez, W., Engelder, T., Geiser, P. A. & Marshak, S. 1982. Mesoscopic fault array of the northern Umbrian Apennine fold belt, Italy: Geometry of conjugate shear by pressure solution slip. Geol. Soc. Am. Bull. v.93. 1013-1022.

Anderson, E. M. 1951. The dynamics of faulting. Oliver & Boyd. Edinburgh.

Aragon 3D, 2007, Gobierno De Aragon, available at http://sitar.aragon.es/en/Vuelos_3D_en.html (accessed: 23.01.08)

Arbues, P., Muñoz, J. A. & Sierra-Kiel, J. 1998. The Ainsa Basin and the Sobrarbe oblique thrust system: Sedimentological and tectonic process controlling slope and platform sequences deposited synchronously with a submarine emergent thrust system. In: Field trip guide book of the 15th international sedimentological congress, Alicante (Edited by Hevia, A. M. & Soria, A. R.). 213-223.

Atkinson, C. D., Farrell, S. G. & Williams, G. D. 1987. Constraints on the age of movements of the Montsech and Cotiella thrusts, south central Pyrenees, Spain. J. Geol. Soc. London v.144, 907-914.

Aydin, A. & Pollard, D. D. 1988. Progress in understanding jointing over the past century. Geological Society of America Bulletin, v.100. 1181-1204.

Aydin, A., Bai, T., Gross, M. R. & Maerten, L. 2002. Orthogonal cross joints: do they imply a regional stress rotation? Journal of structural geology. v.24. 77-88.

Bahat, D., 1991. Tectonofractography. Springer-Verlag. Berlin

Bahat, D., 1999. Single-layer burial joints vs single-layer uplift joints in Eocene chalk from the Beer Sheva syncline in Israel. Journal of structural geology. v.21. 293-303.

Bai, T. & Pollard, D. D. 2000. Fracture spacing in layered rocks: a new explanation based on the stress transition. Journal of structural geology. v.22. 43-57.

Bakke, K., Gjelberg, J. & Petersen, S. A. 2007. Compound seismic modeling of the Ainsa 2 turbidite system, Spain: Application to deep-water channel systems offshore Angola. Marine and Petroleum Geology.

Bellahsen, N., Fiore, P. & Pollard, D. D. 2006. The role of fractures in the structural interpretation of Sheep Mountain Anticline, Wyoming. Journal of structural geology. v.28. 850-867.

Bentham, P. A., Burbank, D. W. and Puigdefabregas, C. 1992. Temporal and spatial control on the alluvial architecture of an axial drainage system: late Eocene Escanilla formation, southern Pyrenean foreland basin, Spain. In: Basin research. Volume 4. p 335-352.

Bergbauer, S. & Pollard, D. D. 2004. A new conceptiual fold-fracture model including prefolding joints, based on the Emigrant Gap anticline, Wyoming. Geological society of American Bulletin 116. 294-307.

Bhattacharya, J. P. & Davies, R. K., 2001. Growth faults at the pro delta to delta-front transition, Cretaceous Ferron sandstone, Utah. Marine and petroleum geology. v.18. 525-534.

Bond R.M.G. & McClay, K.R., 1995. Inversion of a Lower Cretaceous extensional basin, south central Pyrenees, Spain. In: Buchanan, J.G and Buchanan, P.G Editors, 1995. Basin Inversion **88** Geological Society of, London Special Publication, pp. 415–431.

Bouroullec, R., Guillocheau, F., Nalpas, T., Raillar, S. & Rouby, D., 2002. Kinematics of growth faults/raft system on the West African margin using 3-D restoration. Journal of structural geology. v.24. 783-796.

Carey, S. W. 1955. The Orocline Concept in Geotectonics, Part 1. In*:* Papers and proceedings of the Royal Society of Tasmania, volume 89. Tasmania. 255-288.

Choukroune, P. & Seguret, M. 1973. Tectonics of the Pyrenees: Role of Compression and Gravity. In: Gravity and Tectonics (Edited by deJong, K. A. & Scholtem, R. 1973). John Wiley, New York.

Clark J.D., 1995, A detailed section across the Ainsa II channel complex, south-central Pyrenees, Spain, *in* Pickering K.T., R.N. Hiscott, N.H. Kenyon, F. Ricci Lucchi and R.D.A. Smith, eds., Atlas of Deep Water Environments: Architectural Style in Turbidite Systems: Chapman and Hall, London, 212-215.

Clark J.D. & K.T. Pickering, 1996, Architectural elements and growth patterns of submarine

Clevis, Q., de Boer, P. L., de Jager, G. & Nijman, W. 2004. Stratigraphic signatures of translation of thrust-sheet top basins over low-angle detachment faults. Basin research. v.16. 145-163.

Collinson, J. D. 1994. Sedimentary deformational structures. In: The geological deformation of sediments (Ed. Maltman, A). Chapman & Hall. London.

Corregidor, J. & Pickering, K. T. 2005. Mass-transport complexes (MTCs) and tectonic control on basin-floor submarine fans, middle eocene, south Spanish Pyrenees. Journal of sedimentary research v.75.

Cronin, B.T., D. Owen, A.J. Hartley and B. Kneller, 1998, Slumps, debris flows and sandy deepwater channel systems: Implications for the application of sequence stratigraphy to deep water clastic sediments. Journal of the Geological Society, v. 155, p. 429-432.

Darwin, C. 1846. Geological observations in South America. Smith-Elder.

Davis, G. H. 1984. Structural Geology of Rocks and Regions. John Wiley & sons. New York.

Davis, G. H. & Reynolds, S. J. 1996. Structural Geology of Rocks and Regions. Second edition. John Wiley and sons, inc. New York. p. 665.

De Boer, P. L. & Peper, T. 1995. Intrabasinal thrust-tectonic versus climate control on rhythmicities in the Eocene South Pyrenean Tremp-Graus foreland basin: inferences from forward modeling. Tectonophysics. v.249. 93-107.

Delaney, P. T., Pollard, D. D. & Segall, P. 1982. Formation and interpretation of dilatants echelon cracks. Geological Society of America Bulletin, v.93. 1291-1302.

Dickinson, W. R. 1974. Plate tectonics and sedimentation. In: *Tectonic and sedimentation* (Edited by Dickinson, W. R.). Spec. Publ. Soc. Econ. Paleont. Miner., Tulsa.

DiMaggio, E. 2005. ActiveTectonics. Available at: http://activetectonics.asu.edu/Med_Land/MedLand.htm (Accessed: 30.01.2008).

Dreyer, T., Arbues, P., Corregidor, J. and Puigdefabregas, C. 1999. Architacture of the tectonically influenced Sobrarbe deltaic complex in the Ainsa Basin, northern Spain. Sedimentary Geology. v.127. 127-169.

Dunne. W. M. 1986. Mesostructural development in detached folds: an example from west Virginia. Journal of Geology. v.94. 473-488.

Dunne, W. M. & North, C. P. 1990. Orthogonal fracture systems at the limits of thrusting: an example from southwestern Wales. Journal of structural geology. v.12. 207-215.

Dunne, W. M. & Hancock, P. L. 1994. Palaeostress Analysis of Small-Scale Brittle Structures. In: Continental Deformation (Edited by Hancock, Paul L.). Pergamon Press, Oxford, p. 101-120.

Engelder T. 1984. Loading paths to joint propagation during a tectonic cycle: an example from the Appalachian Plateau, U.S.A. Journal of structural geology. v.7. 459-476.

Engelder, T., 1985. Correlation between abnormal pore pressure and tectonic jointing in the Devonian Catskille Delta. *Geology*. Vol. 13. 863-866.

Fairbairn, H. W. 1954. Structural petrology of deformed rocks. Addison-Wesley publishing company, Inc. Cambridge.

Farrell, S. G., Williams, G. D. & Atkinson, C. D., 1987. Constraints on the age of movement of the Monsech and Cotiella thrusts, south central Pyrenees, Spain.*Journal of geological society,* London. Vol. 8. 907-914.

Fernandez, E., Estrada, O., Maestro, L. P., Oms, E., Remacha, E. & Teixel, R. 1998. The upper Hecho Group turbidites and their vertical evolution to deltas (Eocene, south-central Pyrenees). In: Hevia, A.M., Soria, A.R. (Eds.), Field Trip Guidebook of the 15th International Sedimentological Congress, Alicante. 3–25.

Fernandez, O., Muñoz, J. A., Arbues, P., Falivene, O. & Marzo, M., 2004. Threedimensional reconstruction of geological surfaces: An example of growth strata and turbidite systems from the Ainsa Basin (Pyrenees, Spain). American Association of Petroleum Geologists. Bulletin, v. 88. p. 1049-1068.

Fischer, M. P. & Wilkerson, M. S. 2000. Predicting the orientation of joints from fold shape: results of pseudo-three-dimensional modeling and curvature analysis. Geology, v.28. 15-18.

Flåt, R., In Prep. Development and sedimentology of Lower Eocene deep-marine gravity flow deposits in the eastern part of the Ainsa Basin, Pyrenees, Spain. Master Thesis in Geoscience, Petroleum Geology and Geophysics, Department of Geosciences, University of Oslo.

Fonnesu, G., Mutti E., Rampone, F., and Sonnino, M.1981, Channel fill and associated overbank deposits in the Eocene Hecho Group, Ainsa-Boltaña region (south-central Pyrenees): IAS 2nd European Regional Meeting, Bologna, 113-116.

Fontana, D., Garzanti, E. & Zuffa, G. G. 1989. The interaction of eustacy and tectonism from provencestudies of the Eocene Echoho Group Turbidite Complex (South-central Pyrenees). Basin Research v.2. 223-237.

Fossen, H. & Gabrielsen, R. H. 2005. Strukturgeologi. Fagbokforlaget Vigmostad & Bjørke AS. Bergen.

Friedman, M. 1972. Residual elastic strain in rocks. Tectonophysics. Elsevier publishing company. Amsterdam.

Friend, G. G. & Ori, P. F. 1984. Sedimentary basins formed and carried piggyback on active thrust sheets. Geology, v.12, p. 475-478.

Gabrielsen, R. H., Arland, R. K. & Alsaker, E., 1998. Identification and spatial distribution of fractures in porous, siliciclastic sediments. In: Structural geology in Reservoir Characterization (Edited by Coward, M. P., Daltaban, T. S. & Johnson, H.). Geological society, London. 49-64.

Ghosh, S. K. 1988. Teory of chocolate tablet boudinage. Journal of structural geology, v. 10. 541-553.

GoogleEarth™, 2008, GoogleEarth, available at http://earth.google.com/ (Accessed: 23.05.08).

GoogleMaps™, 2008, GoogleMaps, available at: http://maps.google.com/maps?hl=en&tab=wl (Accessed: 23.05.08).

Griffith, A. A. 1920. The phenomena of rupture and flow in solids. Philosophical Transactions of the royal society of London A221, 163-198.

Hansen, E., 1971. Strain Facies. New York, Springer-Verlag.

Hancock, P. L. 1985. Brittle microtectonics: principles and practice. Journal of structural geology, v.7. 437-457.

Hatcher, R. D. 1990. Structural Geology - Principles, Concepts and Problems. Macmillan Publishing Company, New York.

Hayes, M. & Hanks, C. L., 2008. Evolving mechanical stratigraphy during detachment folding. Journal of structural geology. v.30. 548-564.

Hencher, S. R., Lumsdem, A. C., Petit, J. P., Rawnsley, K. D. & Rives, T. 1992. Joint Development in perturbed stress fields near faults. Journal of Structural geology, v.14. 939-951.

Hunt, D. W. & Kosa, E., 2005. Growth and syndepositional faults in carbonate strata: Upper Permian Capitan Platform, New Mexico, USA. Journal of structural geology. v.27. 1069-1094.

Jackson, J. A., Mehl, J. P. & Neuendorf, K. K. E., 2005. Glossory of geology – fifth edition. American geological institute. Virginia.

Jamison, W. R. 1987. Geometric analysis of fold development in overthrust terranes. Journal of structural geology. v.9. 207-219.

Johnson, A. M. & Berger, P., 1989. Kinematics of fault-bend folding. Engeneering geology. v.27. 181-200.

Ladeira, F. L. & Price, N. J., 1981. Relationship between fracture spacing and bed thickness. Journal of structural geology. v.3. 179-183.

Lopez-Blanco, M., Marzo, M. & Munoz, J. A. 2003. Low-Amplitude, synsedimentary folding of a deltaic complex: Roda sandstone (lower Eocene), South-Pyrenean Foreland Basin. Basin Research. v.15. 73-95.

Lucchi, F. R. 1986. The Ologocene to Recent foreland basins of the northern Apennin. In: Foreland Basins (Edited by Allen, P. A. & Homewood, P.). Blackwell scientific publications.

Maltman, A. J., 1988. The importance of shear zones in naturally deformed wet sediments. Tectonophysics. v.145. 163-175.

Marzo, M., Nijman, W. & Puigdefabregas, C. 1988. Architecture of the Castissent fluvial sheet sandstones, Eocene, South Pyrenees, Spain. Sedimentology. v.35. 719-738.

McClay, K, Munoz, J. A. & Poblet, J., 1994. Synchronous extension and contraction in frontal thrust sheets of the Spanish Pyrenees. Geology. v.22. 921-924.

Melick, J., Cavanna, G., Benevelli, G., Tinterri, R. & Mutti, E., 2004. The Lutetian Ainsa Sequence: an example of a small turbidite system deposited in a tectonically controlled basin. Dipartimento di Scienze della Terra, Parma.

Mey, P. H. W., Nagtezaal, P. J. C., Roberti, K. J. & Hartevelt, J. J. A. 1968. Lithostratigraphic subdivision of post Hercynian deposits in the south central Pyrenees, Spain. Leid. Geol. Meded, 41, p. 221-228.

Mueller, K. & Talling, P., 1996. Geomorphic evidence for tear faults accommodating lateral propagation of an active fault-bend fold, Wheeler Ridge, California. Journal of structural geology. v.19. 397-411.

Munoz, J. A. 1992. Evolution of a continental collision belt: ECORS- Pyrenees crustal balanced cross-section. In: Thrust tectonics (Ed. By McClay, K. R.). Chapman & Hall. London.

Munoz, J. A., Puigdefabregas, C. & Verges, J. 1992. Thrusting an foreland basin evolution in the southern Pyrenees. In: Thrust tectonics (Ed. By McClay, K. R.). Chapman & Hall. London.

Mutti, E., and W.R Normark, 1987, Comparing examples of modern and ancient turbidite systems: Problems and concepts, In: Legget J.K., and G.G. Zuffa, eds.: Marine Clastic Sedimentology: Graham and Trotman, London, p.1-38.

Mutti,E., Seguret, M. & Sgavetti, M., 1988. Seimentation and deformation of the Tertiary sequences of the southern Pyrenees. American Association of Petroleum Geologists Mediterranean Basins Conference, Field Tripn No. 17, Nice.

Mutti, E., and W.R Normark, 1991, An integrated approach to the study of turbidite systems, In: Weimer, P., and M.H. Link, eds., Seismic Facies and Sedimentary Processes of Modern and Ancient Submarine Fans: SpringerVerlag, New York, p. 75-106.

Nickelsen, R. P. 1979. Sequence of structural stages of the Alleghany orogeny, at the Bear Valley Strip Mine, Shamokin, Pennsylvania. American Journal of Science, v.279. 225-271.

Nijman, W. J. 1989. Thrust sheet rotation? – The south Pyrenean Tertiary Basin configuration reconsidered. Geodinamica act 3.

Nijman, W. J. 1998. Cyclicity and basin axis shift in a piggy-back basin: towards modeling of the Eocene Tremp-Ager Basin, South Pyrenees, Spain. In*: Cenozoic foreland basins of western Europe* (Ed. Fernandez, M., Luterbacher, H. P., Mascle, A. & Puigdefabregas, C). Geol. Soc. Spec. Publ., v.134. 135-163.

Petit, J. P., Rawnsley, K. D. & Rives, T., 1994. Analogue simulation of natural orthogonal joint set formation in brittle varnish. Journal of structural geology. v.16. 419-429.

Pickering, K. T. & Corregidor, J., 2000. 3D reservoir scale study of Eocene confined submarine fans, south central Spanish Pyrenees. In: Weimer, P., Slatt, R. M., Coleman, J., Rosen, N. C., Nelson, H., Bouma, A. H., Styzen, M. J. & Lawrence, D. T., eds., Deep water reservoirs of the world: SEPM, Gulf Coast Section, 20th Annual Bob F. Perkins research Conference, p. 776-781.

Poblet, J., Munoz, J. A., Serra-Kiel, J. & Trave, A. 1998. Quantifying the kinematics of detachment folds using three-dimensional geometry: Application to the Mediano anticline (Pyrenees, Spain). GSA Bulletin. v.110. 111-125.

Pollard, D.D. & Olson, J. E., 1991. The initiation and growth of en echelon veins. Journal of structural geology. v.13. 595-608.

Price, N. J. 1966. Fault and joint development in brittle and semi-brittle rock. Pergamon press. London.

Price, N. J. & Cosgrove, J. W., 1990. Analysis of Geological Structures. Cambridge University Press, Cambridge, p. 366-384.

Puigdefàbregas, C. & Souquet, P. 1986. Tecto-sedimentary cycles and depositional sequences of the Mesozoic and Tertiary from the Pyrenees. In: Tectonophysics v.129. 173-203.

Ramsay, J. G. 1961. The effects of folding upon the orientation of sedimentary structures. Journal of Geology, v.69. 84-100.

Ramsay, J. G. 1967. Folding and Fracturing of Rocks. McGraw-Hill Book Company, New York.

Reading, H. G. 1996. Sedimentary environments: Processes, Facies and Stratigraphy. Blackwell Science Ltd. London. Third Edition.

Rich, J. L., 1934. Mechanics of low-angle overthrust faulting as illustrated by Cumberland thrust block. Virginia, Kentucky and Tennessee. Am. Assoc. Pet. Geol. Bul., v.118. 1584-1596.

Sander, Bruno. 1948. Einführung in die Gefügekunde der Geolischen Körper. Springe, Vienna, v.1.

Schuppers J..D., 1995, Characterization of deep-marine clastic sediments from foreland basins: Ph.D. Thesis, Delft University of Technology, Holland.

Scrope, G. P. 1825. Considerations on volcanoes, the probable causes of their phenomena, the laws which determine their march, the disposition of their products, and their connexion with the present state and past history of the globe; leading to the establishment of a new theory of the earth: W. Phillips, London.

Selzer, Georg, 1933. Geologie der Südpyrenäischen Sierren in Oberaragonien. E. Schweizerbart`sche Verlagsbuchhandlung, Stuttgart.

Sibuet, J. C., Spakman, W. & Srivastave, S. P. 2004. Pyrenean orogeny and plate kinematics. Journal of Geophysical research, v.109.

Stearns, D. W. 1964. Macrofracture pattern on Teton anticline, northwestern Montana. Trans. Am. Geophys. v.45.

Tavani, S., Storti, F. & Salvini, F., 2004. Rounding hinges to fault-bend folding: geometric and kinematic implications. Journal of structural geology. v.27. 3-22.

Tavani, S., Storti, F. & Salvini, F., 2006. Double-edge fault-propagation folding: geometry and kinematics. Journal of structural geology. v.28. 19-35.

Teixel, A. 1996. The Ansò transect of the southern Pyrenees: basement and cover thrust geometries. Journal of the Geological Society, London, v.153, 301-310.

Travè, A., Briqueu, L., Buatier, M., Calvet, F., Labaume, P., Potdevin, J. L., Raynaud, S., Seguret, M., Soler, A. & Raynaud, S., 1998. Fluif migration during Eocene thrust emplacement in the south Pyrenean foreland basin (Spain): an integrated structural, mineralogical and geochemical approach. Geological society, London. v.134. 163-188.

Twiss, R. J. & Moores, E. M., 1992. Structural geology. W. H. Freeman Company. New York.

Van Der Pluijm, B. A. & Marshak, S., 2004. Earth Structure, Second edition. W. W. Norton & Company, Inc. New York.

Verges, J., Marzo, M., & Munoz, J. A., 2002. Growth strata in foreland setting. Sedimentary geology. v.146. 1-9.

Vincent, S. J. 1999. The role of sediment supply in controlling alluvial architecture: an example from the Spanish Pyrenees. Journal of the geological society. v.156. 749-759.

Vincent, S. J. 2001. The Sis palaeovalley: a record of proximal fluvial sedimentation and drainage basin development in response to Pyrenean mountain building. Sedimentology. v.48. 1235-1276.

Warren, C. S. 1955. The orocline concept in Geotectonics, Part 1. Royal Society of Tasmania. 255-288.

Whaley, J. 2008. Pyrenees hold clues to fractured Carbonate Reservoirs. GeoExpro. v.5, no. 1.

Whitten, E. H. 1969. Structural Geology of Folded Rocks. Rand McNally & Company.

Williams, G. D. 1985. Thrust tectonics in the south central Pyrenees. Journal of structural geology, v.7, Cardiff, 11-17.

Woyessa, A.T., In Prep. Depositional environment, sequence stratigraphy and reservoir properties of an Eocene mixed carbonate-siliciclastic succession in the Ainsa Basin, Southern Pyrenees. Master Thesis in Geoscience, Petroleum Geology and Geophysics, Department of Geosciences, University of Oslo

Appendix I

There are four primary settings which joints are developed in. These four are Hydraulic, tectonic, unloading and release (Cosgrove & Price, 1990). The hydraulic and tectonic deduced joints develop at depths prior to uplift as a response of abnormal fluid pressure, whereas unloading and release deduced joints form at the surface as a result of thermal elastic contraction accompanying erosion and uplift (Engelder, 1984). The difference between the hydraulic and tectonic deduced joints is how the abnormal pore pressure is achieved. The hydraulic joints develop during mechanical compaction by overburden, whereas tectonic joints develop during tectonic compaction. The difference between the unloading joints and release joints is the orientation of the joints, which, regarding unloading joints is decided by either a residual or a contemporary tectonic stress, whereas the orientation of release joints is controlled by a rock fabric.

Fractures related to folds

Joints are developed in an extensional strain field since no offset can be recorded, except normal to the fracture surface (Hatcher, 1990). When joints are present in a fold, which is a compressional structure, and the joints can be related to the folding, extensional strain must have been present in the structure during development.

The dilation fractures are normally oriented such that they cut the fold axis 90^{o}, and are normally also perpendicular to the bedding. They are then usually vertical or steeply dipping features (Cosgrove & Price, 1990). These extensional fractures are usually filled with calcite - or quartz – cement. Joints are good indicators of paleostress since they are sensitive markers of small stress changes, and inhomogeneous stress fields result in curving joints (Delaney et. al, 1982; Hencher et. al, 1992). Joints are also used as indicators of paleostress orientation since they form parallel to the σ_1-σ_2 plane and normal to σ_3 (Griffith, 1920; Aydin & Pollard, 1988).

Appendix I

Shear fractures are more complexly related to folding. Shear fractures include normal, thrust, strike-slip and oblique-slip faults. The orientation of oblique-slip fractures are determined by the orientation of the bedding.

Both shear and dilation fractures related to folding can be used in determining orientation and relative magnitudes of the principal stresses which were associated with the intension of the various fracture systems.

Mechanics of development of fracture patterns within folds

A lot of work has been managed out regarding joint and fault development within folds (Stearns, 1964; Price, 1966; Nickelsen, 1979; Alvarez et. al, 1982). Joints can develop in folds as a function of magnitude of the local stress and the fluid pressure which obtains in the rock. If joints develop as a result of folding, the orientations of the joints will reflect the fold-related stress trajectories and fold kinematics. If joints are not related to folding, they will reflect paleostress at the time of jointing (Fischer & Wilkerson, 2000). It is important to understand the making of joints within folds, since these may reflect paleostress at the time of development, and are important for production of reservoirs located within anticlines. They may form parallel, normal and oblique to the fold axis and axial surface, depended on local fold-related strain and on when the fractures form during the evolution of the fold (Price, 1966; Whitten, 1969; Fischer & Wilkerson, 2000). This is based on the theory that joints open parallel to the maximum stretch direction of a layer and that this direction is parallel to the maximum curvature of a surface. Stress is referred to as maximum, intermediate and minimum principle stress. These are σ_1, σ_2 and σ_3, respectively. By plotting strike and dip into stereonet, relationship between folds and fractures can be established. Figure A-1 is an illustration of one fracture system related to the development of the fold. This is seen directly on the stereonet since the poles of the fractures lie on the best fit great circle to the fold. There are three main characteristics regarding fold-related fractures. These are the orientation, distribution and the density of each fracture population.

Appendix I

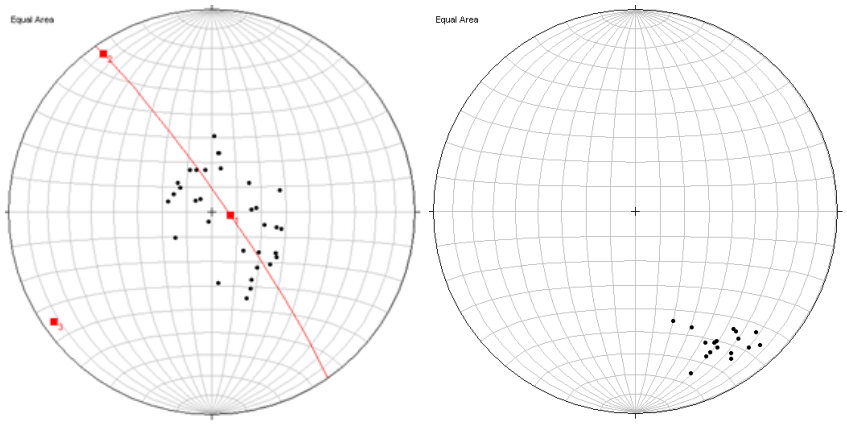

Figure A-1: Illustration of how poles in fractures (to the right) are plotted when they potentially are directly related to the formation of the fold (to the left).

There are 11 common fracture orientations in folded strata, which are comprised in four fracture sets which form systematically with respect to both the fold axis and bedding (Stearns, 1968) (figure A-2).

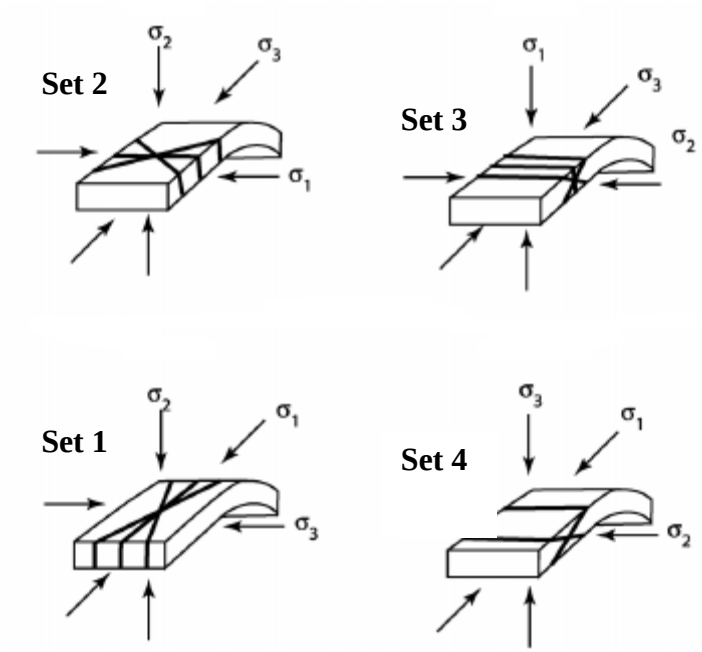

Figure A-2: Illustrations of the 11 common fracture orientations in folded strata. Developed from Stearns (1964).

The fracture set 1 is a result of vertical intermediate (σ_2) stress direction together with a maximum stress (σ_1) direction parallel with the dip direction. Then, one tensile fracture population develop parallel to the maximum stress direction (and dip-direction), and two strike-slip fracture populations develop obliquely to σ_1. Fracture set 2 develops when intermediate stress direction is vertical, but the maximum and intermediate stress directions change directions compared to fracture set 1. In this case, the maximum stress direction is parallel with the fold axis. Then, the same pattern occurs as for fracture set 1, except a 90^o rotation of the respective fracture populations. The fracture set 3, defined by Sterns, is comprised by two shear fractures populations, with normal offset, together with one tensile fracture population. The fourth fracture set includes two orientations of thrust faults (Stearns, 1964). Due to differences in stress directions under which the different fracture sets are formed, Stearns suggested that the fracture set 1 develops in the early stage of folding, set 2 starts to develop when the extension perpendicular to the fold axis becomes large compared to the size of the fold itself, and that sets 3 and 4 develop due to local bending and buckling within the fold.

To develop joints, fluid pressure must be high:

$$p > \sigma_3 + T$$

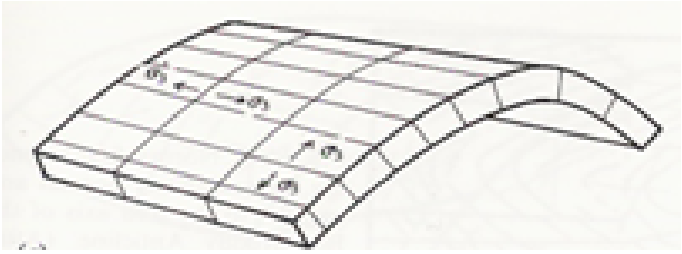

Figure A-3: Typical relationship of joints in a fold. Direction of minimum principle stress is also shown (Cosgrove, 1990).

Where p is the fluid pressure, T is the tensile strength of the rock and σ_3 is the minimum principal stress. Figure A-3 and A-4 are illustrations of such joints. The direction of strike is dependent on direction of maximum, intermediate and minimum stress locally within the fold. Increasing fluid pressure decreases effective normal stress until the strength of the tensile strength of the rock is exceeded. Simultaneously, the differential stress must be low.

$$\sigma_1 - \sigma_3 < 4T$$

Such joints in folded rocks indicate local extensional strain together with compression (Hatcher, 1990).

For the development for shear fractures, the differential stress must be higher, so that:

$$\sigma_1 - \sigma_3 > 4T$$

And the fluid pressure must be lower than for hydraulic fracturing:

$$P < \sigma_3 + T$$

There is a general empirical relationship between Young's modulus and the strength of a rock (Cosgrove & Price, 1990). This means that increasing the strength three times will increase the value of the elastic modulus ten times. This is why the strong rocks, with maximum strength, fractures before softer rocks. The differential stress becomes sufficient high in strong rocks before softer rocks.

If the intermediate principle stress is parallel with the fold axis, minor thrusts may develop. The minimum principal stress is then located vertically. If the intermediate principle stress is vertically, and the minimum principle stress is parallel with the fold axis, dilation fractures may develop perpendicular to the fold axis.

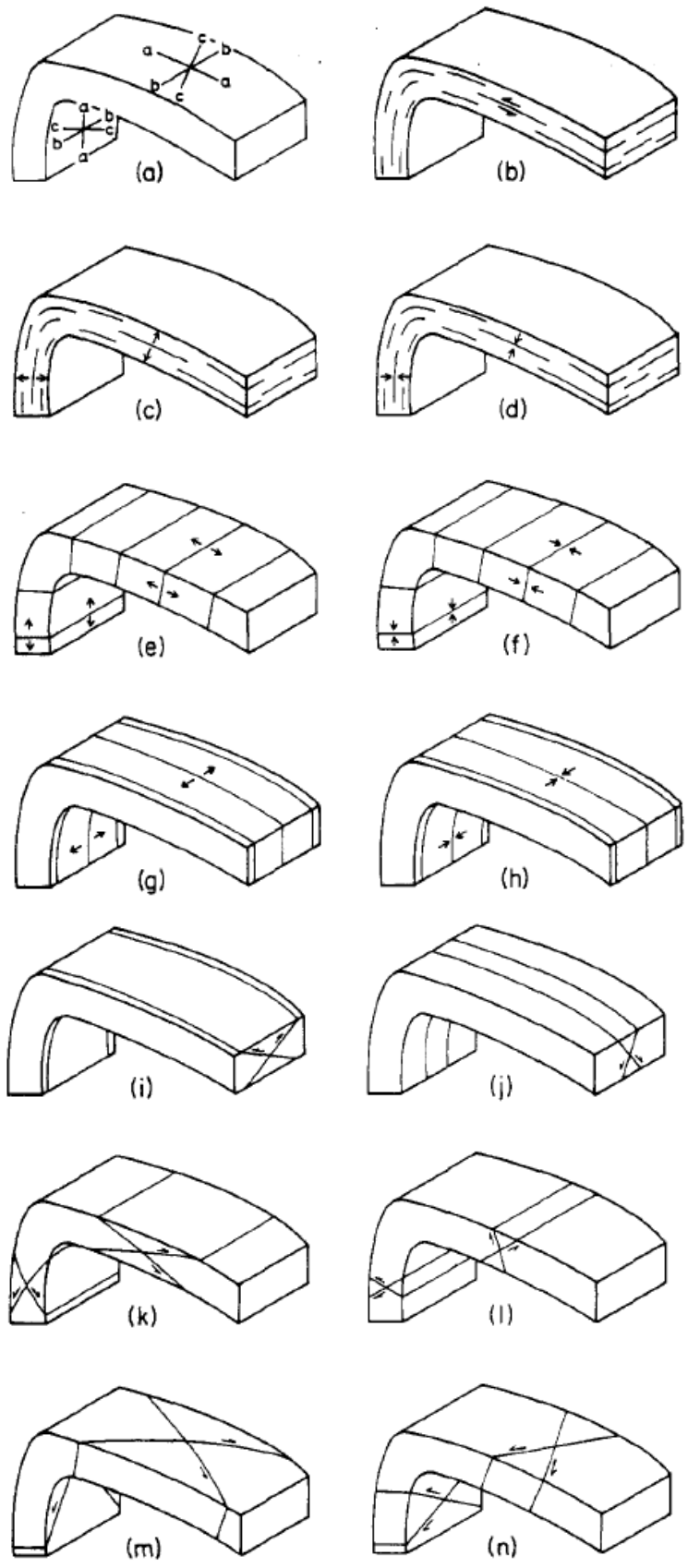

Figure A-4: Blocks illustrating fracture set development relative to sedimentary layering and the hinge line of the fold.Planes perpendicular to one plane but contains the other two are defined to be in the a-b, a-c or b-c plane. Surfaces obliquely to two axes but containing one are defined as 0kl, h0l and hk0; h, k and l refers to notional intercepts on the a, b anc axes respectively, and 0 indicating parallelism to one axis.

a) Definition of the a-b-c directions at the different parts of the fold.
b) Shear fractures in the a-b plane.
c) Tensile fractures in the a-b plane
d) Development of stylolites in the a-b plane.
e) Extensional fractures (tensile) in the b-c plane.
f) Stylolites in the b-c plane.
g) Extensional fractures (tensile) in the a-c plane.
h) Stylolites in the a-c plane.
i) Conjugate 0kl fractures with an angle about b.
j) Conjugate 0kl fractures with an angle about c.
k) Conjugate 0kl fractures with an angle about a.
l) Conjugate hOl fractures enclosing an acute angle about c.
m) Conjugate hk0 fractures with an acute angle about a.
n) Conjugate hk0 fractures with an acute angle about b.

Figure and text from Hancock, 1985.

Thin sections

Host rock at central Fuensalada

The rock sample was gathered to investigate the host rock in bed 2 at locality 5 (figure 5.7). The limestone at this locality has the same properties as the overall limestone in the area. As figure A-5 illustrates, the main component in the matrix are carbonates. The bigger fossils in the rock sample are nummolites of different form. There is also calcite in the matrix, together with quartz, indicating clastic input.

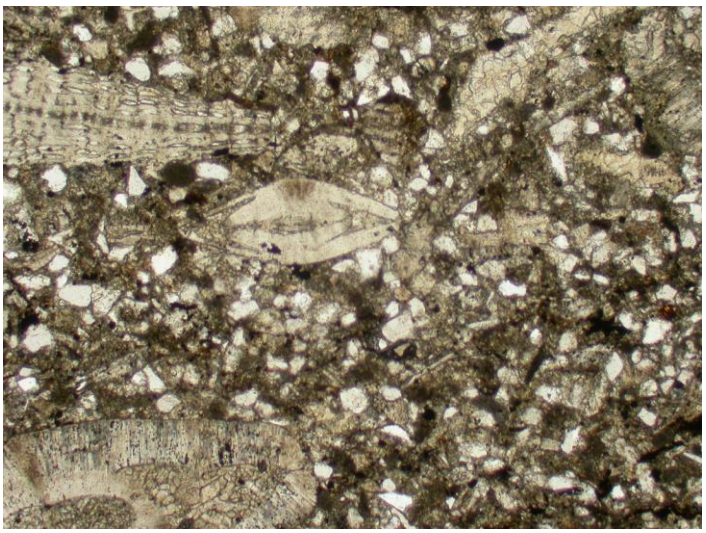

Figure A-5: Host rock at central Fuensalada. Several fossils are observed in the picture. The matrix consists of mainly fossil fragments. Picture taken with 5 optical zoom.*

Population L5

A rock sample was gathered of the fracture population L5. This sample was taken to illustrate direction of growth and timing of growth compared to opening of fracture. The thin section was cut parallel to opening of the fracture, i.e. parallel to growth of fracture fill. The host rock is similar to rock sample one. The fracture cuts through all fossils, indicating that the opening of fractures where not dependent of the Lithological characteristics. The actual fossils which are cut through are nummolites. The fracture has a central open space, indicating syntaxial growth of cement infill, confirmed by the thin section showing an

increase in crystal size towards the central part (figure A-6). The calcite has also grown perpendicular to the vein wall, indicating no shear along the fracture after precipitation of calcite.

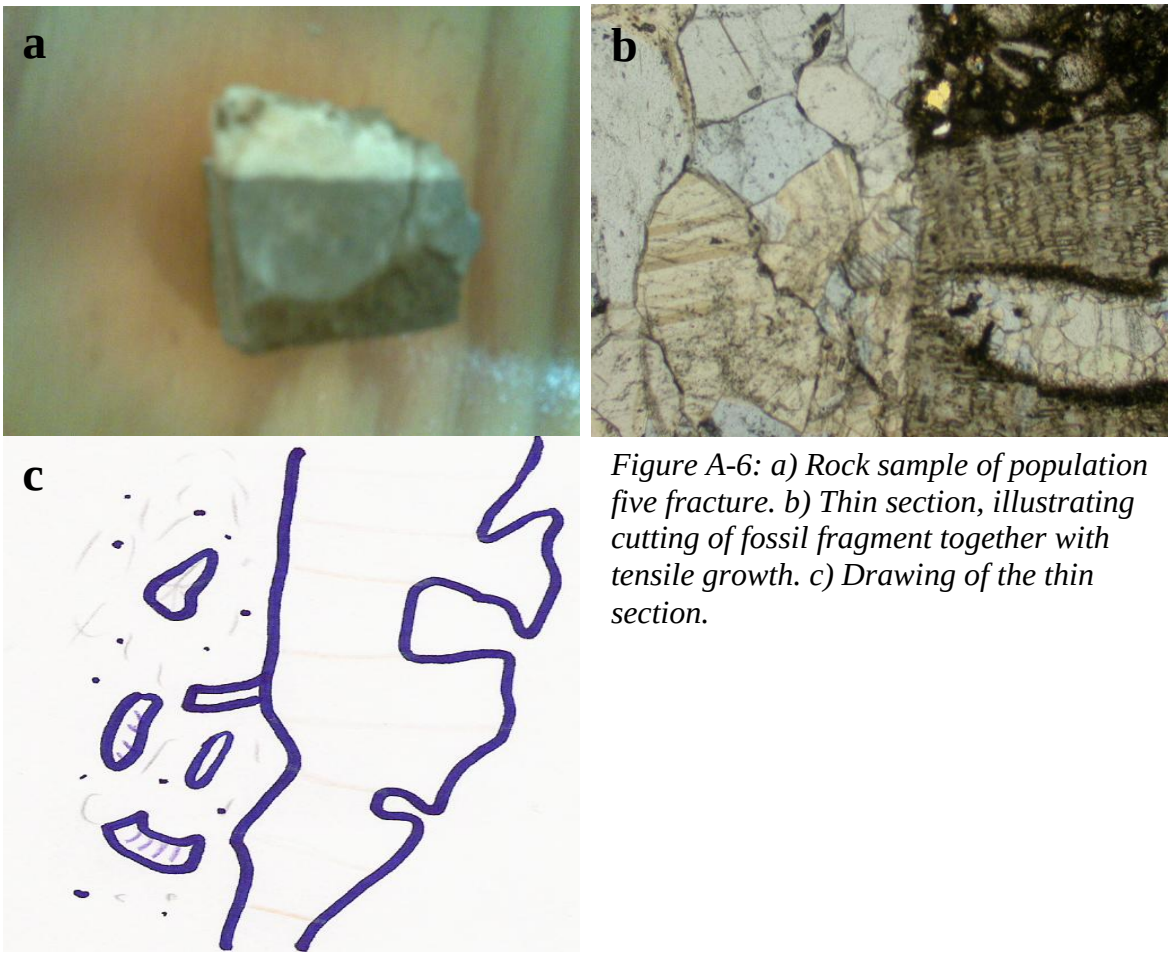

Figure A-6: a) Rock sample of population five fracture. b) Thin section, illustrating cutting of fossil fragment together with tensile growth. c) Drawing of the thin section.

Appendix II

Strike	Dip	cc/-cc	Mode	Form	Offset(cm)
339	43	cc	M2	S	160
?	?	?	M2	?	80
312	45	cc	M2	S	225
320	40	cc	M2	S	160
315	53	cc	M2	S	154
?	?	cc	M2	S	?

Table 1: Field Data gathered from the Las Uslas.

Appendix II

Number	**Strike**	**Dip**	**cc/-cc**	**Mode**	**MW (mm)**	**Form**	**Offset(cm)**
1	337	54	−cc	M1	10	S	
2	310	42	−cc	M1	3	Curved	
3	339	62	cc	M2	5	Curved	
4	344	47	−cc	M2		Curved	40
5	334	75	−cc	M2	2	S	5
6	346	62	−cc	M2	1	S	
7	339	66	−cc	M2	1	S	21
8	326	58	cc	M2	45	Curved	21
9	325	83	−cc	M2	2	Curved	27
10	343	55	−cc	M2	28	S	20
11	318	66	−cc	M2	5	S	
12	334	79	cc	M2	18	Curved	18
13	339	74	cc	M2	19	S	120
14	322	72	−cc	M2	4	Curved	
15	340	62	−cc	M2	4	Curved	12
16	331	61	−cc	M2	1	S	25
17	324	71	−cc	M2	2	S	14

Table 2: Field Data gathered from the central Caixicar de Pardina.

Strike	Dip	Bed number	cc/-cc	Mode	MW (mm)	Open/closed	Form
265	82	BED1	cc	M1	20	Closed	S
262	82	BED1	cc	M1	3	Closed	S
262	78	BED1	cc	M1	1	Closed	W
266	77	BED1	cc	M1	3	Closed	S
258	77	BED1	cc	M1	2	Closed	W
264	83	BED1	cc	M1	3	Closed	W
273	89	BED1	cc	M1	3	Closed	S
258	87	BED1	cc	M1	3	Closed	W
261	79	BED1	cc	M1		Closed	S
270	86	BED1	cc	M1	4	Closed	W
273	67	BED1	cc	M1	1	Closed	S
89	81	BED2	cc	M1	1	Closed	S
86	85	BED2	cc	M1	2	Closed	S
75	84	BED2	cc	M1	4	Closed	S
77	85	BED2	cc	M1	2	Closed	S
78	75	BED2	cc	M1	5	Closed	W
76	86	BED2	cc	M1	1	Closed	S
81	88	BED2	cc	M1	1	Closed	S
79	82	BED2	cc	M1	3	Closed	S
80	80	BED2	cc	M1	2	Closed	S
89	77	BED2	cc	M1	1	Closed	S
270	81	BED3	cc	M1	0,5	Closed	S
259	85	BED3	cc	M1	2	Closed	W
269	81	BED3	cc	M1	2	Closed	S

Table 3: Field data of population Q1 fractures

Strike	Dip	Bed number	cc/-cc	Mode	MW (mm)	Open/closed	Form
65	85	BED1	cc	M1	2	Closed	S
58	77	BED1	cc	M1	1	Closed	S
58	89	BED1	cc	M1		Closed	S
56	63	BED1	cc	M1		Closed	S
67	75	BED1	cc	M1		Closed	S
57	69	BED1	cc	M1	1	Closed	W
71	84	BED2	cc	M1	1	Closed	S
70	80	BED2	cc	M1	1	Closed	S
70	73	BED2	cc	M1	1	Closed	S
69	79	BED2	cc	M1	1	Closed	S
70	80	BED2	cc	M1	6	Closed	S
70	87	BED2	cc	M1	0,5	Closed	S
60	76	BED2	cc	M1	5	Closed	W
245	83	BED3	cc	M1	5	Closed	S
240	85	BED3	cc	M1	0,5	Closed	S
247	88	BED3	cc	M1	1	Closed	S
243	80	BED3	cc	M1	2	Closed	S
249	86	BED3	cc	M1		Closed	S
246	83	BED3	cc	M1	1	Closed	S
250	86	BED3	cc	M1	0,5	Closed	S
245	80	BED3	cc	M1	1	Closed	W
255	85	BED3	cc	M1	1	Closed	S
241	78	BED3	cc	M1	1	Closed	S
249	88	BED3	cc	M1	1	Closed	W
251	81	BED3	cc	M1	5	Closed	SW

Table 4: Field data of population Q2 fractures

Strike	Dip	Bed Number	cc/-cc	Mode	MW (mm)	Open/closed	Form
35	84	BED1	cc	M1	6	Open	W
228	77	BED1	cc	M1		Open	S
36	78	BED1	cc	M1	1	Closed	S
41	84	BED1	cc	M1	1	Closed	S
46	62	BED1	cc	M1	1	Closed	W
50	72	BED1	cc	M1	1	Closed	S
42	69	BED1	cc	M1	1	Closed	S
52	71	BED1	cc	M1	2	Open	S
226	90	BED1	cc	M1	5	Closed	W
223	85	BED2	cc	M1	2	Closed	S
233	89	BED2	cc	M1	10	Closed	S
234	86	BED2	cc	M1	3	Closed	W
233	86	BED2	cc	M1	1	Closed	W
44	78	BED3	cc	M1	3	Closed	S
48	82	BED3	cc	M1	3	Closed	W

Table 5: Field data of population Q3 fractures

Strike	Dip	cc/-cc	Mode	MW (mm)	Open/closed	Form
118	70	-cc	M1	1	Closed	W
297	82	-cc	M1	1	Closed	S
291	83	-cc	M1	12	Closed	W
297	87	-cc	M1	3	Closed	S

Table 6: Field data of population Q4 fractures

Strike	Dip	cc/-cc	Mode	MW (mm)	Open/closed	Form
38	88	cc	M1	0,5	Closed	S
232	90	cc	M1	1	Closed	S
222	89	cc	M1	3	Closed	W

Table 7: Field data of population Q5 fractures

Distance (cm)	Strike	Dip	cc/-cc	Mode	MW (mm)	Open/closed	Form
	270	56	cc	M1	8	Open	S
65	266	66	cc	M1	8	Open	S
67	271	64	cc	M1	8	Open	S
56	269	62	cc	M1	8	Open	S
76	261	58	cc	M1	8	Open	S
56	262	55	cc	M1	8	Open	S
61	257	60	cc	M1	8	Open	S
59	248	56	cc	M1	8	Open	S
60	247	57	cc	M1	8	Open	S
61	247	60	cc	M1	8	Open	S
100	267	64	cc	M1	8	Open	S
104	260	62	cc	M1	8	Open	S
98	254	60	cc	M1	8	Open	S
76	253	70	cc	M1	8	Open	S

Table 8: Field data of population L1 fractures at northern Caixicar de Pardina

Distance (cm)	Strike	Dip	cc/-cc	Mode	MW (mm)	Open/closed	Form
	238	65	cc	M1	11	Closed	S
100	251	48	cc	M1	4	Closed	S
48	242	68	cc	M1	5	Closed	S
27	244	54	cc	M1	?	Closed	S
0	231	70	−cc	M1	?	Closed	S
75	239	65	−cc	M1	3	Closed	SC
48	230	67	−cc	M1	4	Closed	SC
60	237	76	−cc	M1	3	Closed	S
37	244	69	−cc	M1	1	Closed	SC
52	236	74	−cc	M1	1	Closed	S
60	242	63	−cc	M1	2	Closed	S
87	239	68	−cc	M1	2	Closed	S
45	251	74	−cc	M1	1	Closed	S
131	230	65	−cc	M1	2	Closed	SC
160	225	74	−cc	M1	1	Closed	S
119	230	77	−cc	M1	1	Closed	S
101	227	80	−cc	M1	1	Closed	SC

Table 9: Field data of population L1 fractures at central Fuensalada

Appendix II

Distance (cm)	Strike	Dip	cc/-cc	Mode	MW (mm)	Open/closed	Form
	333	68	cc	M1	8	Open	S
354	352	67	cc	M1	8	Open	S
423	330	85	cc	M1	8	Open	S

Table 10: Field data of population L2 fractures at northern Caixicar de Pardina

Strike	Dip	cc/-cc	Mode	MW (mm)	Open/closed	Form
311	70	cc	M1	9	Closed	S
332	65	cc	M1	10	Closed	S
328	60	cc	M1	9	Closed	Curved
321	65	cc	M1	9	Closed	W
314	61	cc	M1	14	Closed	W
293	67	cc	M1	5	Closed	W
315	73	cc	M1	1	Closed	W
321	60	cc	M1	1	Closed	W
313	72	cc	M1	8	Closed	W
323	74	cc	M1	4	Closed	W
313	64	cc	M1	11	Closed	W
307	69	cc	M1	3	Closed	W
312	66	cc	M1	9	Closed	W
308	79	cc	M1	1	Closed	S
319	72	cc	M1	6	Closed	W
309	66	cc	M1	2	Closed	S
319	79	cc	M1	1	Closed	S
318	73	cc	M1	9	Closed	S

Table 11: Field data of population L2 fractures at central Fuensalada

Distance (cm)	Strike	Dip	cc/-cc	Mode	MW (mm)	Open/closed	Clay-filled	Form
33	290	64	−cc	M1	4	+	+	W
193	284		−cc	M1	1	-	+	S
64	280	65	−cc	M1	22	+	+	S
57	288	66	−cc	M1	5	+	+	W
61	284	67	−cc	M1	2	+	+	W
62	280	76	−cc	M1	2	-	+	Curved

55	289	61	−cc	M1	22	+	+	W
59	277	72	−cc	M1	3	-	+	Curved
12	276	81	−cc	M1	3	+	+	W
35	273	74	−cc	M1	10	+	+	W
26	273	63	−cc	M1	4	+	+	W
45	280		−cc	M1	3	+	+	W
27	283	67	−cc	M1	31	+	+	S
25	111	79	−cc	M1	7	+	+	W
12	290	86	−cc	M1	3	+	+	S
21	290	67	−cc	M1	4	+	+	W
16	100	86	−cc	M1	3	+	+	S
33	108	70	−cc	M1	23	+	+	W
21	292	70	−cc	M1	12	+	+	S
8	286	84	−cc	M1	1	-	+	S
18	299		−cc	M1	1	-	+	Curved
31	296	85	−cc	M1	7	+	+	S
36	104	87	−cc	M1	3	+	+	S
9	295	87	−cc	M1	8	+	+	W
25	105	85	−cc	M1	6	+	+	S
40	116	81	−cc	M1	14	+	+	Curved
66	114	77	−cc	M1	4	-	+	W
10	111	80	−cc	M1	7	+	+	W

11	300	70	−cc	M1	6	+	+	S
15	293	68	−cc	M1	3	+	+	S
23	294	67	−cc	M1	3	+	+	S
35	108	87	−cc	M1	2	+	+	W
16	289	60	−cc	M1	1	+	+	S

Table 12: Field data of population L3 at northern Fuensalada.

Distance (cm)	**Strike**	**Dip**	**cc/-cc**	**Mode**	**MW (mm)**	**Open/closed**	**Clay-filled**	**Form**
33	290	64	−cc	M1	4	+	+	W
193	284		−cc	M1	1	-	+	S
64	280	65	−cc	M1	22	+	+	S
57	288	66	−cc	M1	5	+	+	W
61	284	67	−cc	M1	2	+	+	W
62	280	76	−cc	M1	2	-	+	Curved
55	289	61	−cc	M1	22	+	+	W
59	277	72	−cc	M1	3	-	+	Curved
12	276	81	−cc	M1	3	+	+	W
35	273	74	−cc	M1	10	+	+	W
26	273	63	−cc	M1	4	+	+	W
45	280		−cc	M1	3	+	+	W
27	283	67	−cc	M1	31	+	+	S

25	111	79	−cc	M1	7	+	+	W
12	290	86	−cc	M1	3	+	+	S
21	290	67	−cc	M1	4	+	+	W
16	100	86	−cc	M1	3	+	+	S
33	108	70	−cc	M1	23	+	+	W
21	292	70	−cc	M1	12	+	+	S
8	286	84	−cc	M1	1	-	+	S
18	299		−cc	M1	1	-	+	Curved
31	296	85	−cc	M1	7	+	+	S
36	104	87	−cc	M1	3	+	+	S
9	295	87	−cc	M1	8	+	+	W
25	105	85	−cc	M1	6	+	+	S
40	116	81	−cc	M1	14	+	+	Curved
66	114	77	−cc	M1	4	-	+	W
10	111	80	−cc	M1	7	+	+	W
11	300	70	−cc	M1	6	+	+	S
15	293	68	−cc	M1	3	+	+	S
23	294	67	−cc	M1	3	+	+	S
35	108	87	−cc	M1	2	+	+	W
16	289	60	−cc	M1	1	+	+	S
	286,708333	**74,4**						

Table 13: Field data of population L4 at Northern Fuensalada.

Appendix II

Distance (cm)	Strike	Dip	cc/-cc	Mode	MW (mm)	Open/closed	T.W (mm)	Form
35	96	76	cc	M1	28	Closed		S
107	279	79	cc	M1		Open	15	S
78	280	67	cc	M1		Open	17	S
33	280	74	cc	M1	9	Closed		S
71	280	80	cc	M1		Open	26	S
89	271	70	cc	M1	6	Closed		S
31	281	69	cc	M1		Open	18	S
118	281	74	cc	M1	27	Closed		S
91	279	73	cc	M1		Open	25	S
112	279	69	cc	M1		Open	24	S
82	281	70	cc	M1		Open	16	S
47	284	69	cc	M1		Open	10	S
83	280	69	cc	M1	6	Closed		S
66	272	78	cc	M1	25	Closed		S
77	283	65	cc	M1	29	Closed		S
56	275	69	cc	M1	22	Closed		S
92	286	69	cc	M1		Open	10	S
57	280	70	cc	M1		Open	14	S
68	277	67	cc	M1		Open	18	S

86	279	67	cc	M1		Open	18	S
93	284	72	cc	M1	4	Closed		S
36	279	78	cc	M1	2	Closed		S
113	280	70	cc	M1	3	Closed		S
11	280	80	cc	M1		Open	17	S
95	277	69	cc	M1	7	Closed		S
46	278	69	cc	M1		Open	18	S
70	286	64	cc	M1	5	Closed		Curved

Table 14: Field data of population L5 in bed one at central Fuensalada.

Distance (cm)	**Strike**	**Dip**	**cc/-cc**	**Mode**	**MW (mm)**	**Open/closed**	**T.W (mm)**	**Form**
0	283	67	cc	M1	3	Open		W
33	270	73	cc	M1		Open	2	W
34	278	75	cc	M1	1	Open		S
177	279	71	cc	M1		Open	11	S
168	286	70	cc	M1		Open	19	S
133	286	65	cc	M1		Open	18	S
100	284	64	cc	M1	5	Closed		S
155	280	61	cc	M1	3	Closed		S
77	285	69	cc	M1	4	Closed		W
155	290	73	cc	M1	2	Closed		S

13	280	64	cc	M1	7	Closed		S
99	283	64	cc	M1		Open	12	S

Table 15: Field data of population L5 in bed two at central Fuensalada.

Distance (cm)	**Strike**	**Dip**	**cc/-cc**	**Mode**	**MW (mm)**	**Open/closed**	**Form**
0	273	70	cc	M1	4	Closed	S
62	271	72	cc	M1	5	Closed	S
40	270	74	cc	M1	18	Closed	S
112	270	68	cc	M1	9	Closed	S
50	270	64	cc	M1	2	Closed	W
13,8	278	68	cc	M1	1	Closed	W
56	277	69	cc	M1	1	Closed	W
75	273	68		M1	1	Closed	S
15	276	68	cc	M1	3	Closed	W
212	269	66	cc	M1	7	Closed	W

Table 16: Field data of population L5 in bed three at central Fuensalada.

Distance (cm)	**Strike**	**Dip**	**cc/-cc**	**Mode**	**MW (mm)**	**Open/closed**	**Form**
0	272	78	cc	M1	11	Closed	S
118	275	65	cc	M1	7	Closed	W
66	272	71	cc	M1	2	Closed	W

Table 18: Field data of population L5 in bed four at central Fuensalada.

Appendix II

Distance (cm)	**Strike**	**Dip**	**cc/-cc**	**Mode**	**MW (mm)**	**Open/closed**	**T.W (mm)**	**CPO (mm)**	**Form**
0	283	73	cc	M1		Open	15	4	W
55	290	64	cc	M1	2	Closed			W
148	284	65	cc	M1	4	Closed			W
124	278	72	cc	M1	9	Closed			W
100	276	67	cc	M1	19	Closed			S
78	280		cc	M1	13	Closed			S
25	279	77	cc	M1	2	Closed			S
35	273	67	cc	M1		Open	10	1	S
81	276	77	cc	M1		Open	6	1	S
60	273	64	cc	M1	5	Closed			S
44	280		cc	M1	6	Closed			W
117	286	65	cc	M1	7	Closed			S
122	270	72	cc	M1	1	Closed			S
7	281	63	cc	M2	8	Closed			W
89	285	65	cc	M1	8	Closed			S
36	294	64	cc	M1	4	Closed			W
82	286	69	cc	M1	3	Closed			S
81	281	70	cc	M1	10	Closed			W
117	278	69	cc	M1		Open	6	1	S
99	281	73	cc	M1		Open	4	1	S

96	286	66	cc	M1		Open	19	2	W
160	277	70	cc	M1	4	Closed			W

Table 19: Field data of population L5 in bed five at central Fuensalada.

Distance (cm)	**Strike**	**Dip**	**cc/-cc**	**Mode**	**MW (mm)**	**Open/closed**	**Clay-filled**	**Form**
0	296	88	−cc	M1	1	Open	-	S
168	295	82	−cc	M1	2	Open	-	S
82	286	84	−cc	M1	1	Open	-	S
160	119	84	−cc	M1	1	Open	-	Curved
292	299	72	−cc	M1	1	Open	-	S
77	293	85	−cc	M1	2	Open	-	S
380	291	86	−cc	M1	1	Open	-	S
39	290	82	−cc	M1	2	Open	-	S

Table 20: Field data of population L6 in bed three at central Fuensalada.

Distance (cm)	**Strike**	**Dip**	**cc/-cc**	**Mode**	**MW (mm)**	**Open/closed**	**Clay-filled**	**Form**
10	299	81	−cc	M1	0.5	Open	-	W
260	290	89	−cc	M1	1	Open	-	W
36	290	90	−cc	M1	1	Open	-	S
103	294	86	−cc	M1	1	Open	-	S
107	290	84	−cc	M1	1	Open	-	W
212	283	81	−cc	M1	2	Open	-	W
214	292	88	−cc	M1	1	Open	-	S

Table 21: Field data of population L6 in bed four at central Fuensalada.

Distance (cm)	Strike	Dip	cc/-cc	Mode	MW (mm)	Open/closed	Clay-filled	Form
0	165	76	−cc	M1	11	Closed	-	W
100	190	74	−cc	M1	10	Closed	-	W
10	360	66	−cc	M1	7	Closed	-	W
115	347	68	−cc	M1	10	Closed	-	W
144	193	81	−cc	M1	6	Closed	-	W
186	189	79	−cc	M1	3	Closed	-	W

Table 22: Field data of population L7 in bed two at central Fuensalada.

Distance (cm)	Strike	Dip	cc/-cc	Mode	MW (mm)	Open/closed	Clay-filled	Form
0	202	77	−cc	M1	2	Closed	-	S
140	202	71	−cc	M1	1	Closed	-	W
300	22	74	−cc	M1	1	Closed	-	Curved
190	212	76	−cc	M1	2	Closed	-	Curved

Table 23: Field data of population L7 in bed three at central Fuensalada.

Distance (cm)	Strike	Dip	cc/-cc	Mode	MW (mm)	Open/closed	Clay-filled	Form
0	180	63	−cc	M1	1	Closed	-	S
36	13	78	−cc	M1	1	Closed	-	W
129	184	78	−cc	M1	2	Closed	-	W
112	188	83	−cc	M1	1	Closed	-	S

11	196	79	−cc	M1	0,5	Closed	-	Curved
117	197	70	−cc	M1	3	Closed	-	S
370	199	67	−cc	M1	2	Closed	-	S
144	196	72	−cc	M1	2	Closed	-	W
101	10	89	−cc	M1	1	Closed	-	S
84	197	81	−cc	M1	1	Closed	-	S
32	192	78	−cc	M1	1	Closed	-	S

Table 24: Field data of population L7 in bed five at central Fuensalada.

Strike	Dip	cc/-cc	Mode	MW (mm)	Open/closed	Form
92	32	cc	M2	34	closed	S
97	33	cc	M2	54	closed	S
104	27	cc	M2	23	closed	S
105	28	cc	M2	56	closed	S
95	29	cc	M2	44	closed	S
96	31	cc	M2	34	closed	S
105	30	cc	M2	3	closed	S
103	57	cc	M2	1	closed	S
102	30	cc	M2	67	closed	S
98	55	cc	M2	24	closed	S

Table 25: Field data of population L8 at southern Fuensalada.

Strike	Dip	cc/-cc	Mode	MW (mm)	Open/closed	Form
297	33	cc	M2	42	Closed	S
297	35	cc	M2	16	Closed	S
301	32	cc	M2	7	Closed	S
298	38	cc	M2	8	Closed	S
289	35	cc	M2	2	Closed	S
292	41	cc	M2	8	Closed	S
304	45	cc	M2	65	Closed	S
299	51	cc	M2	9	Closed	S
289	35	cc	M2	13	Closed	S

Table 26: Field data of population L9 at southern Fuensalada.